A Computational Based Approach for Non-invasive Localization of Atrial ectopic foci

Eduardo J. Godoy

Directors of the thesis

Dr. Miguel Lozano and Dr. Rafael Sebastian
Department of Computer Sciences

VNIVERSITAT ID VALÈNCIA

Directors

Dr. Rafael Sebastian   Associate Professor
                  Universitat de Valencia
                  Valencia, Spain

Dr. Miguel Lozano   Associate Professor
                  Universitat de Valencia
                  Valencia, Spain

Review Committee (Main):

Prof. Pablo Laguna Lasaosa   Universidad de Zaragoza
Dr. Francisco Martínez Gil   Universidad de Valencia
Dra. Beatriz Ana Trenor Gomis   Universidad Politécnica de Valencia

Review Committee (Reserve):

Prof. Oscar Camara Rey   Universitat Pompeu Fabra
Prof. Francisco Ferri Rabasa   Universidad de Valencia
Dra. Maria de la Salud Guillem Sánchez Universidad Politécnica de Valencia

A mis hijos y a Lourdes

Abstract / Resumen

Abstract   Atrial arrhythmias are the most common cardiac arrhythmia, affecting six million people in Europe and imposing a huge healthcare burden on society. New technologies are helping electrophysiologists to tailor the treatment to each patient in different ways. For instance, magnetic resonance imaging (MRI) allows to assess the spatial distribution of atrial fibrosis; electro-anatomical maps (EAM) permit to obtain an electrical characterization of tissue in real-time; electrocardiographic imaging (ECGI) allows to study cardiac electrical activity non-invasively; and radiofrequency ablation (RFA), allows to eliminate pathological tissue in the heart that is triggering or sustaining an arrhythmia. Despite the access to advanced technologies and well-developed clinical guidelines for the management of atrial arrhythmia, long-term treatment success rates remain low, due to the complexity of the disease. Therefore, there is a compelling need to improve clinical outcomes for the benefit of patients and the healthcare system.

Detailed biophysical models of the atria and torso could be employed to integrate all the patient data into a single reference 3D model able to reproduce the complex electrical activation patterns observed in experiments and clinics. However, there are some limitations related to the difficulty of building such models for each patient, or performing a substantial number of simulations to plan the optimal RFA therapy. Considering all those limitations, we propose to use detailed biophysical models and simulations as a tool to train machine learning systems, for which we have all the ground-truth data which would be impossible to obtain in a real clinical setting. Therefore, we can perform hundreds of electrophysiology simulations, considering a variety of common scenarios and pathologies, and train a system that should be able to recognize them from a limited set of non-invasive patient data, such as an electrocardiogram (ECG), or a body surface potential map (BSPM).

The main aim of this thesis is to develop a computational pipeline combining biophysical simulations and machine learning that allows to guide electrophysiologists during RFA procedures on patients with atrial tachycardia, using only non-invasive BSPM data. In summary, the main contributions of this thesis are:

- Multi-scale modeling pipeline for the simulation of focal atrial tachycardia (FAT): we propose an atrial modeling pipeline that allows to simulate FAT electrical activation sequences, including pathological tissue such as fibrosis. The modeling pipeline has the potential to generate hundreds of simulations, including scenarios that combine fibrosis in different locations and densities, with FAT triggered from any origin at the atria. As a result we obtain, the virtual EAM for each scenario and its corresponding BSPM on the torso model coupled to the atria. We also analyze the main effects of the fibrosis on the BSPM for a given site of origin of the FAT.

- System for predicting the site of origin of atrial tachycardia: we have developed a machine learning system to exploit the results from in-silico simulations. The system learns how to relate a reduced BSPM to the site of origin of a FAT, considering specifically the potential presence of fibrosis in the models. Following, given a clinical BSPM, the system is able to predict the origin of the FAT preoperatively, and guide the electrophysiologist to achieve the location where RFA has to be delivered. We assess the accuracy of the system for the different scenarios, and the effects of fibrosis density on the predictions.

- Validation of the full pipeline on an exemplary clinical case: we have designed a clinical protocol based on pace-mapping to acquire a collection of BSPMs from a patient together with the pacing locations. We locate the position of the BSPM electrodes using a 3D camera installed in the EP-lab at the hospital, and assess the accuracy of the system in predicting several sites of origin for the FAT.

Resumen Las arritmias auriculares son las arritmias cardíacas más comunes, afectan a seis millones de personas en Europa e imponen una enorme carga sanitaria en la sociedad. Las nuevas tecnologías médicas están ayudando a los electrofisiólogos a adaptar el tratamiento a cada paciente de diferentes maneras. Por ejemplo, la resonancia magnética (MRI) permite evaluar la distribución espacial de la fibrosis auricular; los mapas electroanatómicos (EAM) permiten obtener una caracterización eléctrica de los tejidos en tiempo real; Las imágenes electrocardiográficas (ECGI) permiten estudiar la actividad eléctrica cardíaca de forma no invasiva; y la ablación por radiofrecuencia (RFA), permite eliminar el tejido patológico en el corazón que desencadena o mantiene una arritmia. A pesar del acceso a tecnologías avanzadas y de la existencia de guías clínicas bien desarrolladas para el tratamiento de las arritmias auriculares, las tasas de éxito del tratamiento a largo plazo siguen siendo bajas, debido a la complejidad de la enfermedad. Por lo tanto, existe una necesidad imperiosa de mejorar los resultados clínicos en beneficio de los pacientes y el sistema de salud.

Se podrían emplear modelos biofísicos detallados de las aurículas y el torso para integrar todos los datos del paciente en un solo modelo 3D de referencia capaz de reproducir los complejos patrones de activación eléctrica observados en experimentos y la clínica. Sin embargo, existen algunas limitaciones relacionadas con la dificultad de construir tales modelos para cada paciente o realizar un número considerable de simulaciones para planificar la terapia óptima de RFA. Teniendo en cuenta todas esas limitaciones, proponemos utilizar modelos biofísicos detallados y simulaciones como una herramienta para entrenar sistemas de aprendizaje automático, para lo cual dispondríamos de todos los datos y variables del problema, que serían imposibles de obtener en un entorno clínico real. Por lo tanto, podemos realizar cientos de simulaciones electrofisiológicas, considerando una variedad de escenarios y patologías comunes, y entrenar un sistema que debería ser capaz de reconocerlos a partir de un conjunto limitado de datos no invasivos del paciente, como un electrocardiograma (ECG), o mapa de potencial de superficie corporal (BSPM).

El objetivo principal de esta tesis es desarrollar un flujo de datos computacional que combine simulaciones biofísicas y aprendizaje automático que permita guiar a los electrofisiólogos durante los procedimientos de RFA en pacientes con taquicardia auricular, utilizando solo datos BSPM no invasivos. En resumen, las principales contribuciones de esta tesis son:

- Secuencia de procesos de modelado multiescala para la simulación

de taquicardia auricular focal (FAT): proponemos un flujo de datos de modelado auricular que permita simular secuencias de activación eléctrica de FAT, incluyendo tejido patológico, como la fibrosis. Este flujo de datos de modelado tiene el potencial de generar cientos de simulaciones, incluidos escenarios que combinen fibrosis en diferentes localizaciones y densidades, con FAT desencadenado desde cualquier origen en las aurículas. Como resultado, obtenemos el EAM virtual para cada escenario y su BSPM correspondiente en el modelo de torso acoplado a las aurículas. También analizamos los principales efectos de la fibrosis en el BSPM para un conjunto determinado sitios de origen de la FAT.

- Sistema para predecir el lugar de origen de la taquicardia auricular: hemos desarrollado un sistema de aprendizaje automático para explotar los resultados de las simulaciones in-silico. El sistema aprende cómo relacionar un BSPM reducido con el sitio de origen de un FAT, considerando específicamente la posible presencia de fibrosis en los modelos. Luego, dado un BSPM clínico, el sistema puede predecir el origen de la FAT preoperatoriamente y guiar al electrofisiólogo mostrándole la región donde se debe administrar la RFA. Evaluamos la precisión del sistema para los diferentes escenarios y los efectos en las predicciones.

- Validación completa del sistema en un caso clínico: hemos diseñado un protocolo clínico basado en pace-mapping para adquirir una colección de BSPM de un paciente junto con las ubicaciones de estimulación (EAM). Localizamos la posición de los electrodos BSPM utilizando una cámara 3D instalada en el laboratorio EP del hospital, y evaluamos la precisión del sistema para predecir varios sitios de origen para el FAT.

Preface

I would like to express my sincere gratitude to my thesis directors Dr. Rafael Sebastian and Dr. Miguel Lozano for their continuous support of my studies and research, for his patience, motivation, enthusiasm, and their knowledge. Their guidance helped me in all the time of my research and the writing of this thesis. I could not have had better advisors and mentors for my work.

I thank my fellow lab mates in the Ci2B group at the Universidad Politécnica de Valencia, were I started my PhD studies, and the lab mates and professors in CoMMLab group here in the Universidad de Valencia. In particular, I am grateful to Dr. Ignacio García for his advise in the first stages of my research.

Last but not the least, I dedicate this thesis to my children Natalia, Pablo, Herman, and Lucia who have always been a great emotional support and to those I love. Also my partner Lourdes for his support and care, and I love so much. And to all the people who made a long trip with me not limited to this work.

Contents

List of Figures

List of Tables

Acronyms

AF	Atrial fibrilation
AT	Atrial tachycardia
AP	Action potential
APD	Action potential duration
BB	Bachmann's bundle
BSPM	Body surface potential map
BSPiM	Body surface potential integral map
BCL	Basic cycle length
CV	Conduction velocity
CRN	Courtemanche-Ramirez-Nattel ionic model
CS	Coronary sinus
CT	Crista Terminalis
EAM	Electro-anatomical map
ECG	Electrocardiogram
ECGI	Electrocardiographic imaging
FAT	Focal atrial tachycardia
FO	Fossa ovalis
HR	High-Resolution BSPiM
IAS	Interatrial Septum
IVC	Inferior vena cava
LA	Left atrium
LAA	Left atrial appendage
LAT	Local activation time
LGE MRI	Late Gadolinium Enhanced MRI
LV	Left ventricle
LR-BSPiM	Low-resolution BSPiM
LSPV	Left superior pulmonary vein
ML	Machine learning
MRI	Magnetic Resonance Imaging
PM	Pectinate muscles
PVI	Pulmonary vein isolation
RA	Right atrium
RAA	Right atrial appendage
RFA	Radiofrequency ablation
RIPV	Right inferior pulmonary veins

RMP	Resting membrane potential
RSPV	Right superior pulmonary veins
SAN	Sinoatrial node
SVC	Superior vena cava
SVM	Support vector machine
TVR	Tricuspid valve ring
VF	Ventricular fibrilation
VT	Ventricular Tachycardia

1

Introduction

1.1   Motivation

Cardiac arrhythmias are one of the main causes of morbidity and mortality in developing countries. There is a rapidly growing prevalence due to aging of the population, where comorbidities like obesity, hypertension and diabetes are major risk factors. Currently, there are approximately 6 million adults in Europe with atrial fibrillation (AF) with the number expected to increase by a factor of 2.5 by 2050 [1]. Atrial tachycardias (AT), excluding atrial flutter, are thought to represent about 5% to 15% of sustained supraventricular tachycardias in the adult, and are more frequent in the pediatric population.

Pharmacological, electrical therapies and surgical/electrophysiological procedures are widely used to treat cardiac arrhythmias. However, currently the use of anti-arrhythmic drugs has main limitations, whether applied to atrial or ventricular arrhythmias. They have shown a reduced efficacy in many cases and can even result in development of new or worse ventricular arrhythmias, particularly in patients with a pro-arrhythmic substrate such as electrical and structural heart remodeling associated with chronic disease.

The treatment of atrial tachycardias by electrical therapies is focused on rhythm control and prevention of arrhythmia recurrence. Regarding these therapies, catheter ablation of complex arrhythmias was introduced 15 years ago, combined with 2D fluoroscopic navigation systems. Only five years after, 3D catheter localization technology was developed to enable color-coded mapping of cardiac electrical data on cardiac surfaces. Different generations of mapping and ablation catheters or signal processing tools were also iteratively integrated into clinical practice. During these successive waves of development, the clinical community has demonstrated its ability to change its practice and rapidly adapt to the most recent technology.

In parallel, other technologies such as non-invasive imaging techniques also progressed to enable precise characterization of cardiac diseases. For instance, delay enhancement MRI is used to identify infarcted areas or fibrotic tissue in ventricles and atria. More recently, body surface ECG imaging (ECGI), i.e. a system that uses a 250-electrode vest to reconstruct cardiac electrical activity from body surface potentials, has given access to real-time and panoramic mapping of cardiac electrical activity [2]. Preliminary results show that such techniques could be used to improve patient selection for pacing and ablation procedures, and to personalize these therapies through

real-time intra-procedural image integration. However, ECGI involves the solution of the inverse problem in electrocardiography from the set of body surface electrodes. This problem presents an important mathematical challenge since it is an ill-conditioned, non-linear problem that requires a strong mathematical basis coupled with a deep understanding of the propagation of electrical signals in tissues. After the problem is solved, signal processing has to be performed to identify the mechanisms likely to maintain the arrhythmia, i.e. focal discharges or re-entry patterns (rotors).

To date, the afore-mentioned personalized approaches have not penetrated into clinical practice, which can be attributed to a number of reasons:

- Lack of required equipment: in most cases state-of-the-art MRI systems equipped with full commercial software licenses are required to acquire and process non-standard image sequences such as those to detect fibrosis with enough level of detail. In other cases, special devices such as ECGI electrode vests are not available due to their high cost, or the lack of clear evidence of their advantages.

- Absence of integration among diverse imaging technologies, such as MRI, EAMs and ECGI systems, which provide data in their own reference systems but do not offer electrophysiologists an integrated view of all data. That leaves the integration effort to teams of engineers that in some cases collaborate with clinical centers, and have to develop customized software tools compatible with current commercial systems.

- Lack of reference data: when advanced technologies are used (accessible only to a small amount of the population or medical centers), it might be difficult to interpret the results due to the scarce reference data available to characterize each pathology. Systems such as those based on ECGI are tested on small clinical trials, and its benefit and accuracy for the overall population is still not clear.

- Weak cooperation between scientific disciplines (cardiology and radiology) and industries (cardiac rhythm management and medical imaging).

- Lack of clinical validation. This is probably the most challenging point, since new technologies are usually tested in small population cohorts or specific diseases, which makes it difficult to assess their accuracy, or consider them into Clinical Guidelines.

All these facts lead to an overall clinical outcome that is still perceived as suboptimal, with success rates in the range of 60 to 65%. On the other hand, the area of computational physiology has shown the potential to provide aid in clinical decision making in a few technologically advanced hospitals in the world [3]. The main objective of these techniques is the development of realistic 3D biophysical models of different organs, such as the heart, that include, with a high degree of detail, genetic characteristics of the ionic currents, their mutations, the electrophysiological characteristics of the different cardiac cell types, the anatomical structure of cardiac tissues, and in general of the human body. Following, the models are used to simulate the heart function, e.g., electrophysiology, to try to predict the outcome of an intervention [4]. However, the construction and simulation of such models is very time consuming (in the order of days per case), even if high performance computing is used, which renders the approach as impractical from the clinical perspective.

An alternative use of those biophysically detailed models, that could help to overcome the limitations described, is to exploit them to generate large amounts of simulated datasets. The goal is to produce data, where all scenarios and variables are tightly controlled, that can be used to train artificial intelligent systems aimed to aid electrophysiologist in clinical decision making, and therapy planning. Among the advantages of this new approach, there are: i) the construction of detailed models is performed by engineers from retrospective clinical datasets that can represent a target population; ii) all the simulations can be carried out in high performance computers and ran off-line without clinical time constraints; iii) trained machine learning models are easy to use and do not require intervention of engineers, or long computation times to provide a recommendation.

1.2 Objectives

Currently, physician decisions in the management of cardiac arrhythmias are based on the patient situation, the diseases characteristics and the clinical Guidelines. Following the Guidelines, clinicians evaluate all the existing evidences of a particular arrhythmia with the aim of selecting the best treatment. Note that current Guidelines and recommendations assist the physicians to stratify patients and decide if they are candidate to a given therapy, although the final decision belongs to the physician in charge of the patient care.

Once the patient is classified as candidate to an electrical therapy, such as RFA, the measures adopted for his treatment are decided mainly during the surgery, which prevents carrying out a detailed and personalized planning tailored to the patient. Depending on cases, a pre-operative plan can be performed based on the data available from the patient, which is usually the ECG, and in some advanced clinical centers ECGI. The electrophysiologist, based on his experience and the reference values of the literature can try to stratify the patient into a group that help him to personalize the RFA.

A more robust pre-interventional evaluation of the patient would be of great benefit to the outcome of the procedure. The improvement could be achieved by incorporating new technologies from the area of computational physiology, combined with machine learning techniques to help infer the location of pro-arrhythmic electrical substrates and rotors. Having such information pre-operatively can have an impact in the RFA outcome, improving its chances of success and reducing the total time. Nowadays, simulations are much faster, more cost-effective and less invasive than building and testing physical prototypes, or carrying large clinical trials, which makes this technology an interesting alternative.

Therefore, in order to improve the therapy planning and follow-up of RFA interventions, and increase our knowledge about complex cardiac arrhythmias, I propose to develop a set of advanced computational modeling tools and machine learning pipelines aiming at better characterizing the 3D dynamics of cardiac activation during FAT episodes, and predict its origin to better plan RFA pre-operatively. Such a model should be able to consider comorbidities such as the existence of fibrotic tissue in the atria that can be distributed randomly in different densities.

This overall objective can be divided in the following steps:

1. To study the effect of coupling fibroblast and healthy atrial tissue on the electrical wave propagation.

2. To build a set of 3D atrial models with varying fibrosis distribution and perform FAT multi-scale electrophysiology simulations for each scenario.

3. To develop a machine learning system trained with electrophysiology FAT simulations to support clinicians to predict the location of ectopic foci prior to the RFA intervention.

4. To validate the proposed methodology on an exemplary clinical case.

To achieve the first goal, I constructed a simplified geometry consisting in a 3D slab of tissue, that will simplify the interpretation of results. On the slab, I analyzed two conditions: the amount of fibrosis required to generate a conduction block, and the minimum thickness of a conduction channel required to permit the propagation of the depolarization wavefront to cross it. The goal of these simulations is to understand how the propagation of an electrical wavefront can be altered by the fibrosis depending on its density. Finally, I also analyzed changes in the action potential (AP) in the atrial tissue in the surroundings of the fibrosis and inside the fibrotic tissue. All those changes in the atria activation will have an impact on the ECG and BSPM.

For the second goal, I started from a reference atrial anatomical model that included a detailed definition of fiber orientation and consider cell and tissue heterogeneity for different regions. On that model I included fibrotic tissue in different regions and densities. As a result, I created five different distributions of fibrosis with five different increasing densities, giving rise to 25 atrial fibrotic models. All the models were electrically stabilized, and used to simulate FAT. Following, I selected 20 different locations distributed between both atria that will be the origins of the FAT, and I performed simulations to obtain the electrical activation map. Next, the extracellular potential from the atria activation was propagated to the torso surface to obtain the BSPM. Finally, all the BSPM were processed to extract the body surface potential integral maps (BSPiM) for each of the 500 three-dimensional atria-torso simulations.

For the third goal, I developed a machine learning pipeline to learn the relationship between the location of the ectopic focus and the BSPiM that it generates. In healthy conditions (without fibrosis), I first study the minimum number of electrodes in the BSPM required to related BSPiM and ectopic focus locations, as well as I determined the optimal electrode locations. In disease, I studied how the increment of fibrosis over the left atrium affects the BSPiM, and how the machine learning systems gets its accuracy affected. I also provide the limitations of the system for the different scenarios studied.

For the last goal, I defined a clinical protocol based on pace-mapping to record BSPMs from a patient that was going to undergo pulmonary vein isolation (PVI). I constructed our own BSPM system taking advantage of the CARTO3 system polygraph and 64 custom made chest electrodes. The signals corresponding to all the pacing sites were processed at the electrodes,

de-noised, and the BSPiM calculated. It is noteworthy that to achieve this goal, a novel 3D camera setup was incorporated to determine the location of the electrodes on the torso surface of the patient, which signals have to be subsequently classified using the machine learning pipeline developed. Having such information it is crucial since the surface ECG changes depending on the position of the electrodes.

1.3   Thesis Outline

After this chapter, the rest of the thesis is organized as follows.

Chapter 2. It introduces the clinical and technical background required to lay down the basis of the work carried out in this thesis. I briefly introduce the heart function, including cardiac electrophysiology at cellular and tissue level in health and disease. I describe the current clinical technologies used for diagnostic and treatment of atrial arrhythmia, including imaging and electroanatomical navigation systems. Following, I review the state-of-the-art on biophysical electrophysiology modeling of the atria, paying special attention to anatomical and functional models that include fibrosis. Finally, I review current machine learning tools, and their application to diagnosis of cardiac arrhythmias.

Chapter 3. In this chapter, I first describe the properties of a simplified model constructed to study the effects of fibrosis in tissue. Following several scenarios are presented, and the electrical simulations carried out detailed together with the ionic models chosen. Finally, the results from the electrophysiology simulations are obtained for the particular configurations selected in the thesis.

Chapter 4. This chapter describes the anatomical model of the atria used for the electrical simulations. In short, the geometry, fiber orientation, cellular and tissue heterogeneities, are described. Next, the inclusion of fibrosis and the 25 resulting fibrotic models are summarized. I also describe the stimulation protocol defined for the simulation of FAT with different origins. Finally, the 500 atria-torso simulations resulted are analyzed, from which a subset is selected for training of the ML algorithms. Patterns for the BSPiM are analyzed, paying attention to the effects of the fibrosis density for a given ectopic focus location.

Chapter 5. In this chapter, I present the ML pipeline designed to classify
ectopic focus and associate them to specific regions of the atria. We
first analyze BSPiM from healthy atria, and perform a dimensionality
reduction to obtain the critical electrodes required to properly clas-
sify the ectopic foci. Following, we consider all the simulations with
fibrosis, introducing incrementally the most dense fibrotic cases. We
summarize the results including the classification accuracy, and the
effect of fibrosis in the classifier.

Chapter 6. In this chapter, I discuss the steps carried out to acquire and
process the BSPiM of a patient that underwent PVI by RFA. The
procedure included a pace-mapping protocol before the RFA which
permitted to acquire BSPiM from focus triggered from different lo-
cations. The data is used to validate the ML pipeline built with the
electrophysiological simulations.

Chapter 7. This chapter summarizes the most important ideas and con-
tributions of this thesis. I highlight the strengths and limitations, and
propose future research directions.

State of the Art: Clinical and Computational Atrial Arrhythmias

2.1   The Heart

The heart is a complex organ responsible for pumping oxygenated blood into the vessels of the circulatory system. It is located posterior to the sternum between the left and right lung lobes, and has a size comparable to a closed human fist. The heart is made up of four chambers (see Figure 2.1), two atria and two ventricles with differentiated functions. In fact, it functions as a double pump sometimes referred as right heart and left heart, that are subdivided in two chambers, the atria (upper chambers) and the ventricles (lower chambers), giving rise to the four heart chambers [5].

The right atrium (RA) collects venous blood (oxygen-depleted) from the systemic circulation via the inferior and superior vena cava (IVC/SVC) and also from the coronary sinus (CS). It transfers the blood to the right ventricle (RV) through the tricuspid valve (TV). From there, the blood is subsequently pumped to the lungs. The left atrium (LA) collects oxygenated blood from the lung circulatory system, usually through four pulmonary veins. The LA passes the blood through the mitral valve into the left ventricle (LV), which then pumps it into the body circulatory system. The myocardium receives the oxygen from the coronary circulation, and in particular the coronary arteries, which originate from the ascending part of the aortic arch, and are critical for the proper function of the heart. Blood from the coronary veins is collected in the CS, which runs posterior between the LV and LA into the RA.

Note that there is a one-way blood flow in the heart thanks to the four heart valves. To prevent that blood flows back from the ventricles into the atria, the tricuspid and mitral valves, also known as atrioventricular valves, close during ventricular systole, and open again during ventricular diastole. The opening and closing of the valves is due to differential blood pressure between chambers.

The effective pumping action of the heart requires a precise coordination of the myocardial contractions (millions of cells), that is initiated by electrical excitatory impulses (APs) which propagate along their surface membranes. The electrical currents generated in the heart also spread to other tissues in the body, and can be recorded on the torso surface, which provides the electrocardiogram (ECG). Alterations in the cardiac impulse can lead to cardiac arrhythmia, a condition in which the heart rhythm is irregular and beats systematically faster or slower than the normal range of 60-100 beats per minute at rest.
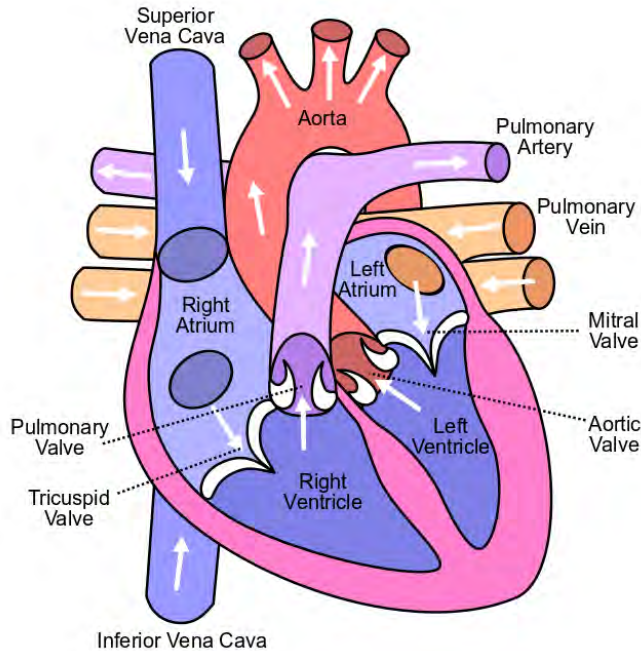
Figure 2.1: Schematic view of the heart showing the four chambers, main veins and arteries. The blood flow direction is shown by white arrows at the valves. Source: https://commons.wikimedia.org/

2.1.1 Atria Anatomy

The atrial chambers lie to the right of their respective ventricular chambers. The RA has an anterior position, that is closer to the chest, whereas the LA is posterior and superior, and therefore closer to the back. From a frontal view the wall that separates both atria, the interatrial septum, forms and angle of around 65 degrees to the vertical plane (known as sagittal plane). The tracheal bifurcation, and the esophagus, are immediately behind the pericardium, being directly related to the posterior wall of the LA. The anterior wall of the LA is located behind the ascending aorta. Although both atria differ markedly in their shape, they are basically made up of a venous component, an appendage, and a vestibule. The atria have relatively thin chambers compared to the ventricles, since ventricles have to generate greater pressure to propel blood into the pulmonary circulation in the case of the RV and to the rest of the body in the case of the LV.

We can divide the atria in 21 different anatomical regions, that in some
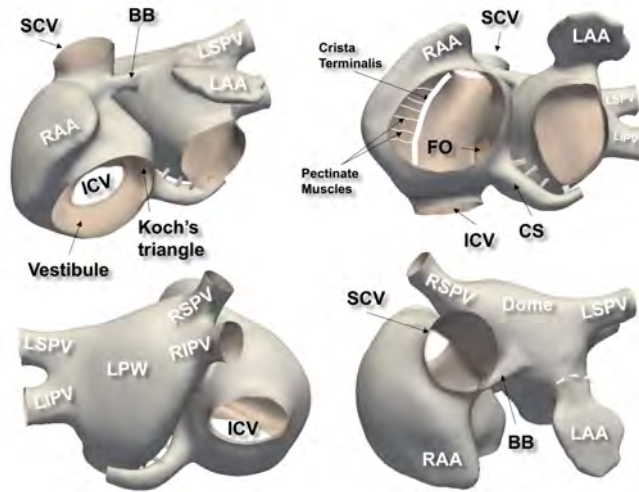
Figure 2.2: Three-dimensional model reconstructed from an MRI in which the different atria regions have been labeled. RA: Right atrium, PM: Pectinate muscles, CT: Crista Terminalis, ICV: Inferior vena cava, CSO: Coronary sinus orifice; LA: left atrium, RIPV/LIPV: Right/Left inferior pulmonary vein, LV: left ventricle. Courtesy of Damian Sanchez-Quintana

cases can be subdivided into specific substructures (see Figure 2.2). In the right atria (RA), we can differentiate 12 regions: sinoatrial node (SAN), Crista Terminalis (CT), Bachmann bundle (right part, BBR), intercaval bundle (IB), inter-atrial septum (IAS), lateral wall (RLW), right appendage (RAA), pectinate muscles (PM), isthmus (IST), superior (SCV) and inferior cava veins (ICV) and ring of the tricuspid valve (TV). In the left atria (LA) 8 regions can be identified besides the left section of the Bachmann bundle (BB): superior wall (LSW), septum (LAS), left appendage (LAA), posterior wall (LPW), ring of the mitral valve (MV), right inferior and superior (RIPV, RSPV) and left inferior and superior pulmonary veins (LIPV, LSPV) and the coronary sinus (CS). In addition, the fossa ovalis (FO) and its limb (LFO), which connects the RA and the LA, can be considered as one independent structure.

The Left Atrium

The LA has a smooth-walled body, with the pulmonary veins entering at the four corners of the venous regions, enclosing an atrial dome (see Figure 2.3 LA). The smooth LA endocardium does not show PMs with the excep-

tion of the appendage, which is a muscular ear-shaped pouch that extends prominently from the superolateral regions. The mean LA anteroposterior diameter is 38.4±4.9 mm in healthy subjects. The LA walls have an average thickness of 3.3±1.2 mm, which is larger than most of the RA, and presents a high variability between regions. For a comprehensive review of the thickness of the different atrial regions see [6, 7].

The four pulmonary veins (PVs) in the LA present a large anatomical variability compared to other heart structures. For instance, the number of venous orifices can vary between subjects, showing 5 openings in some cases, while in others two veins can be grouped in a common trunk. The reason is that in some cases the three lobar veins that emerge from the lungs in the right side remain separated, giving rise to three right openings. In addition, the two left or two right lobar veins can end up in a common orifice in the LA. The incidence of united veins is about 25% for the left pulmonary veins (LPVs) and about 3% in the right pulmonary veins (RPVs). It is important to remark that four fifth of the focal electrical triggers for atrial fibrillation are located in small muscular sleeves present in the PVs, that connect to the LA. These sleeves are more developed in upper than lower veins and their extent ranges from 13mm to 25mm. The only prominent endocardial structure in the otherwise smooth-walled LA body is a left lateral ridge, an infolding of atrial walls that extends between the LPV and the entrance of the left atrial appendage (LAA).

The LAA is a small finger-like or sac extension of the LA, that can present multiple lobules in some cases. The distal side of the LAA can lie in a number of anatomical locations such as the pulmonary trunk, or pointing posteriorly, or towards the back of the aorta, which makes the LAA a highly variable structure between subjects. Endocardially, there is a complex network of trabeculations or PMs. In a large study [8], the gross morphologies of the LAA were classified into four classes: cactus (30%), chicken wing (48%), windsock (19%), and cauliflower (3%). LAAs with a chicken wing morphology present mild trabeculations, cactus morphology moderate trabeculations and in cases with cauliflower morphology extensive trabeculations. The morphology of the LAA is of great importance, since due to its irregular lobulated shape it is prone to the development of thrombus during atrial fibrillation that can cause stroke, infarction and emboli. Patients with chicken wing LAA morphology have been reported to be less likely to have an embolic event, while cauliflower morphology is the most likely. In addition, the LAA appears to be responsible for triggering AF in 27% of patients presenting for repeat procedures of catheter ablation [9].
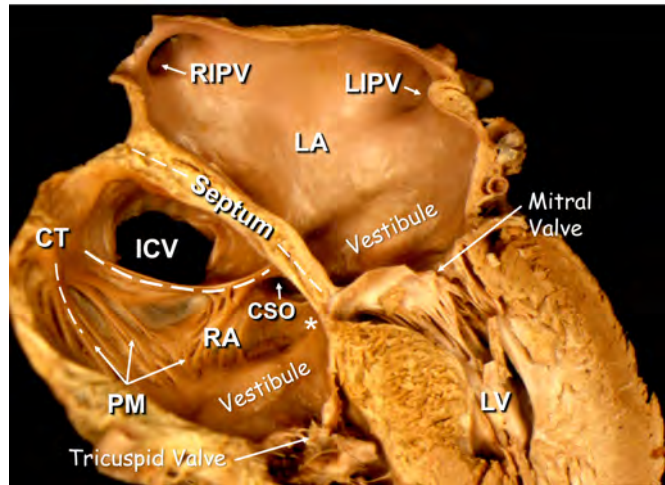
Figure 2.3: Anterior view of the atria, together with the main components. RA: Right atrium, PM: Pectinate muscles, CT: Crista Terminalis, ICV: Inferior vena cava, CSO: Coronary sinus orifice; LA: left atrium, RIPV/LIPV: Right/Left inferior pulmonary vein, LV: left ventricle. Courtesy of Damian Sanchez-Quintana

Under physiological conditions, the left atrium has a volume of 42 ml and a diameter of 3.7 cm [10], but structural remodeling caused by AF commonly increases left atrial volume [11].

The Right Atrium

As in the case of the LA, the RA presents an appendage (RAA) overlapping the aortic root which has a roughly triangular shape, and also contains multiple PMs (see Figure 2.3). The interatrial septum (IAS), the wall that separates LA and RA, presents a central region marked by a depression, that is observed in both atria and is known as the fossa ovalis (FO) or oval fossa. The FO is the remnant of a thin fibrous sheet that covered the foramen ovale during fetal development. During that period both atria are connected and the blood can flow directly between them. If one wants to be rigorous, the atrial septum should be limited to the region below the FO and its immediate muscular rim. Most of the rim around the FO is formed by infoldings of the atrial walls (interatrial grove) that are separated by vascularized fibrofatty tissues of the extracardiac fat, except for a flap valve that remains from the fetal period together with its anchorage point.

The RA internally exhibits a rough structure (see Figure 2.2) with several PMs originating from another structure called the crista terminalis (CT), the most prominent RA structure, that acts as a boundary inside the atrium [12]. The CT can be seen as a vertical crest (5.1±9 mm length, and 5.5±1.3 mm width) that unites internally the right atrial appendage and the smooth venous part. The PMs fan out from the crest and run towards the vestibular portion. In the RA resides the sinus node, a functional structure located in the junction of the superior cava vein (SCV), that is the source of the cardiac impulse. The sinus node can be seen as the pacemaker of the conduction system of the heart. It is also known as sino-atrial node (SAN), and it has a spindle-shaped structure with a tail that extends towards the inferior cava vein. At the SAN periphery specialized cardiomyocytes and working myocardium are mixed, where the SAN can present multiple extensions radially into the crest and towards the epicardium of the SCV. We will revisit the SAN later on due to its importance in cardiac electrophysiology [13].

Another related area of importance from the electrophysiology point of view in the RA is the triangle of Koch. It is bordered by the attachment of the septal leaflet of the tricuspid valve, the orifice of the coronary sinus (collects almost all of the deoxygenated blood from the vasculature of the heart) and the site of penetration of the bundle of His. At the apex of the triangle of Koch, it is located the atrioventricular node (AVN), that is the only electrical communication path between atria and ventricles. The AVN is formed by a compact region and areas of transitional cardiomyocytes, surrounded by connective tissue in a proportion higher than in other parts of the atria. Its main function is to receive the electrical impulse from the surrounding atrial tissue that arrives into the AVN compact region, to propagate it to the His bundle located in the ventricles. In normal conditions, the bundle is the only electrical pathway for electrical conduction to the ventricles. Note that this structures can only be differentiated using microscopy imaging combined with specific stains, and therefore cannot be observed invivo. To include some important heart structures such as the AVN in a computer model of the heart and reproduce their function, we have to rely on exvivo studies performed in populations.

The region of the RA enclosed by the tricuspid valve and the orifice of the ICV forms an isthmus [14]. Note that, in patients with atrial flutter, this region has a slower conduction velocity [15] and is therefore a substrate for macro-reentries and a target of RFA [14].
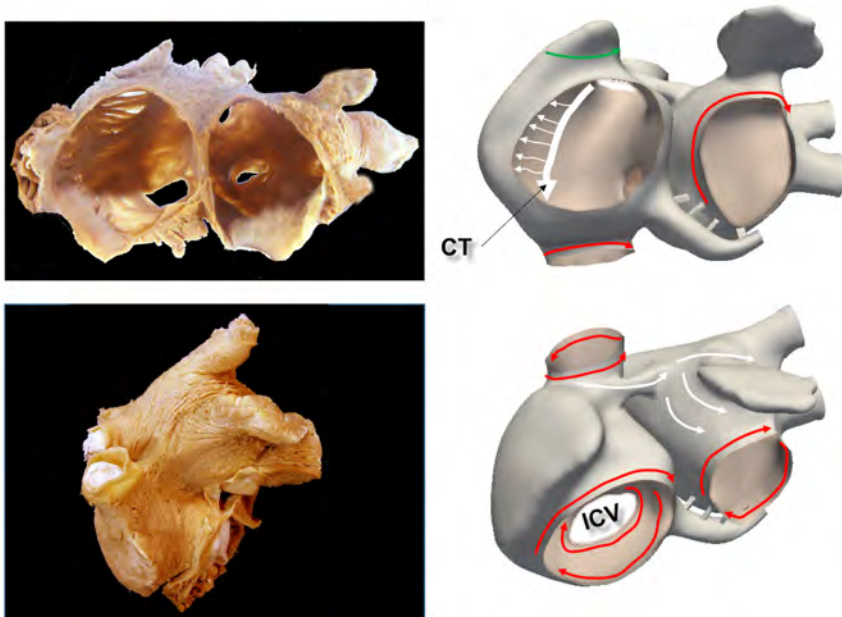
Figure 2.4: View of the fiber orientation in the RA endocardium in an photography and on a 3D model and the area close to the veins and valves. Courtesy of Damian Sanchez-Quintana

Myoarchitecture of the Atrial Walls

The cardiomyocytes that make up the heart walls show a complex organization, that is far from homogeneous along its structures or regions. The term "fibers" describes the macroscopic appearance of strands of cardiomyocytes. Their alignment defines the longitudinal axis along which the electrical impulse is favored, since depolarization signals travel faster in some preferential directions than others. In the atria there are individual variations from heart to heart. Only histological techniques can reveal with enough detail the arrangement of those cardiomyocytes, although some promising imaging techniques such as diffusion-tensor MRI or microCT can provide very good approximations from exvivo atria and ventricles [16]. Modelers that want to take into account the myofiber architecture need to analyze exvivo samples and impose those fiber orientations learned from a few cases into their three-dimensional models. We are going to review the principal fiber orientation in the different regions of the atria.

In general, the macroscopic appearance of muscle bundles in the atria re-

veals three main orientations: circumferential, longitudinal, and oblique. Figures 2.4 and 2.5 show with arrows the principal myofiber orientation in various regions of the atria. The preferential and fast conduction pathways in the atria show a longitudinal myofiber orientation. That is the case of the CT, the BB and the PMs, that have an elongated or tubular shape, with the fibers aligned in parallel and longitudinally relative to the long axis. In the RA wall, however, the tissue that is not part of the PMs shows an irregular orientation of the fibers, intermingling horizontal with oblique or longitudinal myocytes. Other regions of the RA such as those adjacent to the orifice of the veins, ICV and SCV, or the vestibule where the TV is attached have a particular circumferential fiber orientation that arranges the cardiomyocytes around the oval morphology. In the LA the BB extends splitting in two limbs that embrace the LAA, passing to either side of the neck of the appendage, and reuniting as a broad band that runs circumferentially around the LA inferior wall. From the LA septal wall myofiber bundles emerge and extend towards the LA roof, reaching the superior PVs where their organization becomes circumferential in the epicardium. From the PVs and from the area right around them, the myofibers turn toward the center of the LPW, where they fuse and descend towards the inferior region.

2.1.2 Specialized Atrial Tissues

The effective pumping action of the heart requires a precise coordination of the myocardial contractions (millions of cells), and this is accomplished via the conduction system of the heart. Contractions of each cell are normally initiated when electrical excitatory impulses (APs) propagate along their surface membranes. The myocardium can be viewed as a functional syncytium; APs from one cell conduct to the next cell via the gap junctions. The gross anatomy of the cardiac conduction system (CCS) has been widely studied, specially its suprahisian (above the His bundle) structures owing to their clearer implications in supraventricular rhythm disorders and the complexity of the CCS at distal sections.

The fundamental function of the specific cardiac conduction tissue is to trigger and spread at fast speeds the electrical impulse responsible for the heartbeat, maintaining the heartbeat at an average of 60-90 beats per minute in an adult heart normal. The different elements of the specific cardiac conduction system are responsible for the generation and maintenance of the cardiac cycle. The effectiveness of the cardiac contraction depends on the
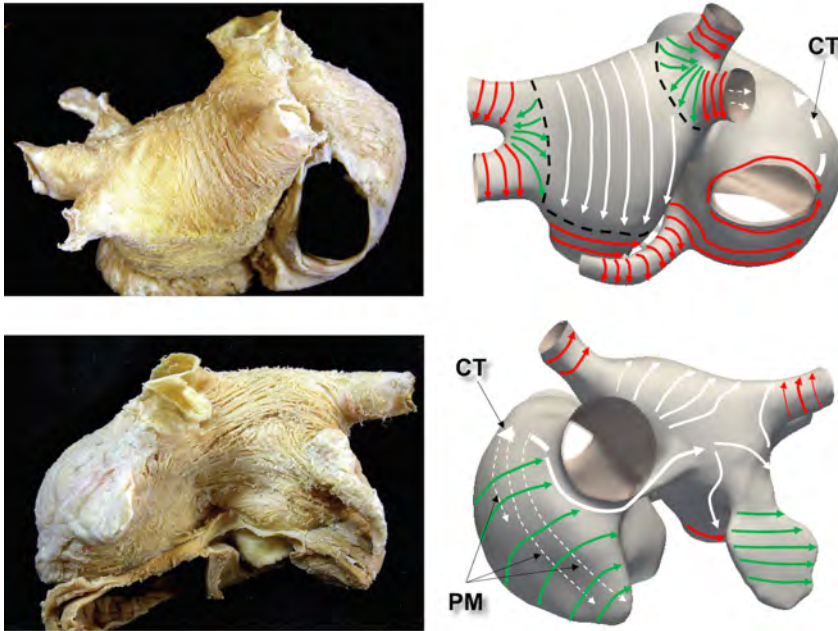
Figure 2.5: View of the fiber orientation in different epicardial regions. Courtesy of Damian Sanchez-Quintana

coordinated sequence of the different events of the cardiac cycle. The atrial contraction must happen before the ventricular, which in turn must first occur at the level of the papillary muscles, extending from there to the ventricular apex and then to the ventricles and pulmonary and aortic outflow tract. These components of the CCS are: the sinus node (sinoatrial or Keith and Flack node), the atrio-ventricular node (Tawara node), the penetrating bundle of His, the right and left branches of the bundle of His and finally, the Purkinje network. Those components are formed by three cell types morphologically different from the cells that make up the "working" myocardium: P cells, transitional cells and Purkinje fibers.

The electrical impulse is generated in the P cells located in the SAN, and it is transmitted to the AVN, where a conduction delay occurs, which allows the atria to contract completely before the ventricles start to contract. The depolarizing impulse is transmitted then to the bundle of His and its branches and, finally, the Purkinje fibers, which distribute the cardiac impulse to the apex and from there extend along the ventricular walls, thus causing ventricular contraction. The transitional cells connect the specific

tissue of conduction to the working myocardial cells.

The Sinus Node

The SAN is also called the Keith and Flack node because it was first described by both in 1907. It is the pacemaker of the heart, that is, its cells are responsible for the start of the cardiac impulse. It is situated in roughly the same location in all hearts: high on the right atrial wall near the junction of the superior vena cava and the right atrium. At the boundaries of the node in the human heart, short areas of histologically transitional cardiomyocytes insert into the musculature of the terminal crest [17]. Conduction spreads through the atria to the AVN and then to the His bundle (HB), which is the normal conducting pathway from the atria to the ventricles. During an extended period of time, it was believed that a specialized insulated pathway existed between the SAN and the AVN. In reality it does not exist, however, there are preferential conduction pathways that permit to transmit rapidly the electrical impulse generated by the SAN to the AVN. The main pathways are the crista terminalis (CT) and the margins of the FO. The PMs also transport the electrical impulse at higher speeds within the right atria, while the Bachmann's bundle (BB) is the preferential fast connection towards the LA. In addition to the BB, the electrical impulse can also access the LA via its connections to the CS. It is important to remark that this connection might be not electrically functional in some people, and can be easily affected by fibrotic tissue.

The Atrioventricular Node

The AVN and HB are typically located subendocardially in the RA within a region known as the triangle of Koch, which is delineated by the coronary sinus ostium, the membranous septum, and the septal/posterior commissure of the tricuspid valve. At the histological level, the AVN consists of a compact portion and an area of transitional cells, which establish contact with the working myocardium. The AVN delays the cardiac impulse prior to its propagation through the ventricular conduction pathways.

The atrioventricular conduction axis has atrial, penetrating, and ventricular components. The cells of the penetrating part become insulated from the atrial myocardium by the fibrous tissues of the atrioventricular junction. In the human heart, the penetrating part or HB, is a relatively short column of

longitudinally oriented and histologically specialized cardiomyocytes. The HB continues as a short non-branching segment that gives rise to the fascicles of the left bundle branch (LBB). The right bundle branch (RBB) takes its origin from the most distal left-sided fascicles, located beneath the septum on its left side, and courses buried through the septum towards the RV.

2.1.3 Atrial Fibrosis

The major non-myocyte population of cells in the heart are the fibroblast, although they represent a smaller volume compared to the myocytes. Fibroblast synthesizes the extracellular matrix and collagen and plays a critical role in wound healing. The main function of fibroblasts is to maintain the structural integrity of connective tissues by continuously secreting precursors of the extracellular matrix. Fibroblast can differentiate into myofibroblast that are involved in wound tissue healing.

Myofibroblast are non-excitable tissue, but it has been recently shown that they can interact electrically with surrounding myocytes, affecting their normal function [18, 19]. Experimental studies have provided convincing evidence that fibrotic transformation of atrial myocardium results in deterioration of atrial conduction. Fibrosis increases the anisotropy of the impulse propagation and can build barriers that promote re-entry in the atrial walls. In addition, fibrosis may be directly involved in the mechanisms responsible for maintaining atrial arrhythmias [20].

Pathological states are frequently associated with myocardial remodeling involving fibrosis. This is observed in ischaemic and rheumatic heart disease, inflammation, hypertrophy, and infarction. The growth in fibrous tissue content is based on the maintained proliferative potential of fibroblasts (largely absent in myocytes of the adult heart [21]), and the synthesis of extra-cellular matrix (ECM) proteins, predominantly by fibroblasts [22]. Structural remodeling has been observed both clinically and experimentally, and is an important feature of the AF substrate, producing fibrosis that alters atrial tissue composition and function. The precise mechanisms underlying atrial fibrosis are not fully elucidated, but recent experimental studies and clinical investigations have provided valuable insights [23].

Experimental and numerical studies have shown that the texture and spatial distribution of fibrosis may play an important role in arrhythmia onset.

Spatial heterogeneity of fibrosis increases the probability of arrhythmia induction. This effect is more pronounced with the increase of both the spatial size and the degree of heterogeneity [24].

Late Gadolinium enhancement (LGE) MRI has the potential to image regions of low perfusion, which can be related to fibrosis. LGE-MRI enables to distinguish diseased myocardium from normal myocardium by utilizing slow washout kinetics of gadolinium in diseased tissue. For some time, LGE-MRI has been used for detecting fibrosis in the LV in conditions such as myocardial infarction, dilated cardiomyopathy, and hypertrophic cardiomyopathy. Extensive atrial tissue fibrosis identified by delayed enhancement MRI has been associated with poor outcomes of catheter ablation [25].

Computational studies on patient-specific atrial models including fibrosis derived form MRI have confirmed that rotors stabilize in the border zones of patchy fibrosis in 3D atria, where slow conduction enable the development of circuits within relatively small regions [26]. However, in the diffuse fibrosis models, waves randomly meandered through the atria, whereas in each the patient-specific models, rotors stabilized in fibrotic regions.

Anatomic targeting of LGE-MRI-detected gaps and superficial atrial scar is feasible and effective to treat recurrent arrhythmias post-AF ablation. Homogenization of existing scar is the appropriate treatment for recurrent AF, whereas dechanneling of existing isthmi seems the right approach for patients recurring with AT [27].

2.2 Cardiac Electrophysiology

Cardiac electrophysiology is the science of elucidating, diagnosing, and treating the electrical activities of the heart. One of its goals is to assess complex arrhythmias, elucidate symptoms, evaluate abnormal electrocardiograms, assess risk of developing arrhythmias in the future, and design treatment. In the next sections, we review cardiac electrophysiology at cellular, tissue and body scale. All scales are inter-related and depend on each other, so that a mutation or fibrosis at cellular level that affects an ionic channel can modify the morphology of the electrocardiogram at body surface level.

2.2.1   Cardiac Cell Action Potential

Cells can build an electrical potential difference, known as the resting membrane potential, between the inside and outside of the cell through the action of ion pumps and ion selective channels. Cells can have a variety of ion selective channels in their membranes, but the main ion species involved in cardiac electrophysiology are sodium (Na^+), potassium (K^+), and calcium (Ca^{2+}). The channels are said to be gated because a trigger is needed for opening a given channel. The ion channels in the cardiomyocytes are voltage-gated ion channels, so they are activated by changes in the electrical membrane potential near the channel. The membrane potential alters the conformation of the channel proteins, regulating their opening and closing. The opening and closing of the channels are triggered by changing ion concentration, and hence charge gradient, between the sides of the cell membrane.

There are two forces acting on the ions, chemical and electrical forces. Chemical forces act against the concentration of a particular ion species, flowing down the concentration gradient and favoring a uniform solution. Electrical forces try to balance the cation and anion concentrations. Therefore, the movement of ions across the cell membrane causes changes in electrical gradient that act to oppose the chemical gradient. In resting state, the cell has an intracellular negative charge with respect to the extracellular space, that is typically around -85 mV. In that state, the main ion in the extracellular space is sodium (Na^+), whereas in the intracellular space is potassium (K^+). Note that apart from the electrochemical gradients there are energy consuming mechanisms such as ATP-dependent ion pumps that maintain the negative transmembrane potential.

Action Potential Phases

A current movement through the gap junctions that increases the transmembrane potential above a critical point known as threshold potential will trigger the action potential (AP) initiation. Note that if the current does not reach the required minimum threshold, the cell will respond passively, and no AP will be generated, which protects the cell to small perturbations. When a sufficient large stimulus is given (threshold is about 40mV above the resting potential) voltage-dependent Na^+ channels open, causing a transient increase in sodium permeability and a rapid influx of sodium
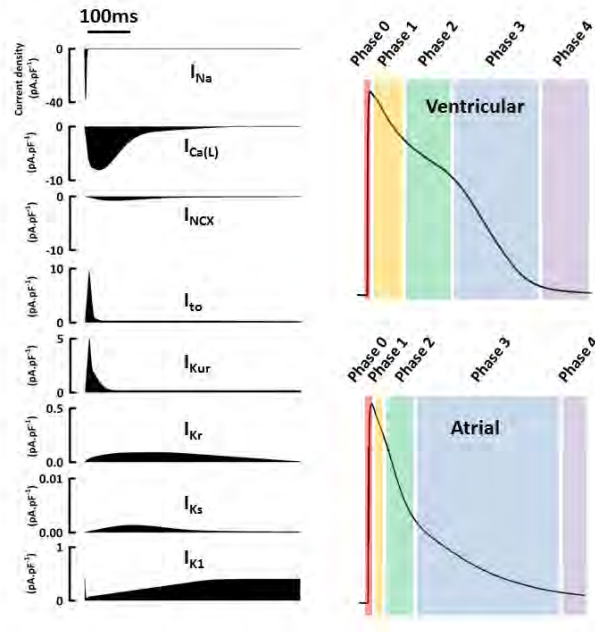
Figure 2.6: Action potentials recorded from sheep atrial and ventricular cardiomyocytes with phases shown. Ion currents approximate to ventricular action potential. Source: https://commons.wikimedia.org/

ions, which starts the depolarization of the cell. At that point the membrane potential moves very rapidly to the (positive) sodium equilibrium potential, since at positive potentials the membrane is highly permeable to sodium ions.

AP initiation will affect other cell ion channels, in particular it will activate voltage-gated Ca^{2+} and K^+ channels. An important channel is the voltage-gated L-type calcium channel that allows calcium to enter the cell, sustaining the depolarized state when sodium channels close. Finally, the voltage-gated K^+ channels open after some delay to move potassium ions down its concentration gradient, that is from intracellular to extracellular space. This drives the cell again toward the negative resting state, and is called repolarization.

To better understand the generation of the AP and the return to the resting state the process is usually divided in phases (see Figure 2.6).

Phase 0 corresponds to the rapid depolarization phase, where the opening of voltage-gated Na^+ sodium channels generates the sharp upstroke and

23

favor rapid conduction velocity. These channels usually open due to an AP that arrives from neighboring cells through gap junctions, that increases the intracellular voltage over the triggering threshold. Subsequently a large influx of sodium into the cell increases the voltage. Upstroke duration in ventricular and atrial cells lasts less than 2ms, while other cells such as pacemaker cell (e.g. SAN cells) is 10-20ms. The main reason for that difference is that the increase in membrane voltage in pacemaker cells is due to the activation of calcium channels, that are slower than the sodium ones.

In phase 1, sodium channels begin to close, producing a rapid decrease in sodium influx into the cell, and the subsequent reduction in the membrane potential. At the same time outward K^+ current (I_{to} current) due to potassium ions flowing outside the cell produces a fast decrease in the membrane potential for a short time period. This phase can be observed in the AP waveform as a notch.

During phase 2 of the AP, called plateau phase, the membrane potential remains stable, and begins to slowly repolarize. In this phase, activated L-type Ca^{2+} channels produce a small influx of Ca^{2+} into the cell (I_{CaL} current), which triggers a much larger Ca^{2+}-induced Ca^{2+} release from the sarcoplasmic reticulum through the cardiac ryanodine receptors. However, there is a balance between calcium and potassium channels, that keep moving ions K^+ outside the cell (I_{ks} current) through the slow delayed rectifier potassium channels. In addition, although it plays a secondary role, the activity of the sodium-calcium exchanger and the sodium-potassium pump increases due to the increased of calcium and sodium concentrations, respectively.

In phase 3, there is a rapid depolarization, due to the closing of the L-type Ca^{2+} channels, and the increased effect of the slow delayed rectifier current (I_{ks} current). As the transmembrane potential decreases due to the outflow of positive ions (K^+), more potassium channels activate, the rapid delayed rectifier K^+ channels (I_{Kr}) and the inwardly rectifying K^+ current, I_{K1}. The sustained outflow of potassium (loss of positive charge from the cell) causes the cell repolarization.

Finally, in phase 4 the membrane stays in a resting state, the delayed rectifier K^+ channels close, and only the I_{K1} remains active to reach the final resting potential state. Ion pumps also remain active throughout phase 4, to reset the resting ion concentrations, e.g. the calcium that caused the cell to contract is pumped out of the cell.

Note that from the initiation of the AP through approximately half of the repolarization, the cell is considered refractory, and cannot respond to a new depolarization signal. Cardiac cells have two refractory periods, the absolute refractory period for which it is impossible for the cell to produce another AP (sodium channels are inactivated), and a relative refractory period (until end of phase 3), during which a stimulus of greater intensity than a regular one can trigger another AP. These mechanisms protect the cell and the whole heart, impeding too fast heart rhythms under normal conditions.

Action Potential Heterogeneity

The timing of repolarization is known to vary in different regions of the heart, mainly due to differences in isoforms of the Ca^{2+}, and K^+ channel proteins in each cell. The fundamental differences can be found between working cardiomyocytes and specialized cells that form part of the cardiac conduction system (nodal cells and conduction cells). For instance, phase 1 and 2 of the action potential are not present in pacemaker cells. In addition, other currents such as the so-called funny current (I_f), specific for pacemaker cells, are due to channels that allow the pass of both Na^+ and K^+ at very negative membrane potentials. The activity of these channels in the SAN cells causes the membrane potential to depolarize slowly and so they are thought to be responsible for the depolarization automaticity. In summary, action potentials from cells that form part of the specialized conduction tissues are characterized by a slower initial depolarization phase, a lower amplitude overshoot, a shorter and less stable plateau phase, and repolarization to an unstable, slowly depolarizing resting potential. Note that there also exist differences within each cell type as a function of its location in the heart, but these are smaller in comparison to other cell types.

There has been described different spatial variations of the action potential waveform in the atria. Measurements performed in isolated cells, sometime in animals, are difficult to measure invivo, where the electrotonic currents exchanged between neighboring cells tend to mask the individual differences in action potential. Right versus left heterogeneity has been described, with differences in the AP between cells in the RA and LA. All these differences in action potential duration can be arrhythmogenic, since spatial dispersion of the APD can lead to temporal dispersion of repolarization, and a premature

Figure 2.7: Ordered sequence of electrical activation of the atria in sinus rhythm. Arrows point to the main direction of the depolarization wavefront divided in 10 sequential steps.

stimulus (ectopic focus) can result in a local functional block initiating electrical reentry.

Atrial Sequence of Activation

The contraction of the atria and the ventricles is carefully regulated by the transmission of electrical impulses that result from the propagation of the AP throughout the heart. Unlike the AP in skeletal muscle cells (initiated by nervous activity), the cardiac AP is initiated by the SAN, that have automatic AP generation. The frequency of depolarization of the SAN is modulated by both sympathetic and parasympathetic efferent innervations. Note that under pathological conditions the initial AP can be triggered from focal ectopic activity in any region of the atria. Under that circumstance, the SAN function can be canceled by the faster trigger.

After pacemaker cells trigger the initial depolarization, the electrical impulse travels very fast within the cardiac conduction system in a coordinated

fashion. It is important to point out that in the atria there are not explicit structures that compose the conduction system as happens in the ventricles, but preferential anatomical conduction pathways. Therefore, after the initial impulse passes from the SAN to the adjacent myocardial tissue, it propagates faster through well-organized regions such as the CT, or the BB (see Figure 2.5). CT has a myofibers organization that favor the conduction from the SAN to the atrioventricular node region faster than other surrounding tissue. At the same time, BB provides a fast transport of the electrical impulse from the SAN to the LA. Therefore, we could say that in the atria the fast pathways are due to well organized myofiber routes, instead of independent specialized structures. In addition to the depolarization through these pathways, general excitation also spreads from cell to cell throughout the atria, and it is affected by the alignment of myofibers in each atrial region.

The sequence of activation of the atria is deterministic and can be described by measuring at which time the depolarizing wavefront arrives at each region (see Figure 2.7 arrows) [28]. The activation starts form the SAN, the first region that activates (rates between 60 and 100 beats per minute). After the SAN starts the activation (t = 0 ms), the electrical signal travels fast through the CT, depolarizing almost simultaneously the right side of the BB, and the SCV. For the next 57 ms, the activation continues rapidly through the CT towards the IVC (see Figure 2.7, arrow 1), which activates one by one the PMs as the wavefront encounters them, together with the endocardial wall of the intercaval region. This activation pattern produces a triangular wavefront that spreads from the CT to TV through the RLW and the RAA for 85 ms (see Figure 2.7, arrow 2). The right side of the atrial septum is activated by the intercaval bundle at t = 20 ms, which allows a second wavefront to spread with lower conduction velocity from the CT to the TV (see Figure 2.7, arrow 3). Both wavefronts collide in the TV (see Figure 2.7, arrows 2 and 3), the last right atrial region activated, and thus produce the last activation time registered in the right atrium at t = 109 ms [29].

The RA starts its activation in parallel to the LA with a delay of approximately t = 38ms. The activation wavefront from the LA arrives first to the RA through the the right side of the BB (see Figure 2.7, arrow 4). From there, the activation spreads simultaneously on the left superior wall and regions around the LAA. The left side of the atrial septum is partially activated by the left side of the BB (arrow 5) and partially by the left side of the FO, 10 ms later. These LA activation produce four wavefronts at t

27

= 64 ms, which advance simultaneously towards the mitral valve (see Figure 2.7, arrow 5), the union between the superior and inferior RPV (see Figure 2.7,arrow 6), the LPV (see Figure 2.7, arrow 7) and the left atrial appendage (see Figure 2.7, arrow 8). The LAA shows a slow conduction velocity, since the depolarization wavefront travels perpendicularly to the local fiber direction, taking 61 ms to be completely depolarized. In the posterior wall, the LPW depolarization sequence depends on two wavefronts, one arriving from the left superior wall (see Figure 2.7, arrow 7) and the other crossing the RPV (see Figure 2.7, arrow 6). This causes a diagonal wavefront (see Figure 2.7, arrow 9) that electrically sweeps the posterior wall from the SRPV towards the ILPV for 64 ms.

The distal regions of the CS (see Figure 2.7, arrow 10) are depolarized together with the left superior wall but with a slower conduction velocity due to the circular fiber direction. The latest activation time registered in the atria corresponds to t = 132 ms and is concurrent with the latest activation of the coronary sinus.

Toward the end of atrial depolarization, the excitatory signal crosses the AVN. Since the atria and ventricles are electrically isolated from each other by dense connective tissue rings, the atrioventricular node located in the triangle of Koch is the only conduction pathway between upper and lower chambers. The AVN has the mission of delaying the electrical signal before transmitting it to the ventricle. This will allow the atria to completely pump the blood into the ventricles, since simultaneous contraction would cause inefficient filling and backflow. It is worth to mention that in pathological conditions (e.g. Wolff-Parkinson-White syndrome) there exist aberrant paths between the atria and ventricles such as the bundle of Kent. The atrioventricular node also present depolarization automaticity, but with a slower frequency (40 to 50 beats per minute) than the SAN. Following atrioventricular nodal excitation, impulses continue down to the HB to activate the ventricles.

2.2.2 The Electrocardiogram

The ECG is an inexpensive non-invasive diagnosis tool, virtually available to any clinician, that has been extensively used by cardiologist to assess cardiac function from the electrical perspective. Nevertheless, it has important limitations since it is difficult to infer cardiac status from a short
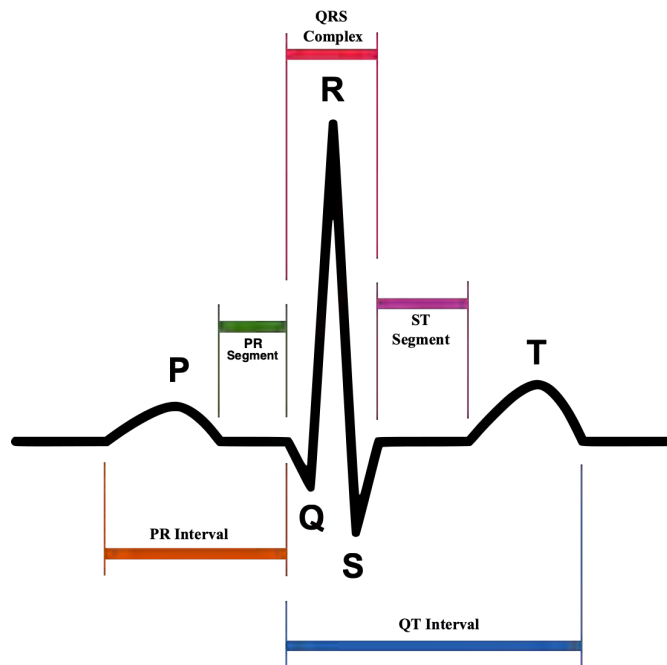
Figure 2.8: Schematic diagram of normal sinus rhythm for a human heart as seen on ECG. Source: https://commons.wikimedia.org/

time window, especially when there is presence of ischemia or non-chronic arrhythmias.

Over the last decade there have been other important advances that have favored the advance of diagnostic tools for cardiology, such as echocardiography, MRI or EAM, that complement the information provided by the ECG.

12-Lead ECG

There are different configurations used to study the electrical activity of the heart, being one of the most standard the 12-lead electrocardiogram. It requires to place ten electrodes on the skin of a subject, that are typically conductive pads in contact with the body that make an electrical circuit with the electrocardiograph. ECG leads are computed by comparing the electrical currents measured at several electrodes. The computed waveform features depend on the amount of cardiac tissue involved, as well as the relative orientation of the electrodes with respect to the major dipoles in

the heart. The 12-lead ECG consists of two sets of ECG leads: limb leads (bipolar), augmented lead leads (unipolar) and chest leads, often called precordial leads (unipolar). The bipolar limb leads usually referred to as Lead I, II and III, form on the torso an equilateral triangle (Einthoven's triangle). The three electrodes are the vertices of the triangle, placed on both arms, avoiding thick muscle, and on the left leg, lower end of medial aspect of calf muscle. Traces are measured along the sides of the triangle. Lead I is obtained as the voltage difference between the left arm (LA, positive) and the right arm (RA, negative). Lead II is the difference between left leg (LL, positive) and right arm (RA, negative). Finally, Lead III is the voltage difference between the left leg (LL, positive) and the left arm (LA). The augmented limb leads are referred to as aVR (augmented vector right), aVL (augmented vector left) and aVF (augmented vector foot). They are obtained from the same electrodes as Leads I, II and III, but they use Goldberger's central terminal as their negative pole. Goldberger's central terminal is a combination of two limb electrodes, with a different combination for each augmented lead.

The precordial leads lie in the horizontal plane. The precordial electrodes act as the positive pole for the six corresponding leads (V1, V2, V3, V4, V5 and V6), while the Wilson's central terminal is used as the negative pole. Wilson's central terminal VW, is produced by averaging the measurements from the electrodes RA, LA, and LL.

The precordial electrodes are located as follows: V1 in the fourth intercostal space (between ribs 4 and 5) just to the right of the sternum (breastbone); V2 in the fourth intercostal space (between ribs 4 and 5) just to the left of the sternum; V3 between leads V2 and V4; V4 in the fifth intercostal space (between ribs 5 and 6) in the mid-clavicular line; V5 horizontally even with V4, in the left anterior axillary line; V6 horizontally even with V4 and V5 in the midaxillary line.

As the ECG is recorded, signals of voltage (mV) over time (seconds) are produced and usually displayed in the electrocardiograph. The signal waveform at each lead has a typical known signature, with peaks and waves that correspond to depolarization and repolarization phases. First of all, we are going to describe why the signals have positive or negative polarity and after we will review the different segments that conform the ECG waveform.

When a depolarizing wavefront advances through tissue, it creates a moving dipole between the tissue at rest (negative potential, -85mV) and the depolarized tissue (positive potential, +35 mV). If the depolarizing wavefront

advances in the direction of our positive electrode, we obtain a positive deflection. If the depolarizing signal moves away from the positive electrode, we obtain a negative deflection. The effect inverts during repolarization, so that, a negative deflection is obtained if the repolarization wavefront moves towards the positive electrode, and a positive reflection if it moves away from the electrode. Therefore, the overall direction of depolarization across the heart produces a vector that gives rise to positive or negative deflections on the ECG with respect to a given positive electrode.

The first milliseconds of the cardiac activation, that correspond to the SAN depolarization, are not visible in the electrocardiogram since the amount of cells depolarized is not big enough to produce detectable potentials on torso electrodes. As the depolarization wavefront advances through both atria, downwards and from right to left, a wave called the P-wave, is created in the electrocardiogram (see Figure 2.8). It usually has a duration of 80-100ms that corresponds to the period in which the electrocardiograph can detect the potential produced by the atrial activation. During this period the cardiac dipole points downwards and to the left producing positive deflections in leads I, II, and III with different amplitude.

While the AP reaches the atrioventricular node, and crosses it to spread through the HB and the bundle branches, the electrocardiogram signal stays at baseline. Following, the Purkinje system starts activating the tissue of the LA and RA. The septum in the LV activates first causing an activation from LV to RV that produces a negative deflection in leads I and II, and positive in lead III, known as Q-wave. Following activation advances from endocardium to epicardium in the apical part, and extends to the lateral wall of both ventricles causing a large positive deflection (especially in leads I and II), the R-wave. Finally, the basal region of the lateral wall of the LV depolarizes causing a negative deflection called the S-wave. All together the activation sequence of the ventricles form the well-known QRS complex. After the QRS complex, the electrogram signal returns to the baseline, the ventricular repolarization phase is produced from the epicardium to the endocardium, and gives rise to the T-wave, which is positive in leads I and II, and negative in lead III. The repolarization of the atria is masked by the large QRS complex, and therefore cannot be observed.

ECGi

Electrocardiographic imaging (ECGI) is a imaging modality for cardiac electrophysiology and arrhythmias. It reconstructs cardiac potentials, electrograms, and isochrones from electrocardiographic body-surface potentials non-invasively. The basic ECGI methodology involves solving the electrocardiographic inverse problem, which can be defined as the computation of epicardial potentials from body surface potentials. This inverse problem is ill posed in the sense that small perturbations in the data (e.g., measurement noise or geometrical errors that are practically inevitable) can cause large unbounded errors in the solution. Accuracy depends on a priori knowledge of solution characteristics and determination of an optimal regularization parameter [2].

2.2.3 Atrial arrhythmias

Cardiac arrhythmia is a condition in which the heart rhythm is irregular and beats systematically faster or slower than the normal range of 60-100 beats per minute at rest. Faster rhythms are called tachycardia, and slow rhythms bradycardia. It is considered an electrical disorder, which compromises cardiac mechanics and affects the heart pumping efficiency. The term cardiac arrhythmia covers a very large number of very different conditions. The most common way to diagnose an arrhythmia is by evaluating the patients' ECG, which can be complemented by an eco-cardiographic study, and in specific cases with an electro-anatomical map before a RFA intervention. The most common treatments for arrhythmia include, the use of drugs (beta blockers, blood thinners), implantation of pacemakers and intra-cardiac defibrillators (cardiac resynchronization therapy), and surgery (radio-frequency ablation).

Apart from the classification as a function of the heart rate in tachycardia and bradycardia, arrhythmia can be analyzed by i) mechanism [30]: automaticity, re-entry, triggered; ii) duration: paroxysmal, sustained, permanent; iii) site of origin: atria, ventricles, conduction system. Other causes of arrhythmia include congenital heart defects present from birth that affect heart structure or electrical pathways. Among them, there are Wolff–Parkinson–White syndrome, Long QT Syndrome or the Brugada Syndrome.

Heart tachycardia

Tachycardia results from abnormal impulses triggered in the heart that result in fast rhythms, above 100 beats per minute, which can range from 140 - 200 beats per minute. It should not be confused with fast heart rates due to physical exercise, emotional stress, or ingestion of substances such as caffeine. Although a few seconds may not result in problems, longer periods are dangerous There are three basic mechanisms that can elicit heart tachycardia: automaticity produced by ectopic focus, re-entrant activity produced by rotors and spiral waves, and triggered activity produced by cell afterdepolarizations. All these mechanisms happen in both atria and ventricles. Tachycardia might degrade into fibrillation due to the electrical changes at ionic level produced by sustained fast heart rhythms. Heart tachycardia can be classified as non-sustained, if the fast rhythm self-terminates within 30 seconds, or sustained if it lasts more than 30 second.

Atrial tachycardia

In general, all atrial tachycardias are also known as supraventricular tachycardias. They can be classified as focal or macro-reentrant, depending on their origin and propagation of the electrical impulse. When the source of the tachycardia is an ectopic focus, e.g. focal atrial tachycardia (FAT), the electrical impulse comes from an abnormal pacemaker rather than the SAN. The aberrant pacemaker fires the activation faster than the SAN, which blocks completely its function. In addition, it changes the normal activation sequence since it can be located at any point in the atria, although there are some areas with higher prevalence such as the PVs.

Focal AT (FAT) are caused by automatic triggering, or micro-re-entrant mechanisms (see Figure 2.9). FATs are characterised by radial, circular, or centrifugal spread of activation from a single focus or point source and the activation is shorter than the flutter case (i.e., it is a short activation; there is no activation spanning the whole tachycardia CL) [31]. The source of the tachycardia can be also multiple, as in multifocal atrial tachycardia, which is common in older people that suffer from chronic obstructive pulmonary disease. Multifocal atrial tachycardia is characterized by an electrocardiogram (ECG) strip with 3 or more P-waves of variable morphology and varying P–R intervals, plus tachycardia. The reason of this particular ECG is that the location of the source of activation can change from one ectopic focus to the next one.

FAT often originates from well-characterized sites within the LA and RA such as the tricuspid annulus, CT, PVs, ostium of the CS, and mitral annulus [32, 33, 34, 35, 36].

Another type of supraventricular tachycardia that can happen in subjects with cardiovascular disease and spontaneously healthy ones is known as atrial flutter. It is caused by a reentrant rhythm initiated by a premature impulse or an ectopic focus. Following, it is sustained due to differences in the refractory periods of adjacent tissue regions that generates a localized self-perpetuating loop. There are two types of atrial flutter, Type I or typical flutter, and Type II or atypical flutter. Typical flutter is characterized by a reentrant loop that circles the RA, passing through the cavo-tricuspid isthmus, and can turn clockwise and counterclockwise. Atypical flutter describes more complex loop pathway and is usually faster.

Atrial tachycardias, excluding atrial flutter, are thought to represent about 5% to 15% of sustained supraventricular tachycardias in the adult, and are more frequent in the pediatric population. The treatment of atrial tachycardias is focused on rhythm control and prevention of arrhythmia recurrence. Patients with multiple comorbidities and contraindications for antiarrhythmic drugs should be treated with an invasive strategy. Persistent tachycardias with hemodynamic compromise must be terminated emergently with electrical cardioversion.

2.2.4 Radiofrequency ablation

Catheter ablation is a minimally-invasive surgical procedure that aims to terminate a faulty electrical pathway in the heart of subjects prone to develop cardiac arrhythmias such as atrial fibrillation, atrial flutter, atrial tachycardia, ventricular fibrillation, ventricular tachycardias or Wolff Parkinson White syndrome. It involves introducing several flexible catheters through the femoral vein (or the subclavian vein), and advance them towards the heart chambers. Once inside the heart, catheters are used to induce the arrhythmia, which is subsequently stopped by applying local heating or freezing to ablate the abnormal electrical pathways. The ablation basically has as a goal the creation of lesions in the tissue that change the conduction patterns. Catheter ablation is recommended in people with no or little structural heart disease where rhythm control by medication or cardioversion fails to maintain normal heart rhythms (recurrent or persistent arrhythmia), or requires very long drug treatments that prolong for years.
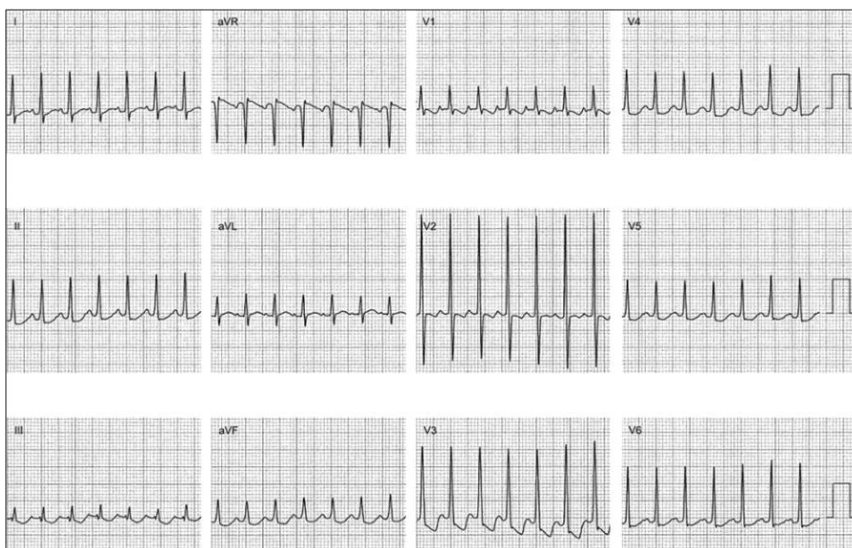
Figure 2.9: Patient presenting with an incessant atrial tachycardia and tachycardia-induced cardiomyopathy. An electrophysiology study demonstrated a focal atrial tachycardia originating in the anterior rim of the fossa ovalis.

The procedure can be classified by energy source: radiofrequency ablation (RFA) and cryoablation.

Before the ablation is performed the electrophysiologist constructs a chamber 3D map, i.e. EAM, (see Figure 2.10), that guides him towards the regions that need to be ablated, as we will see in next section. While originally applied towards relatively straightforward arrhythmias with a single discrete target site (such as atrioventricular nodal reentry or tachycardias associated with Wolff-Parkinson-White syndrome), they are increasingly being used to address more complex arrhythmias, including atypical atrial flutter, atrial fibrillation, and ventricular tachycardia. The greatest impact of EAM is probably its application to facilitate PVI for treatment of AF.

Nowadays, several different EAM systems utilizing various technologies are available to facilitate mapping and ablation. Each EAM system has its strengths and weaknesses, and the system chosen depends upon what data is required for procedural success (activation mapping, substrate mapping, cardiac geometry), the anticipated arrhythmia, the compatibility of the system with adjunct tools (i.e. diagnostic and ablation catheters), and the operator's familiarity with the selected system.
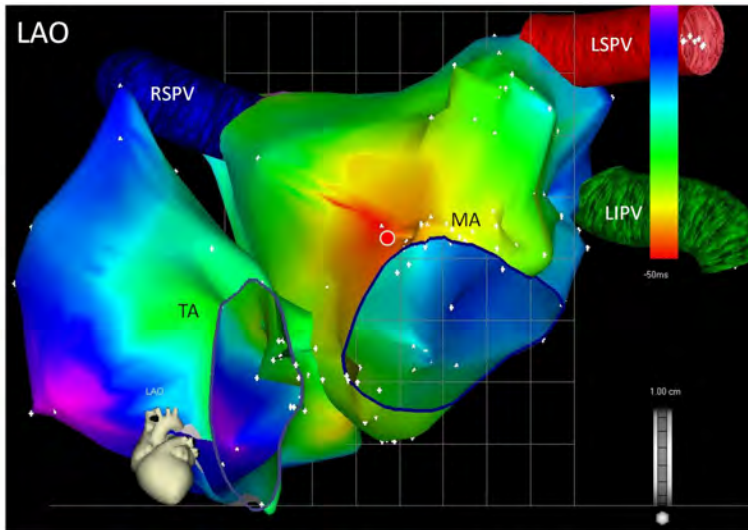
Figure 2.10: Three dimensional non fluoroscopic activation map of a focal atrial tachycardia originating in the mitral annulus-aorta continuity. Both RA and LA are shown with color-coded representation of the timing intervals. The red area represents early activation and the solid circle the earliest area of activation where radiofrequency ablation resulted in termination of the tachycardia. LAO: left anterior oblique. TA: tricuspid annulus. MA: mitral annulus. RSPV: right superior pulmonary vein. LSPV: left superior pulmonary vein. LIPV: left inferior pulmonary vein.

Electrophysiological procedure of FAT

The common clinical treatment for patient with a FAT confirmed by an ECG involves the following steps. First, the patient undergoes an electrophysiological study after cessation of drug administration at least for a period corresponding to 5 half-lives before the study. In the study, a conventional multipolar catheters is placed in the upper RA, the His bundle area and, sometimes, in the CS and the apex of the RV. In cases where tachycardia is not incessant, a programmed atrial stimulation (pace-mapping) is performed with the introduction of extra-stimuli and / or atrial stimulation at different fixed frequencies for the induction of clinical tachycardias, with the infusion of isoproterenol when necessary.

The standardized criteria for the diagnosis of AT and for its characterization as focal or reentrant is as follows. In the case of a FAT, an initial assessment of its atrial origin, left or right, is performed using early criteria in relation to an atrial reference electrogram or the P wave of the surface electrocardiogram. In macro-reentrant TA, in parallel to the EAM, electrophysiologists

search for double electrograms.

2.2.5 Electro-anatomical mapping systems

Radiofrequency (RF) ablation is a clearly established therapeutic option for patients with atrial tachycardia refractory to drug treatment. In these patients, which is a great anatomical variability in the location of the optimal points to perform the ablation, it is especially important to obtain an accurate mapping. So far, this technique has consisted of the use of fluoroscopy in combination with electrogram analysis. However, fluoroscopic localization, even with biplane technique, is not without limitations, in addition to the necessary exposure to ionizing radiation. This technique does not allow to visualize the endocardial surfaces or to precisely locate the tip of the catheter, whose approximate situation is determined according to its relationship with adjacent structures.

With the intention of overcoming these limitations, a non-fluoroscopic electroanatomic mapping system based on a special electrocatheter has been developed in recent years. The so-called EAM system uses an integrated mapping catheter with a location sensor built into its tip to allow automatic and simultaneous acquisition of the electrogram of that position and its three-dimensional location coordinates. The mapping system acquires the electrode location of the catheter tip along with its local electrogram and reconstructs a three-dimensional electroanatomic map of the color-coded cardiac chamber, with relevant and real-time electrophysiological information (see Figure 2.10).

This technique utilizes catheters in an electrophysiological study that records surface electrical activity to identify the location of the VT reentrant circuits, which are then targeted for ablation. However, an electrophysiological study is limited to interrogation of the cardiac surfaces alone, which fails to take into account the complex 3D architecture of the infarct and could lead to missing intramural arrhythmogenic substrates. Additionally, the point by point nature of the technique results in long procedure times that increase risk for complications in patients. These limitations have resulted in a success rate of only 58% for first time VT ablation procedures. Clearly, there remains a need for novel methodologies to safely and effectively identify the specific MI regions that harbor VT reentrant pathways which can then guide successful post-MI VT ablation.

2.3 Computational physiology

Despite technological advances, cardiovascular disease still is the one cause of mortality in the world. Therefore, it is necessary to develop novel methodologies and tools that help us to gain understanding in the pathophysiology of the heart, and at the same time serve to improve patient management, therapy planning, and delivery. The fundamental goal of this technologies is to provide some further knowledge to go from the raw medical data to the construction of personalized biophysical models of the heart for simulation of cardiac electrophysiology.

Over the last years, new medical imaging technologies have allowed obtaining clinical information with a high level of detail, and specific to each patient. The amount of data currently available represents an important opportunity to transform the diagnostic model of cardiovascular diseases through a greater degree of personalization of therapies. However, to improve the understanding of cardiovascular diseases, not only geometric and mechanical information is required, but also a thorough knowledge of the different physics present in the heart (electrophysiology, mechanics, haemodynamics) and physiological information. In this context, a huge amount of information has been generated in recent years at different levels: subcellular, cellular, tissue, organs and systems [37]. An integrative approach is therefore necessary, which must take into account the complex interactions between all components in order to study the origin and maintenance of cardiac arrhythmias in order to improve its prevention [38, 39]. It is of great importance to develop predictive models that integrate information from different levels or spatial scales. These personalized electrophysiological simulations have already shown promising results to support clinical decisions in cardiology [40, 41, 42, 43].

2.3.1 Biophysical models of the heart

A 3D biophysical model of the heart is composed of a 3D geometry, myocardial structure, electrophysiology models at different scales (cell to whole organ models), and specialized structures (e.g. the cardiac conduction system [44]). Depending on the final application of the model, modeling a particular pathology (mutation, alteration of tissue properties, ...) might be also required (see Figure 2.12). As can be inferred from the blocks, this is a very interdisciplinary work that involves clinicians and biologists

to acquire and analyze biological samples, mathematicians and engineers to formalize, develop and implement the computational models, companies that develop implantable devices and drugs, and electrophysiologist that plan and perform interventions, and validate the models.

Over the last years, an extensive number of mathematical models have been built to reproduce the electrical (cardiac electrophysiology) and mechanical (tissue deformation) dynamics of cardiac cells and tissues. The biophysical models of the heart are also starting to be embraced in clinical research environments to assess their predictive capacity for treatment delivery and optimization [45]. The applications are countless, and although they will require a long validation process and acceptance from the clinical community, the initial results are promising. Some of the therapies that could potentially benefit from biophysical models are cardiac synchronization therapy or radio-frequency ablation, among others. In addition, last years advances in computing resources and imaging technologies, have led to the development of patient-specific models. These models, generated using *in vivo* imaging, accurately represent the cardiac anatomy of the subject and incorporate material properties and cardiac features of the patient. Let us review the different components required.

Anatomical models

Three-dimensional models of the heart, and especially the methods and sources of information used in their construction, have evolved enormously since their conception. The specific geometry of the patient's atria and ventricles can be accurately reconstructed from a wide variety of imaging sequences using advanced segmentation tools [46, 47]. For example, radiological image sequences can be processed and segmented using semi-automatic techniques to obtain patient-specific geometrical models that describe the anatomy of the heart and, in some cases, if data are available, include relevant properties such as the pathological substrate, i.e., regions with fibrosis in the atrium or areas of scar in the ventricles [48]. These substrates are highly pro-arrhythmic, and therefore are the target of radiofrequency ablation interventions in clinical practice [45, 49]. In [50], the results of a Grand Challenge focused on efficient algorithms for the segmentation of fibrosis in the atrium from LGE MRI image sequences were evaluated.

The acquisition of medical imaging sequences is not sufficient for the construction of detailed biophysical computational models due to the impor-

tance of cardiac microstructure, which can only be obtained from exvivo invasive studies (for example, histological data or diffusion tensor imaging DTI-MRI). The heart shows a high degree of organization and specialization of the different tissues at the structural level and at the cellular level [51, 52]. In-vivo data from a patient is very valuable, however it must be complemented with ex-vivo population data in order to build complete multi-scale models [53]. These population-based data refer to known common characteristics that are not directly observable in the individual using clinical imaging techniques, but that are present and should be considered. Micro-structural level data is essential for a correct representation and simulation of cardiac electrophysiology. Given the need to include this information, mathematical models have been developed that allow structures to be modeled according to average observations in a given population [54, 55]. For example, the arrangement of myocardial fibers in the ventricles and atria can be characterized by histological techniques for each region of the heart [56, 13]. These descriptions are then tailored to a segmented cardiac model of a specific patient, using rule-based mathematical models [57, 58]. In the modeling of the heart it is also essential to include preferential conduction beams, such as the Purkinje network, the CT or the Bachmann's bundle.

Electrophysiological cellular models

At this point it is important to differentiate between the so-called phenomenological models and the predictive models. Phenomenological models are often macroscopic representations of a given phenomenon that can reproduce experimental results but do not have a reference to the physical system. Predictive models can provide new findings, allowing insights into underlying mechanisms, outside the set of experimental conditions used to fit the model. Those latter models rely on anatomical and biophysical definitions of the phenomena under study. In addition, predictive models can be subdivided into detailed, that describe numerous ion channels, and simplified models, that group ionic channels into a minimal set of variables.

In the past decades, there have been built hundreds of predictive biophysical models of cardiac myocytes that can reproduce the bio electrochemical phenomena occurring through cardiac cellular membranes [37]. Models of cardiac cells incorporate formulations of transmembrane ionic currents along with the voltage, ionic concentrations, and ion channel kinetics responsible for the currents. They can capture the time-dependent processes
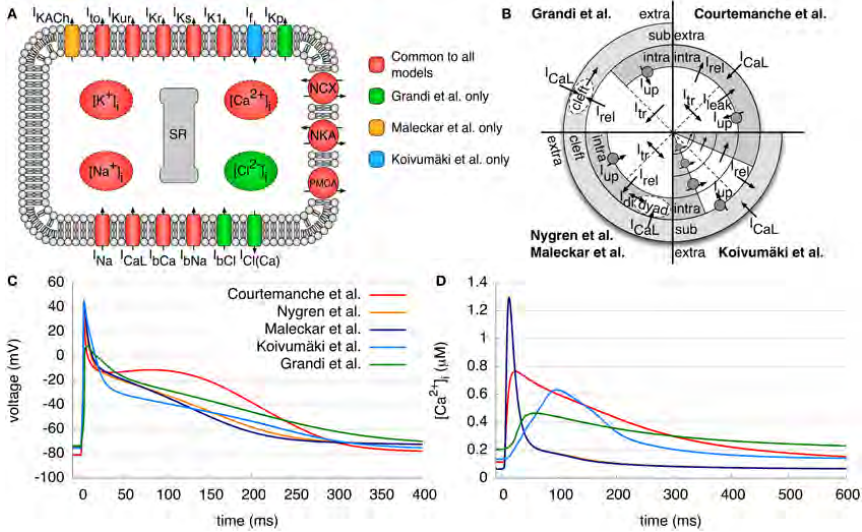
Figure 2.11: Comparison of human atrial ionic models. (A) Schematic of the cell membrane including the different modeled ionic currents and intracellular ion concentrations. (B) Schematic of the calcium handling with different compartments and currents of the models. (C,D) Resulting APs and the corresponding intracellular calcium concentrations after pacing for 50 s with a BCL of 1 s. Figure adapted from [64]

that underlie common electrical pathologies at cellular level. Those models are based on experimental electrophysiology data acquired from invivo and exvivo samples using techniques such as patch-clamp (invented by Erwin Neher and Bert Sakmann in the 1970's), which could be assimilated thanks to mathematical and numerical models of computational electrocardiology, such as the Poisson-Nernst-Planck (PNP) system.

Hence, there are mathematical models to simulate ventricular myocytes, atrial myocytes, specialized conducting tissues such as Purkinje cells or fibroblast. Most of the models have also been adapted to take into account the electrophysiological heterogeneity present in real tissues. Among the most used detailed models to simulate human atrial myocytes we can highlight, the Courtemanche-Ramirez-Nattel (CRN) ionic model [59], the Maleckar et al. ionic model [60], the Nygren et al. ionic model [61], the Koivumaki et al. [62], or the Grandi etl al. ionic model [63] (see Figure 2.11). A comprehensive review of atrial models is presented in [64].

Electrophysiological tissue models

Since cellular models by themselves will not allow performing whole heart studies they have to be integrated into tissue and organ level models. The integrating approach is known as multi-scale modeling, and has to deal with the coupling of different temporal and spatial scales into a single main model.

Therefore, we have subsystems with different levels of detail coupled together by a few interface variables. In cardiac electrophysiology modeling, cell models are coupled together by means of the so-called bidomain model [65, 66], a generalization of the one-dimensional cable theory that takes into account the evolution of the intra- and extracellular potential fields. The bidomain model is a reaction-diffusion set of equations that can incorporate the information from the cellular scale, but not in an individual fashion, since it is a continuous-based model that averages the properties of many cells up to the body surface.

Bi-domain model only receives one parameter from the cellular level, the transmembrane potential that results from a large number of ionic exchanges that are only traced at cellular level. As the bidomain model is very expensive computationally, it is often simplified by assuming that the relationship between intra- and extracellular domains has equal conductivity anisotropy ratios, which allows obtaining a simplified representation called the mono-domain model [67]. This model has been widely used for cardiac simulation because of its reduced computational cost.

Multiscale simulations

The mathematical problem associated with solving the differential equations that govern the propagation of the electrical signal in a three-dimensional heart model is highly nonlinear and has no analytical solution. Therefore, these models must be solved using numerical methods, such as the finite difference method or the finite element method (FEM). A 15 cm^3 block of tissue (approximate volume of a rabbit heart) will have more than 15 million elements. In the heart electrical modeling problem, each of these elements must be associated with a system of about 20-30 differential equations that must be solved with time steps of the order of milliseconds. Thus, the dimensions of the problem for a human heart are enormous. Under these conditions, it is evident that the complexity of cardiac models implies the
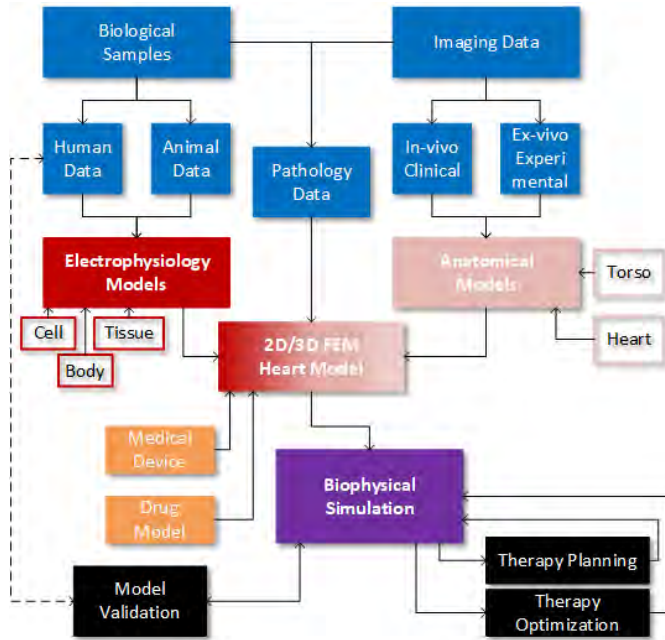
Figure 2.12: Different steps that are required to go from the raw biological data to the patient-specific simulation for diagnosis and therapy planning.

use of high performance computers (HPC, High Performance Computing) or GPU systems (Graphics Processing Unit) and software specifically designed to solve them [68, 69, 70].

2.4 Machine Learning

Artificial Intelligence (AI) is the area of Computer Science dedicated to design machines able to recognize patterns. These machines are based on mathematical models oriented to provide artificial perception to different scientific scenarios, such as, speech recognition, fingerprints identification, DNA sequence identification and others. Within biomedical engineering, the perception of clinical samples is carried out by medical teams which can recognize or classify medical images, ECG signals, and others. However, before any human or machine could recognize any kind of pattern, a previous learning process is required.

Machine Learning (ML) is the area of AI responsible for modeling this learn-

ing processes in an artificial way, that is, designing mathematical models that will be coded as algorithms and finally evaluated in real scenarios. This section aims to briefly introduce the computational context of learning algorithms and specially focusing on the models and techniques used in this thesis.

A learning process starts analyzing the set of patterns under study, that is, the training set (TS). For instance, to properly recognize diseased cells images versus healthy ones. Once a TS, with images of both classes, is available, it is important to know if the training set has been already recognized by medical experts in the field, that is, if the TS has been labeled with the corresponding classes or not. This question is a key-point in ML and it splits the area into the two main approaches followed to design learning algorithms: **supervised** learning (samples classes are known) and **unsupervised** learning (classes are unknown). In this way, each sample (cell image) could have an associated label or class (A=Cancer, B=Healthy) or not. When the class of the samples is unknown, algorithms have to automatically group them by similarity (clustering), and assign the label or class to each cluster. Therefore, the goal of clustering algorithms is to manage the different groups or classes hidden in the TS. On the other hand, when the class of each sample is known, the learning process changes completely, and focuses on explaining why an image has been classified to the corresponding class. In this supervised case, the learning process generally adopts an optimization scenario where the parameters of the model must be calibrated to correctly classify the maximum number of samples of the TS.

There are a few common tasks in both learning scenarios (supervised and unsupervised). The first one is how to represent the training samples, that is, the **feature extraction**. A feature of a pattern is simply a function that helps to define or characterize that pattern in some way. The selection of the most informative features for a specific pattern plays a fundamental role in current ML systems, as normally an expert analysis of the pattern under study is required. At this point, pattern **segmentation** is normally faced in bio-medicine samples and it is the base of many feature vectors used by ML algorithms. In our example, features must capture important morphological information from the cell images provided, logically according to the clinical experts recommendations. Features as, edges extraction, thresholding, curve fitting and many others can be used to represent the cell morphology of a sample. The final selection of features will be computed for all the images, transforming them into a new space, the *feature-space*. In this space,
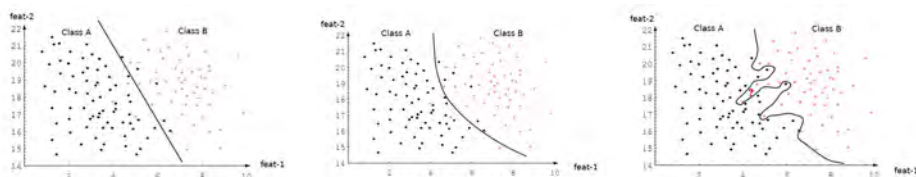
Figure 2.13: 3 different decision boundaries in 2D feature space.

each sample is represented as a feature vector, that can be viewed as a point in a n-dimensional euclidean space, being n the number of features selected. It is remarkable the advances produced by convolutional neural approaches at this point, as these deep neural designs are able to automatically perform this selection and to obtain excellent results in different scenarios. Once the training set has been transformed to the new features space, the main goal of ML models is to learn the **decision boundaries** among the different classes inferred from the training set. Once the classes-boundaries have been obtained, the model can predict the class of new unknown samples (test) according the relative position of the test-samples to them.

To illustrate this, Figure 2.13 shows three different types of boundary decision with two sample classes, represented as 2D feature vectors (e.g., width and height of the cell). Each point represents a sample from the TS, however now we have a mathematical framework to define models able to define the required boundaries. Logically the number of features associated to complex patterns is normally higher, and sometimes it can be problematic. For instance, when handling 2D/3D images where each pixel is managed as a single dimension, a small image (100x100 pixel) is managed as a feature vector with dimension 10000. The dimensionality is an other important topic in ML, and as it is convenient to work with a minimum set of features, the **feature selection** phase is a common task included in ML systems. ML complex systems requires the combination of different phases so pipeline designs are very frequent in biomedical systems.

2.4.1 Feature Selection

This problem consists on selecting a subset of relevant features that will be used to build the learning model. There are different benefits of selecting features properly:

- Smaller models (avoiding high dimensionality)

- Reduced training times

- Reduce overfitting (see figure 2.13 - right)

When dealing with high dimensionality spaces, redundant or irrelevant data is normally handled, and therefore it should be removed without incurring in too much loss of information. There are different techniques able to score the features of a training set to help studies on this selection. First, an exhaustive search of the space is clearly intractable for any complex biomedical problem. The evaluation metric used for the features heavily influences the algorithm design. Traditionally, there are two main categories associated to these methods: wrappers, filters. **Wrapper** methods use ML models to score the features. Firstly, new sets extracted from the training are built to train a model. Secondly, all the models are trained and tested on a hold-out methodology. In traditional regression analysis, the most popular form of feature selection is *stepwise* regression, which includes a greedy algorithm that adds the best feature (or deletes the worst feature) at each round.

Filter methods use different kinds of functions, that can be easily computed on the features set providing useful information associated to them. Generally, these functions aims to evaluate any kind of correlation between the features involved. The evaluation metrics can be based on Information Theory, such as, mutual information functions, pointwise mutual information, or based on statistical tests, such as, Pearson product-moment correlation or univariate feature selection, which works by selecting the best features based on univariate statistical tests (eg. χ^2).These scoring functions are useful to obtain the univariate scores and also the corresponding $p-values$ associated [71].

2.4.2 Unsupervised Models

From an engineering point of view, unsupervised learning let the researches to look for the different groups that the TS contains and to work with the corresponding sets. Probabilistic and nonprobabilistic solutions have been traditionally used to face this problem. The classical **K-means** algorithm [72] is probably the main representative clustering algorithm based on the sum-of-squares criterion. The algorithm tries to identify K-clusters from the TS based on the optimization of the centroids of each class. In this context, the centroid is an imaginary sample ideally situated at the center of mass

of each set of cluster samples. The method used by K-means to move the centroids from their original random locations in the feature space to their final locations is based on an objective function or distortion measure:

$$J = \sum_{n=1}^{N} \sum_{k=1}^{K} \|x_n - \mu_k\|^2$$

This measure represents the sum of squares of the distances of each data point to its assigned centroid μ_k, and logically the goal is to minimize this function. K-means can do this through an iterative process in which each iteration involves two steps, first the data are classified according to the current vector μ of centroids. Second, the centroids are recomputed and moved forward towards their final locations. This procedure stops when the groups contain the same points in two consecutive iterations, or the space displacement is very small. Figure 2.14 illustrates the iterative clustering algorithm presented.

One important issue of K-means is that the number of clusters, K, must be provided as an input parameter. This is interesting when researchers want to validate their hypothesis for a fixed number of clusters. For instance, in our case we use the clustering algorithm with BSPiM torso images and different K values to validate the atrial space partitions obtained for each case.

Hierarchical Clustering is also very interesting when clusters can be further split in subclusters iteratively. The most natural representation of hierarchical clustering is a corresponding *tree*, called dendogram which shows how the samples are grouped. Instead of deciding a priori the number of clusters to obtain, the dendogram offers a global view, and the possibility to define a measure of similarity among clusters. Then, according to this function and a given threshold, different clusters can be obtained. Figure 2.15) shows how the maximum similarity corresponds to $k = 1$, i.e. one cluster per sample. Then when this threshold is relaxed different samples start to clusterize, $k = 2..8$ This representation is also very useful in biological taxonomies for visualizing groups of species, sub-species. In this work, hierarchical clustering represents a very useful tool to analyze the relation among the ectopic locations (on the atria) and their corresponding BSPiM (torso map) through the possible groups provided by the tree.

Bayesian approaches of clustering have been studied during the last decades as they provide a robust mathematical framework to obtain different kind of
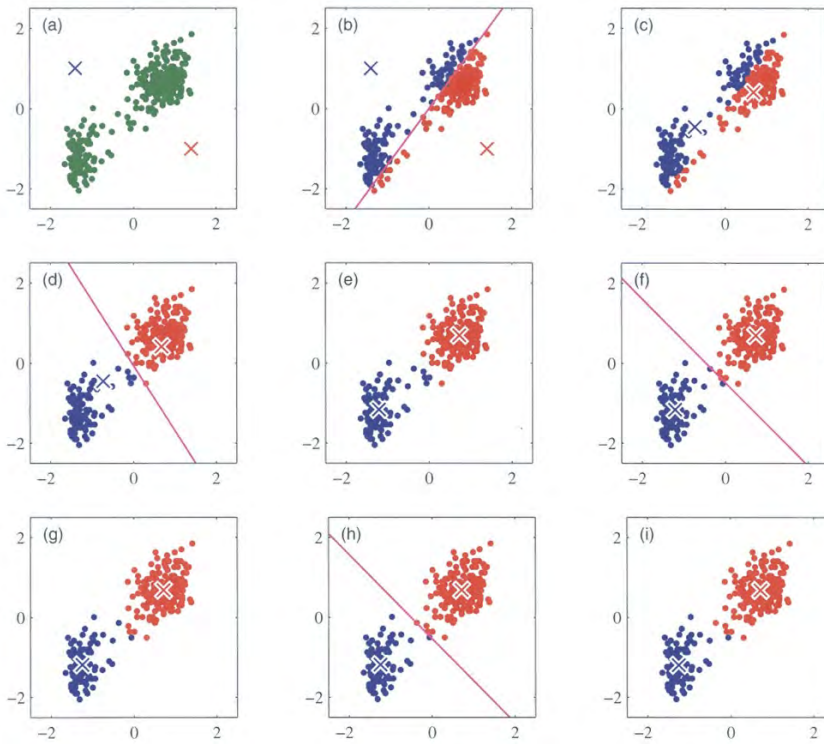
Figure 2.14: Illustration of K-means iterations. The cluster centroids are shown by crosses [73]
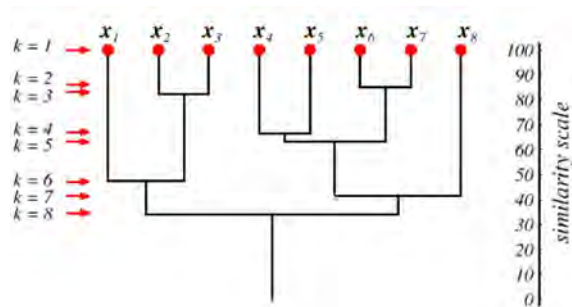
Figure 2.15: A dendogram represents the results of hierarchical clustering algorithms.
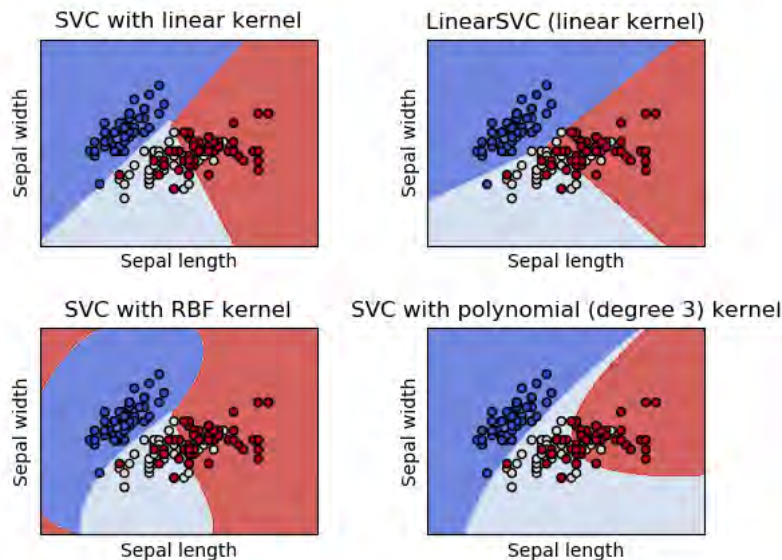
Figure 2.16: Classification boundaries for different SVM-kernels [71].

clusters based on Mixture of Gaussians [73]. A shared problem among ML algorithms is to have enough data to learn the desired decision functions. This is specially important in biomedicine where the data variability of the population must be captured by the model, so a high number of clinical samples is required to let the model learn this variability. However, since the amount and type of clinical samples do not fully represent the population variability, synthetic data can help to fill this gap, providing very accurate simulation models able to complete or replace real population data.

2.4.3 Supervised Models

These models learn from a labeled dataset, where each sample has an associated class. In this scenario, most of the ML models learn the required decision functions by means of an internal parameter optimization process. Generally, when the learning process has converged the model is able to correctly classify (predict the correct class) a high percentage of the samples in the training set. To check its generalization level, a cross-validation is often used.

Recent advances promoted by the application of convolutional neural networks (CNNs) have been recognized by scientific communities such as biology, bio-medicine and behavioral sciences, which have been incorporating ML models into their research problems [74]. However, CNNs require a lot of data samples to optimize their parameters and to learn, and this requirement can be problematic in some domains. When the number of available learning samples (i.e, images) is not very high (thousands) other similar ML methods, such as Support Vector Machines (SVM) offer an adequate alternative.

Support Vector Machines have been very popular in the ML community as they are very effective in high dimensional spaces, even when the number of dimensions is greater than the number of samples. Another important property of SVNs is that the learning process is managed as a convex optimization problem and so any local solution is also a global optimum [73]. This model uses a subset of training points in the decision function (called support vectors) and different kernels (linear, polynomial, radial) can be used for the decision function. Basically the kernels project the classes into a new higher dimensional space (to increase the classes separation) using the support vectors (vector from the two closest points of the classes). For illustrative purposes, Figure 2.16 shows the different decision boundaries obtained for the kernels used in a well-known toy 2D problem [71].

2.4.4 Cross Validation

Cross-validation is a statistical method used to evaluate whether the assumed hypothesis about ML models are acceptable according to the data managed and the results obtained. The evaluation of ML models requires (at least) an error function, however, during the learning process the error function managed only gives us an idea about how well the model does on data used to train it. Therefore, a basic solution involves removing a part of the training data and using it as a validation set, to get predictions from new data (holdout). In **K-Fold cross validation**, the training set is divided into k subsets. Now the holdout method is repeated k times, so that each time, one of the k subsets is used as the validation set and the other k-1 subsets conform the training set. The error estimation is averaged over all k trials to get total effectiveness of our model. The procedure ensures that every data point appears in a validation set exactly once, and k-1 times in a training set. There is not a general accepted K value (mainly depends on the training set size considered and the number of samples per class) but

generally K = 5 or 10 is preferred. The stratified version of this method ensures that each fold contains approximately the same percentage of samples of each target class as the complete set. This is specially important in small training sets as possibly reducing samples from the under-represented classes is not always possible.

ML within its two main approaches, supervised and unsupervised learning, are both mature scientific fields that currently offer a large number of methods and alternatives to clustering and classification problems [71]. Although originally pattern recognition was highly influenced by Bayesian Decision Theory, nowadays, neural networks are taking advantage of the large amount of biological and physiological data acquired with medical technologies, such as medical images, electroencephalography or genomics sequences. On the other hand, in order to properly exploit the new convolutional models, a large amount of clinical samples must be provided.

2.4.5 Application of ML to Electrophysiology

Machine learning has become particularly relevant in well-known cardiology problems such as the analysis and classification of ECGs, the characterization and recognition of (A/V)F and also the location of abnormal activation that produces tachycardia in both atria and ventricle. There is a substantial body of literature focused on ECG's classification. A very good review of some of the earlier work is given by [75]. The PhysioNet challenge to classify single-lead ECG segments into four categories (sinus rhythm, AF, other rhythm or too noisy) shows the state of the art around this problem [76]. Most of the approaches proposed require preprocessing signal, including denoising and correcting for baseline wander. Then, different ML algorithms are ready to be used. At this point, although convolutional neural networks [77, 78] and recurrent neural networks [79] are gaining popularity, many studies still achieved accurate classification results using other algorithms such as ensembles of decision trees (random forests) [80], multi-level binary classifiers [81] and least-squares support vector machine classifiers [82]. Furthermore, online real-time feature extraction and classification of ECGs using machine learning is being explored [83].

The combination of clinical data, such as medical images from MR, within simulated data (EGM, ECG) oriented to generate the training set for ML algorithms conforms a pipeline scheme that can be shown in recent approaches to predict the ablation target [84]. For instance, in [84] the authors propose

a feature augmentation scheme that aims to improve the performance of a learning algorithm for the detection of cardiac radio-frequency ablation (RFA) targets (managed as patches in the ventricle), with respect to learning from images. First, the authors extract image features from delayed-enhanced MRI (DE-MRI) to describe local tissue heterogeneities and feed them into a machine learning framework for the identification of potential ablation targets. Second, they introduce a patient-specific image-based model derived from DE-MRI coupled with the Mitchell-Schaeffer electrophysiology model for the simulation of intracardiac electrograms. This feature augmentation scheme increases the classifier's performance up to 97.2% accuracy, 82.4% sensitivity and 95.0% positive predictive value (PPV) improving the original classification results.

Analysis of fibroblast-myocyte coupling in a 3D model

Abstract – Atrial arrhythmias have been linked to the existence of fibrosis. The distribution of fibrosis may determine the location of electrical drivers, and alter the normal sequence of activation in the atria. Due to the effects of myocyte-fibroblast coupling, such as modified myocyte resting potential, and partial inactivation of sodium current, conduction velocity of electrical wave propagation can be greatly decreased in areas near fibrosis. In this chapter, we study the effects of coupling the Courtemanche-Ramirez-Nattel (CRN) ionic model to the MacCannell fibroblast cell model in a simplified 3D geometrical model, considering different version of the CRN as a function of the atrial region.

3.1 Introduction

Initiation and maintenance of atria arrhythmias, specially AF, as well as success of RFA are strongly related to atrial fibrosis [25]. From a mechanistic point of view, the existence of areas with structural and functional heterogeneity in the atria, due to the proximity to fibrosis, promote the arrhythmogenesis [85, 86]. Such regions usually slow down or even block the propagation of electrical waves, which creates the conditions required to sustain rotors. It is important to note that those regions, although damaged, do not inhibit completely the propagation of electrical waves as happens in dense scarred areas, but show complex high-frequency electrical activity [87].

Computational models can help to analyze the detailed interactions between fibroblast and atrial myocytes, to better understand the mechanisms that initiate arrhythmia, or the coupling effect myocyte-fibroblast [88]. Those studies would be impossible in real clinical or experimental settings, where most parameters are unknown or cannot be altered. In that line, in [26], multi-scale biophysical models were used to elucidate the mechanistic link between patient-specific fibrosis distribution and AF drivers, concluding that rotors stabilize in the border zones of patchy fibrosis in 3D atrial models, where slow conduction enable the development of circuits within relatively small regions. In that study, patient-specific fibrotic regions were reconstructed from LGE-MRI images, healthy tissue was modelled using the CRN ionic model, and fibrotic tissue by the MacCannell fibroblast model.

In [89], several methodologies to capture fibrillation dynamics by computational models were studied, concluding that the representation of fibrosis has indeed a large effect on rotor dynamics. Among the most common ways to model fibrosis within the LA there are those who opted for including structural changes affecting tissue properties such as interstitial conduction barriers [90], probabilistic percolation [91], or modified conductivities [92], and those who include electrical changes at cellular level such as incorporation of fibroblast [93, 94, 95], or modification of ion channels [96], or both [97]. In addition, some recent works also studied in 0D and 2D the different effects of myocyte-fibroblast coupling in different regions of the atria considering the cellular heterogeneity [97, 88].

In this chapter, in order to analyze the coupling of the different heterogeneous cell models with fibrosis, we performed an analysis on a 3D slab of tissue that combined healthy atrial tissue from different regions and fibrotic
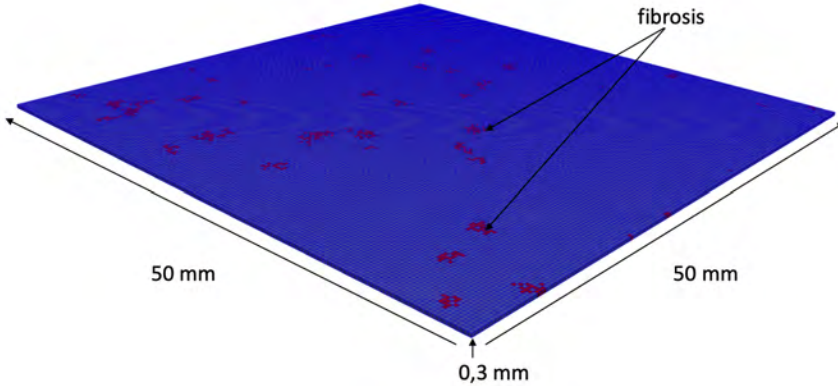
Figure 3.1: 3D model of a slab of tissue model including fibrosis (red elements).

tissue to assess: (i) changes in action potential duration (APD), (ii) conduction velocities and (iii) depolarization patterns. We analyzed results for both diffuse fibrosis and patchy fibrosis. For the last different densities of fibrosis, following the Utah levels were used.

3.2   Methods

3.2.1   Anatomical Modeling

To study the effects of fibrosis in isolation, all simulations were performed using the same mesh geometry and fiber field. The 3D slab dimensions were $50 \times 50 \times 0.3$ mm and were built with voxel elements of 300μm in size (see Figure 3.1). Fiber orientation was assigned parallel to the x-y plane to easy the interpretation of results.

Fibrosis was also added to the slab model in two different ways. First, diffuse fibrosis was included by randomly selecting elements from the slab and assigning the fibroblast cell to its nodes (see Figure 3.2, top row). Second, patchy fibrosis was included by randomly selecting seeds (mesh elements) to spread the fibrotic patches, and following performing a region growing (see Figure 3.2, row below). However, to avoid unrealistic perfect spherical fibrotic regions, we randomly reassign patchy elements back to healthy atrial tissue in the contours of the growing patch in each iteration, forming random fibrotic tissue shapes that might include surviving healthy

tissue surrounded by fibrosis. The fibrotic area sizes were grown according
to the Utah classification [98, 99], that defines up to four levels of LA
remodeling (quartiles) of fibrosis associated to the ratio of fibrosis to atrial
volume [Utah stage I: $< 8.1\%$ (Q1); Utah Stage II: $< 16\%$ (Q2); Utah
Stage III: $< 21\%$ (Q3) ; Utah Stage IV: $> 21\%$ (Q4)]. Therefore, from the
initial random distribution of seeds, fibrosis was grown, as described above,
generating a total of 5 3D models. Note that we developed two models for
quartile Q4 that we called Stage IV and Stage V.

In the slab model, we also evaluated two conditions: i) the amount of tissue
required to obtain a conduction block, and ii) the minimum width of a con-
duction channel (i.e., longitudinal disposition of halthy tissue, surrounded
by dense fibrosis) required to allow that the electrical wavefront crosses it.
For the first configuration, cross-wise lines of fibroblast cells with different
widths (x-axis) were included (from 0.3mm to 1.8mm). For the second, all
tissue was modeled as fibroblast, except a conduction channel modeled as
healthy atrial tissue, with different width [1.4, 1.5, 1.8, 2.4, and 2.7 mm]
(x-axis) $\times$ [0.3 mm] (z-axis).

3.2.2 Electrophysiological Modeling

For the electrophysiology simulations, we made use of the Courtemanche-
Ramirez-Nattel (CRN) ionic model [59], plus the well-established fibroblast
cell model by [93] coupled to the CRN model as in [26]. We considered
cellular tissue heterogeneity in the atria as in [97], and hence we carried out
experiments for two different atrial regions, namely LA, and PV. To model
both regions we adjusted several currents at cellular level I_{to}, I_{CaL}, and
I_{Kr}, as well as conductivities and conductivity ratios, as in [100]. Table
3.1 summarized the changes. The first three rows are the multiplicative
factors used for the maximum conductance of three (g_{to}, g_{CaL}, and g_{Kr}) ion
channels with respect to the base CRN ionic model, and the next three rows
are the longitudinal conductivity (σ_l), the ratio between the transverse and
longitudinal conductivities (σ_t/σ_l), and the longitudinal conduction velocity
(CV_L).

The computation of the electrical propagation in the atria was calculated
solving the reaction-diffusion, mono-domain equations, Eqs. 3.1 and 3.2,
given by [101] with the finite element method using the operator splitting

Table 3.1: Parameters used to reproduce cellular and tissue atrial heterogeneity.

Prop.	LA	PV
g_{to}	1.00	1.00
g_{CaL}	1.00	1.00
g_{Kr}	1.60	2.20
σ_l	0.003	0.0017
σ_t/σ_l	0.35	0.5
CV_L	63.3	75.0
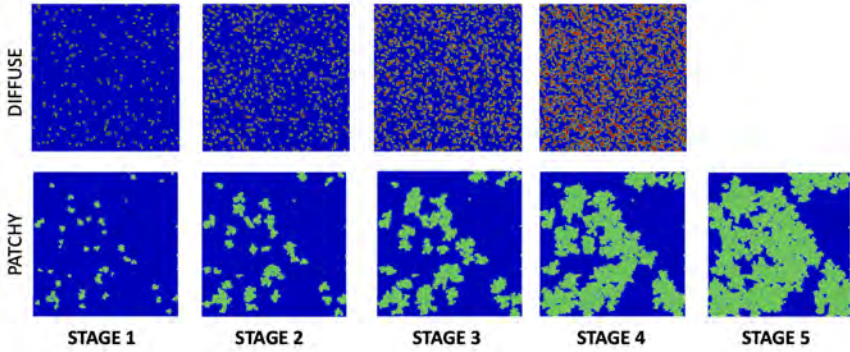
Figure 3.2: 3D slab of tissue including diffuse and patchy fibrosis (red and green regions, respectively).

numerical scheme by ELVIRA software [69],

$$\nabla \cdot \big(\mathbf{D}\nabla V\big) = C_m \cdot \frac{\partial V}{\partial t} + I_{ion} \quad in \quad \Omega_H \tag{3.1}$$

$$\mathbf{n} \cdot \big(\mathbf{D}\nabla V\big) = 0 \quad in \quad \partial\Omega_H \tag{3.2}$$

where $\mathbf{D}$ is the equivalent conductivity tensor, I_{ion} is the transmembrane ionic current that depends on the cellular model, C_m is the membrane capacitance and Ω_H is the heart domain.

Note that due to the large gradients in resting membrane potential (RMP) at t=0ms between the fibroblast model and the myocyte healthy cell model, the full 3D system requires a full electric stabilization. Otherwise, the tissue triggers random electrical depolarizations in areas were dense fibrosis is included. Therefore, we paced the model for 10 heart cycles at a frequency

of 2Hz (BCL=500ms) before starting the experiments. Simulations were carried out by stimulating with a square signal of 140 pA/pF amplitude of 2 ms duration. Stimuli were apply either to a complete face of the slab (considering propagation along and across the fibers) or from a box-shaped region in the middle of the 3D slab. Spatial discretization was 0.3 mm and temporal discretization was set to 0.02 ms.

3.2.3 Analysis of Cell Coupling

Several configurations of the fibrotic tissue were designed to evaluate: (i) the minimum amount of fibrosis required to produce a conduction block in a wavefront advancing perpendicular to the line of fibrosis; (ii) the minimum conduction channel (healthy tissue surrounded by fibroblast) necessary to allow the propagation of the electrical impulse.

3.3 Results

3.3.1 Diffuse Fibrosis

In the slab of tissue including diffuse fibrosis (see Figure 3.2 top row), after stabilizing it during ten heat cycles, we performed a simulation by stimulating with a transmural squared stimuli at the center of the geometrical model. Figure 3.3 shows the wave front propagation at six different time steps color-coded with the amplitude of the voltage membrane (Vn). At t=1ms, it can be observed the area that has already depolarized due to the stimulus (red regions). It is noteworthy that the healthy atrial tissue (correspond to the CRN model [59], PV region) show very different RMP as a function of the fibrosis STAGE. At stage 1, most of the tissue shows a RMP around -81 mV (blueish areas), while at stage 4 where there is a large amount of fibrosis coupled to tissue, the RMP is around -66 mV (greenish areas). As time progresses, the wavefront propagates much faster in the model on stage 1, and the wavefront shows a smooth spread, whereas in stage 4, it is distinguishable a rough advance of the wavefront which is much slower. Note that at t=50ms in stage 4, the center of the model starts to repolarize earlier than other models, and at t=150ms it is clear that the amount of fibrosis is correlated with the time where repolarization starts (shortening of the AP plateau). This larger different in depolarization time
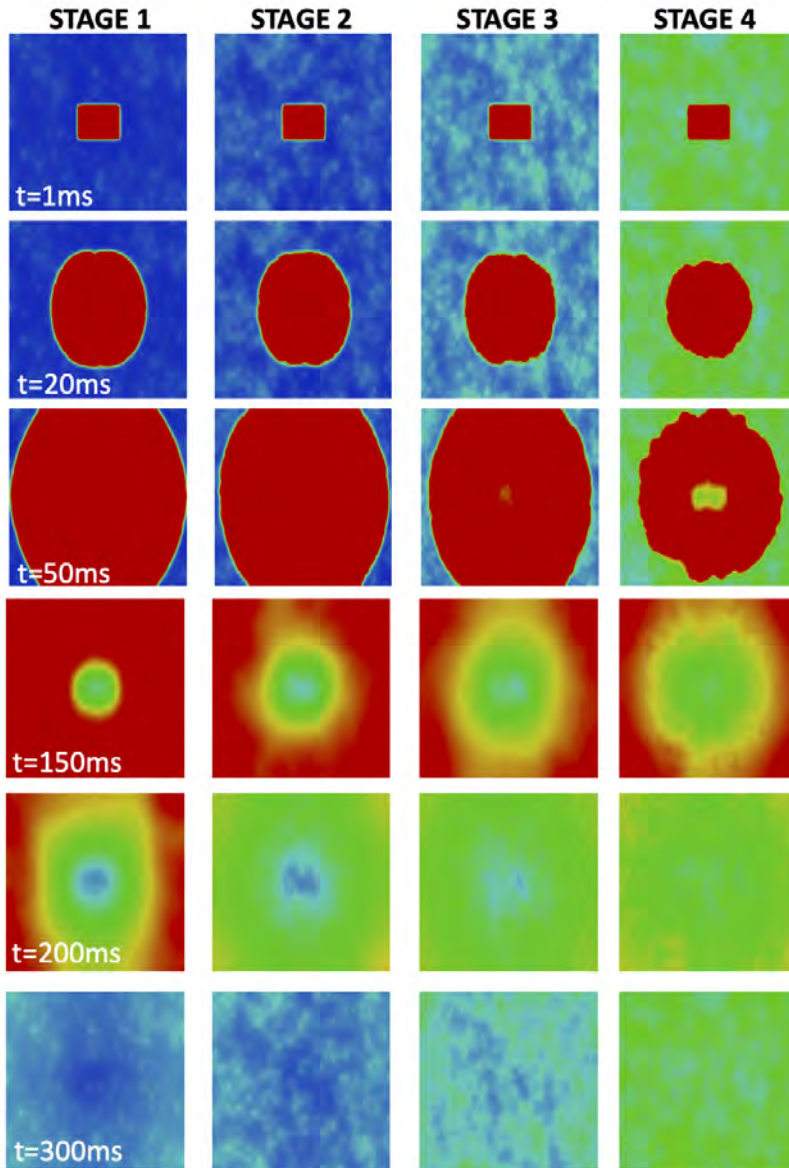
Figure 3.3: Depolarization sequence at six different time instances on a model with different stages of diffuse fibrosis. Healthy tissue ionic model corresponds to the PV region. Slabs are color-coded with the value of the transmembrane voltage (Vm), where bluish colors correspond to low voltages (-81 mV), while reddish colors correspond to large values (-20 mV).
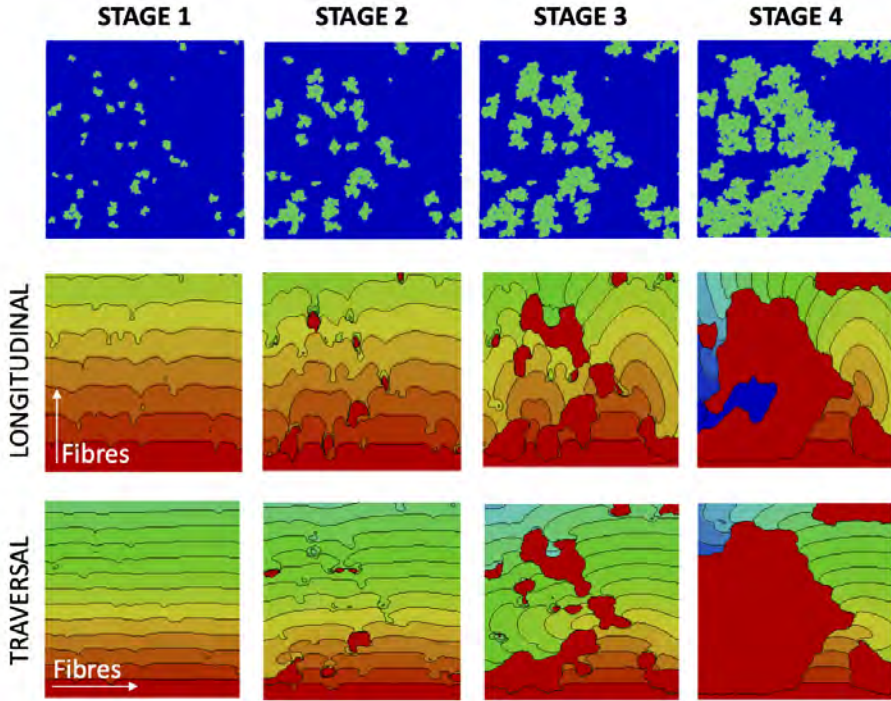
Figure 3.4: Local activation map along and across fibres on a model with different stages of patchy fibrosis corresponding to the PV region. Stimulation is triggered from the hexahedral external element faces below. Green areas in the top row correspond to the fibrotic patches. Color-coded with the LAT from red (earliest activated regions) to blue (latest activated regions). Note that none activated (fibrotic) areas are also depicted in red.

as a function of the density of fibrosis create on the tissue large depolarization heterogeneity gradients that can favor the initiation and maintenance of arrhythmias. Stage 5 of fibrosis (not shown), did not allow to trigger a depolarization. In all cases the maximum amplitude of the AP was very much reduced.

3.3.2 Patchy Fibrosis

In the slab model including patchy fibrosis we performed different studies. First, we analyzed the effect on the depolarization wavefront for different regions of the atria (PV and LA) and different stages of fibrosis. As can be observed in Figures 3.4 and 3.5 the LAT maps show disruptions on
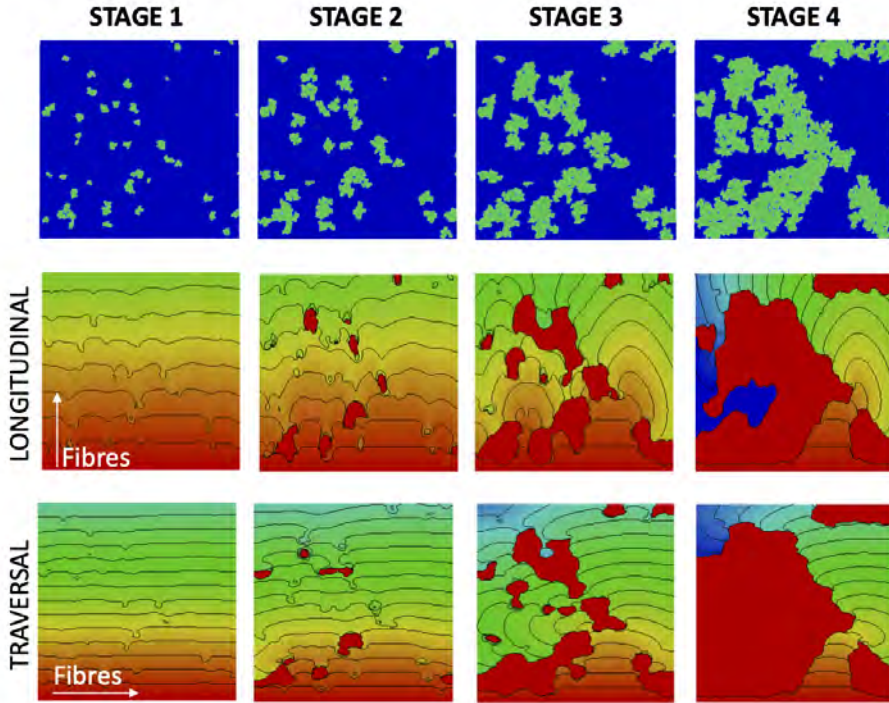
Figure 3.5: Local activation map along and across fibers on a model with different stages of patchy fibrosis corresponding to the LA region. Stimulation is triggered from the face below. Green areas in the top row correspond to the fibrotic patches. Color-coded with the LAT from red (earliest activated regions) to blue (latest activated regions). Note that none activated areas are also depicted in red.

the wavefront propagation due to the interaction with fibrotic patches (top row shows the location of the fibrotic patches in green color). In stage 1, where the patches have a reduced area, the depolarization wavefront can go through most of them thanks to the electrotonic currents generated due to the myocyte-fibroblast coupling. Therefore, there is simply a delay on the wavefront propagation observable on the isochrones, but the tissue appears to be activated (over a threshold).

It is remarkable that the isochrone maps are different for the case of PV (Figure 3.4), and LA (Figure 3.5), which is not due the AP model itself but to the different tissue conductivities employed in this two atrial regions. The same differences can be also observed for both cases when we stimulate generating a wavefront along the fibers (middle rows) or across the fibers (row below). It can be appreciated a difference in conduction velocity where

faster tissue shows wider isochrones and depolarizes the 3D slab faster, but also differences in the wavefront propagation, being more sensible those with higher conductivity. When we move to larger sizes of fibrotic patches (stages 2 to 4)) small islands of non-depolarized tissue start to appear (red regions), since due to the fibrotic mass they behave as anatomical barriers that the wavefront surrounds. In the most extreme case (stage 4), several interactions can be observed. Due to the continuous coupling of fibrotic tissue to healthy atrial cells in large patches, the isochrones nearby the patches start suffering a reduction in propagation velocity due to the decrease in current availability. This effect can be observed in the LAT maps, where isochrones around the fibrotic region curve more markedly. In addition, also due to the patch sizes, the depolarization wave cannot cross through many of the small and tortuous channels created by the healthy atrial tissue, generating blocks. The existence of a block depends on the geometry of the patch, and the conductivity of the tissue interacting with the fibroblast, which explain the differences in the maps for Figures 3.4 and 3.5.

Finally, we analyzed in more detail the coupling effects between the atrial healthy tissue and the fibroblast. In particular, we assessed the influence of the electrotonic interactions between atrial tissue myocytes and random shape and size fibrotic patches on the AP, APD, and the RMP; with that purpose, we used six probes located in different positions within the 3D slab of tissue with Stage IV of fibrosis. Figure 3.6 (B) shows the AP morphology measured at different locations (see Figure 3.6 (A) color-coded probes) in one of the simulations with patchy fibrosis stage 4. Those locations were selected to go across different areas of the slab, from a region free of fibrosis to an area well inside a higher density zone of fibrosis, see Figure 3.6A, labeled Stage IV. To appreciate the changes in the AP when coupling myocytes to fibroblasts, and the cell-to-cell electrotonic interaction, we overlapped the AP signals measured at each probe, together with an AP measured in a healthy myocyte, as control. Figure 3.6B together with Table 3.2 show those effects.

The first effect is that the closer to a fibrotic area the smaller the AP plateau, as can be observed if we compare probes color-coded in dark red, green and blue. Blue probe is already in contact with a fibrotic patch, and shows a reduction of the maximum AP amplitude as well. As we move into the fibrotic patch, we can still observe an AP morphology (purple and black probes), however there is a reduction in the AP upstroke, which will decrease conduction velocity. In addition, the RMP is elevated as we get closer or inside the fibrotic patch. Finally, when we measure deeper in the

Figure 3.6: Electrophysiological effects on the Courtemanche-Ramirez-Nattel myocytes when coupling to the active formulation of MacCannell fibroblast model.
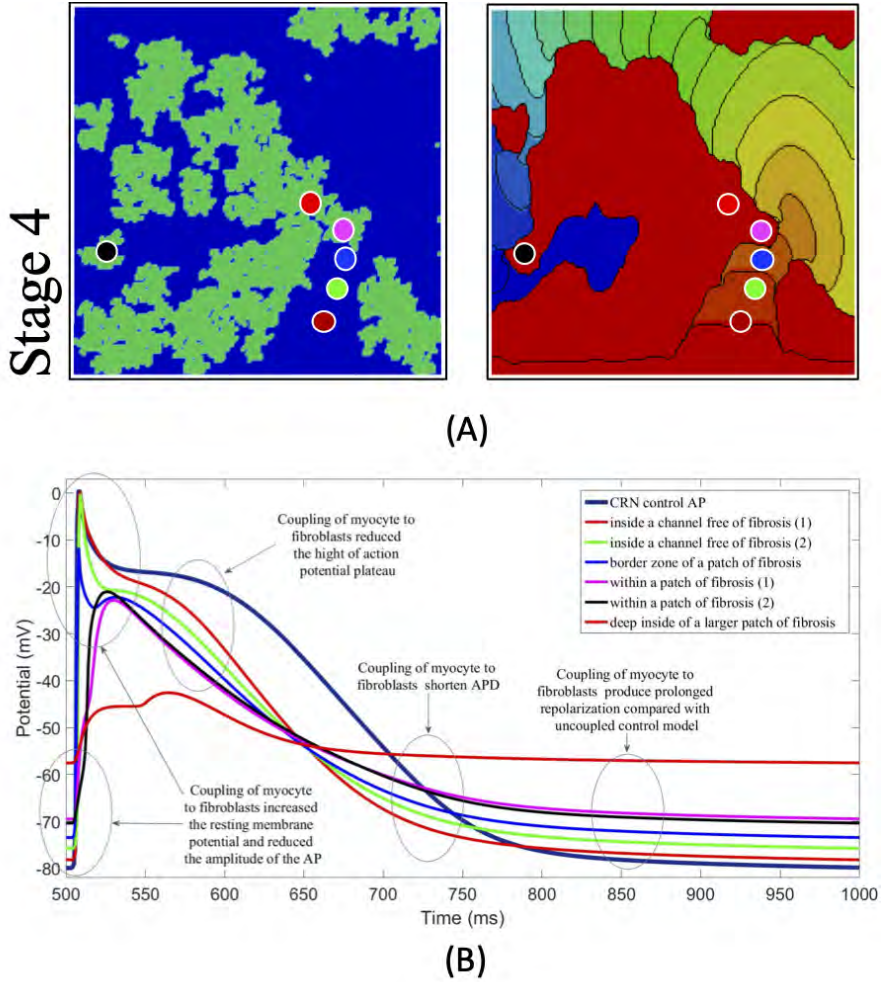
fibrotic patch, only electrotonic currents are observed (red plot), with very small amplitude. Table 3.2 summarizes the changes in RMP, peak value, amplitude and APD90 at the different stages.

3.3.3 Fibrotic Barriers and Conduction Channels

From the analysis of previous section, we concluded that fibrosis can produce important delays in wave propagation and even conduction blocks.

Therefore, we performed several simulations in 3D slab models including fibrotic barriers and conduction channels of healthy tissue surrounded by dense fibroblast regions.

In a first evaluation, we analyzed the amount of fibrosis required to produce a conduction block. We included in the slab modeled as LA posterior wall tissue, a cross-wise line of fibroblast cells with different width (x-axis) to evaluate the effect on the propagation (see Figures 3.7A–D). We stimulated the slab with a cross-wise flat impulse that progressed activating the full width of the slab from bottom to top. Figure 3.7A shows a slab configuration free of fibrosis. The time required for the wavefront to travel the full size of the slab was 59 ms. Figure 3.7B, shows a slab that includes a cross-wise line of 0.3 mm modeled as fibroblast cells. The activation time was 62 ms, therefore the fibroblasts introduced a delay in the propagation wavefront of 3 ms (5% increase). When the fibrotic barrier was 0.6mm, the wavefront took 71ms to reach the top of the slab, that is a 12 ms delay (20% increase) with respect to the healthy configuration (see Figure 3.7C). When the barrier was increased to three voxels, i.e., 0.9 mm width, there was a conduction blockage (see Figure 3.7D). The results clearly show that the effect of fibrosis on the propagation wavefront in our model is not linear.

In a second evaluation, we inverted the configuration of the tissue types of the slab, that is, all tissue was modeled as fibroblast, except a conduction channel modeled as healthy atrial tissue, with different width [1.4, 1.5, 1.8, 2.4, and 2.7 mm] (x-axis) × [0.3 mm] (z-axis). The goal was to determine the minimum width required for a conducting channel to propagate the electrical impulse when it is surrounded by fibrotic tissue. Figure 3.7E shows a slab of fibrosis tissue with a conduction channel of 1.8 × 0.3 mm, where we studied the AP at 4 locations distributed along the conduction channel. Table 3.3 summarizes the results obtained. Location 1 (trace in red color) shows the largest AP amplitude, since it is closer to the initial electrical shock delivered. Resting potential is elevated in all cases, but the effect is larger at locations 2, 3, and 4. Table 3.3 shows the AP values for locations 1 and 4, and for each channel width tested.

The channel with a width of 1.2 mm produced a propagation block a few millimeters from the initial impulse. The intermediate channel width (1.5 mm), propagated the signal, but the amplitude of the signal at the channel exit (location 4) was reduced by 54%, whereas in the wider channel (1.8 mm) it was reduced by 48%. All the APD90 measured, for all locations in the conduction channel, were greatly reduced with respect to the APD

for the original model. With respect to the delay, it was clear that the electrotonic coupling affected the AP rising time, with an increase of 40ms in the propagation delay when channels were reduced to 1.5 mm. That delay equates to a decrease in conduction velocity from 0.85 to 0.50 m/s, due only to the effect of fibrosis coupling. Channels larger than 3.0 mm permitted a normal propagation of the signal in the center of the channel, with respect to conduction velocity and APD morphology.
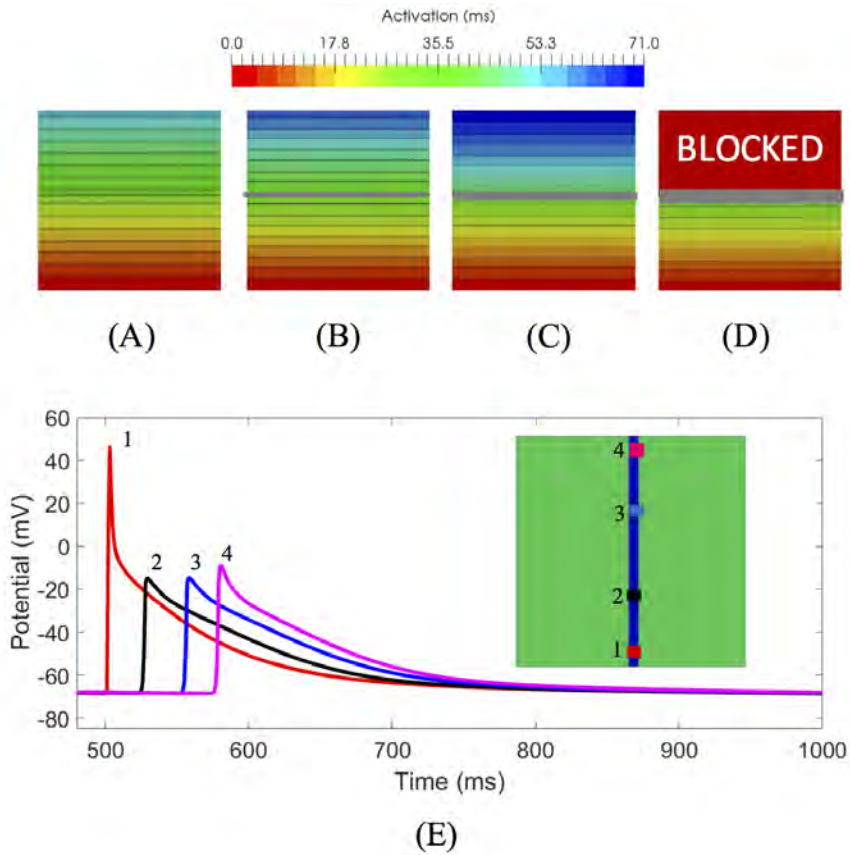
Figure 3.7: 3D slabs of left atrial tissue including fibrosis barriers. (A) Shows a slab free of fibrosis with an activation time of $59ms$; (B) a slab with the same properties and a cross-wise line of one voxel element of fibroblast cell model, taking a time for activation of $62ms$; (C) 3D slab but a line with two voxel elements width, the total activation time was $71ms$; (D) 3D slab including a line of three voxel elements width of fibrosis tissue model where the propagation front is blocked; (E) Study of the effect on the AP at 4 locations along a conduction channel of healthy atrial tissue with a thickness of $1.8mm$ and $[0.3mm]$ height, on a slab of fibrosis tissue.

Table 3.2: Effects of fibroblast-myocyte interaction on the Action Potential (Shown for the Stage 4 of fibrosis)

AP Measurement / Trace	Control	Red	Green	Blue	Magenta	Black	Red (2)
RMP (mV)	-79,9	-78,2	-75.7	-73.4	-69.4	-70.3	-57.5
Peak value (mV)	0.73	0.39	-0.16	-11.67	-22.85	-21.04	-42.58
Amplitude (mV)	80.66	78.59	75.60	61.77	46.63	49.33	14.97
APD90 (ms)	252	209	212	224	219	218	200
APD50 (ms)	153	105	94	101	85	87	52

Table 3.3: Properties of AP in the entrance and exit (locations (1)/(4)) of a conduction channel

Channel Width	1.2mm	1.5mm	1.8mm	2.4mm	2.7mm	> 3.0mm
RMP (mV)	-63.6 / -	-66.3 / -65.8	-68.5 / -68.0	-71.4 / -71.0	-72.7 / -72.2	-79.91
Peak value (mV)	39.4 / -	43.0 / -15.2	46.7 / -9.0	50.7 / -1.7	52.9 / 0.2	0.73
APD90 (ms)	65.0 / -	104 / 122	127 / 168	153 / 189	161 / 195	252
Delay (4)-(1) (ms)	-	99.0	76.0	60.0	60.0	59.0

3.4   Discussion

There is compelling evidence that fibroblasts and cardiomyocytes cell types can directly couple to each other via connexin-based gap junctions [102]. In fact, electrical coupling between fibroblasts/myofibroblasts and ventricular cardiomyocytes [103, 104] and atrial cardiomyocytes [105, 106] has been demonstrated, as well as its effect on cardiac electrical conduction.

Our study shows electrophysiological effects on the Courtemanche-Ramirez-Nattel myocytes when coupling to the active formulation of MacCannell fibroblast model due to the cell-to-cell electrotonic interaction, caused a reduction of AP amplitude which can be appreciated with respect to the control trace as soon as the probe was near a more dense patchy fibrosis area. It produced a reduction of AP plateau, and a clear shortening of the myocyte APD90 with respect to the control AP and variable depending the location of the probe and the density of fibrosis. APD50 showed a more constant reduction of the APD as we went deep inside fibrotic areas showing a clear deformation of the AP profile. Also, it produced a prolonged repolarization of the AP compared to the uncoupled myocyte, and more significantly, fibroblasts had a higher resting membrane potential (RMP) and hence affected directly the myocyte RMP, which was constantly elevated (see Figure 3.6B). Since the resting potential in fibroblasts is less negative than in cardiomyocytes, heterocellular coupling influences the membrane potentials of the two cell types in opposite directions, i. e., the membrane potential of the fibroblast becomes more negative whereas that of the cardiomyocyte is slightly less negative.

Several modeling studies have illustrated the impact of fibrosis on atrial electrophysiology and conduction as well as on ECGs and showed in a realistic atrial anatomy that increased anisotropy in the atria due to fibrosis can be responsible for the breakup of PV ectopic waves into multiple re-entrant circuits. Maleckar et al. [60] coupled a human atrial myocyte to a variable number of fibroblasts and investigated the effect of altering the intercellular coupling conductance, electrophysiological fibroblast properties, and stimulation rate on the atrial AP. The results demonstrated that the myocyte resting potential and AP waveform are modulated strongly by the properties and number of coupled fibroblasts, the degree of coupling, and the pacing frequency.

Jacquemet et al. developed a 2D model of atrial tissue including microfibrosis incorporated as a set of thin collagenous septa (sheets) of cardiac muscle

to determine whether they, like thick collagenous septa, could affect electrical impulse propagation and disconnect transverse coupling [107]. The density and length of these septa were varied and the analysis of unipolar electrograms showed that the septa decreased conduction velocity (CV) by up to 75%. Another important aspect to be considered is the existence of collagen layers in the fibrosis model. Atrial models incorporating transverse collagen deposition have underlined the significant interruption and disorder in atrial conduction patterns [108].

Not only the total amount of collagen was important, but also the specific spatial distribution of collagen deposition, which governed the occurrences of conduction block. Another novel arrhythmic mechanism being considered in models is percolation (slow and difficult fluid flow through a porous medium). It has been shown that simulation of conduction obstacles derived from LGE-MR images of AF patient atria, give rise to excitation patterns resembling near-threshold percolation [91]. In this context, the percolation threshold is the fraction of lattice points that must be filled to create a continuous path of nearest neighbors from one side to another.

In our study, we evaluated the degree to which coupling fibroblasts to atrial myocytes altered the electrophysiology of the normal myocytes. Our simulations confirmed that the coupling of fibroblasts to myocytes significantly affects the electrophysiological properties of the myocytes, as described by [93, 60]. In [26], they observed that the rotors propagate slowly around the border zones of patchy fibrosis (levels 3–4),failing to spread into inner areas of dense fibrosis, which matched our observation in the slab model for patchy fibrosis.

The coupling of the CRN [59] atrial myocyte model to the active formulation of the MacCannell fibroblast model (i.e., 4 membrane currents including, the time and voltage dependent fibroblast current I_{Kv}, the inward rectifying current I_{K1}, the Na^+-K^+ pump current I_{NaK}, and the background Na^+ current Ib,Na) [93], and the cell-to-cell electrotonic interaction, caused: (i) a reduction of myocyte APD; (ii) a prolonged repolarization of the AP compared to the uncoupled myocyte control model AP; and importantly since fibroblasts have a higher resting membrane potential (RMP), (iii) changes of the myocyte RMP, see Figure 3.6B. Furthermore, this shortening of the APD generates a spatial heterogeneity within the atrial tissue due to variations in the fibroblast density and the number of coupled fibroblasts to myocytes, generating a variation of the APD that depends, to a great extent, on the point where the measurement is taken in our virtual human

atrial mesh. Although there were variations in the APD90, dependent on the test location, density of fibrosis, and the number of coupled fibroblast to that point, all the APDs were shorter than the uncoupled myocyte control case, see Figure 3.6B.

Finally, we studied the disruptive effects that fibrotic barriers might cause in wavefront propagation for several configurations. An action potential in a cardiomyocyte in contact to a fibroblast will induce an electrotonically mediated potential change in the fibroblast, and may cause sufficient depolarization to the next cardiomyocyte in the tissue to reach the threshold potential, leading to passive propagation of an action potential through a non-excitable cell, although with some delay [109]. However, if more than one fibroblast is interposed between the cardiomyocytes, the depolarization of the distant cardiomyocyte may not be sufficiently large to reach threshold and impulse propagation will fail. In cell culture experiments with neonatal rat cells, conduction fails if the bridging distance is larger than $300 \mu m$ [103]. Our simulation study, with the particular conduction velocities and cell regions considered, showed that electrotonic currents can excite atrial myocytes crossing fibrotic barriers much thicker, in the order of one millimeter.

3.5 Conclusions

We have carried out a simulation study based on the CRN ionic model coupled to the fibroblast MacCannell model. We considered tissue from the LA and PV regions, and analyzed the fibroblast-myocyte coupling effect, and the impact of fibrotic barriers and conduction channels on the wavefront propagation. In summary, myocyte-fibroblast electrotonic interaction caused: (i) a shortening of myocyte APD; (ii) a prolonged repolarization of the AP compared to the uncoupled myocyte in control; (iii) changes (increase) of the myocyte RMP. Fibrotic barriers of 0.9mm produced conduction blocks in the wavefront propagation. On the other hand, conduction channels under 1.2mm in width did not let the wavefront to cross them. The specific configuration of fibrosis has important effects in the sequence of activation, and should be carefully considered.

Modeling FAT on a 3D atrial model including fibrotic substrate

Abstract – Focal atrial tachycardia is commonly treated by radio frequency ablation with an acceptable long-term success. Although the location of ectopic foci tends to appear in specific hot-spots, they can be located virtually in any atrial region. Multi-electrode surface ECG systems allow acquiring dense body surface potential maps (BSPM) for non-invasive therapy planning of cardiac arrhythmia. However, the activation of the atria could be affected by fibrosis and therefore biomarkers based on BSPM need to take these effects into account. We aim to analyze the effect of fibrosis on a BSPM derived index, and its potential application to predict the location of ectopic foci in the atria. We have developed a 3D atrial model that includes 5 distributions of patchy fibrosis in the left atrium at 5 different stages. Each stage corresponds to a different amount of fibrosis that ranges from 2 to 40%. The 25 resulting 3D models were used for simulation of focal atrial tachycardia, triggered from 19 different locations described in clinical studies. BSPM were obtained for all simulations, and the body surface potential integral maps (BSPiM) were calculated to describe atrial activations. Activation maps for stages with more than 15% of fibrosis were greatly affected, producing conduction blocks and delays in propagation. From stage 3 (15% fibrosis) the BSPiMs showed differences for ectopic beats placed around the area of the pulmonary veins and the coronary sinus.

4.1 Introduction

Focal atrial tachycardia (FAT) is a supraventricular tachycardia that triggers fast atrial rhythms from a location outside the sinoatrial node [30]. FAT is commonly treated by RFA with a long-term success rate. The catheter ablation treatment targets the arrhythmogenic electrical drivers and terminates them by localized energy delivery. The end point of catheter based ablation is to eliminate the triggers with the least amount of ablation necessary [110]. In the case of FAT, the localization of those drivers tends to appear in specific hot-spots [111], for example the PV ostia are the most common sites of origin of focal tachycardias within the LA [112], however they can be found virtually in any region of the atria, which makes sometimes their treatment difficult. The prevalence and distribution of focal triggers in persistent and long-standing atrial fibrillation has also been studied, showing a higher prevalence in the PVs for most groups, although non-PV triggers were observed in 11% of the cases [113]. EAM is the standard technique used to obtain detailed intra-atrial activation sequences with the aim of bounding the source of the tachycardia [114, 115, 110].

Some factors might coexist with the tachycardia such as heart disease, hypertension or diabetes that could induce a structural remodeling process and the proliferation of fibrosis. Atrial fibrosis increases also with age and grows in conjunction with cardiomyopathy and heart failure [116]. Fibrosis has been linked to an increased incidence of rhythm disturbances via interaction with healthy tissue [117]. In addition, fibrosis distribution and density have been proposed as a predictor of recurrence in patients after a pulmonary vein isolation procedure by RFA [98].

Detailed biophysical and anatomical models of the atria and torso have been successfully employed to reproduce complex electrical activation patterns observed in experiments and clinics [118, 119]. Most of these studies, however, have focused on understanding the mechanisms that maintain certain types of arrhythmia such as AF [120, 121], or spiral wave dynamics [122], rather than providing solutions to tailor their treatment.

In the last years, the analysis of arrhythmic patterns from non-invasive recordings such as multi-electrode surface ECGs using multi-scale biophysical models is starting to draw some attention as an alternative to EAMs [123, 124, 125, 126]. The use of multi-electrode surface ECG systems allows for dense BSPMs with the aim of improving diagnosis of cardiac arrhythmia. A few attempts have been already carried out in clinics to relate BSPM-

derived indices with atrial arrhythmic events induced artificially from an intracardiac catheter [123]. From the modeling perspective, algorithms have been developed, mainly based on decision trees, to help identify the source of FAT from BSPM data [111, 100]. In those last studies, the presence of fibrosis was neglected or not considered in the models. Ignoring the effects of fibrosis is a clear limitation since current-resistant fibrotic tissue affects the activation patterns.

In this chapter, based on a previously developed 3D atrial model [29], we create 25 new models including fibrosis. Following, the procedure presented in Chapter 3, we create five different distribution of fibrosis, with five different densities, that correspond to the Utah Stages. On these models, we perform electrophysiology simulations of FAT triggered from different location in the RA and LA. Finally, we solve the direct problem in electrophysiology to obtain BSPMs on a torso model coupled to the atria model.

4.2 Methods

4.2.1 Anatomical Modeling

The 3D geometrical model of the atria and torso used in this study was previously developed in [29]. It consists of a highly detailed 3D geometric model of the atria (754,893 nodes and 515,005 hexahedral elements with a homogeneous resolution of 300 μm) coupled to a torso model (254,976 nodes and 1.5 M tetrahedral elements) that includes lungs, bones, liver, ventricles, blood, and general torso (see Figure 4.1A). The atrial model includes specific fiber orientations in 21 different atrial regions (see Figure 4.1C), heterogeneous tissue conductivity and anisotropy ratios and heterogeneous cellular properties adjusted following the model by [100] and summarized in Table 4.1. Those cellular conductivities give rise to AP that mimic the experimental APDs [127, 128, 129, 130].

On the base atrial model, we included 5 different random distributions of patchy fibrosis in the LA. To define the fibrotic regions, we included 50 seeds distributed among the following LA regions: PV, CS, FO ring, and posterior LA wall in different proportions. Based on [131], which analyzed fibrosis distributions from Utah's LGE MRI images available online, we included a larger amount of seeds in the PVs (58%), followed by the atrial roof and floor (20%), and finally the LA lateral wall (22%).
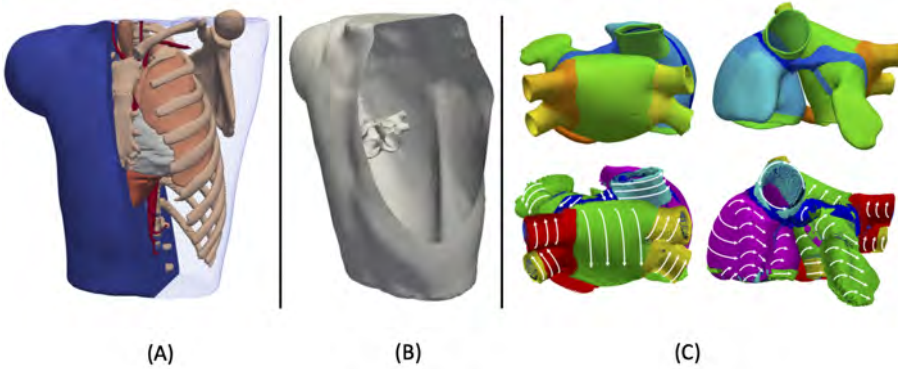
Figure 4.1: Model of the human atria and torso. (A) 3D torso model of tetrahedral elements, made up of lungs, bones, liver, ventricles, blood and general torso. (B) shows the 3D atrial model incorporated inside the torso volume. (C) 3D atrial model, color-coded with the different regions of the atria that show specific cellular and tissue properties, with main fiber orientation defined by white arrows overlapped on the model.

The fibrotic areas were grown according to the Utah classification [98, 99], that defines up to four levels of LA remodeling (quartiles) of fibrosis associated to the ratio of fibrosis to atrial volume [Utah stage I: $< 8.1\%$ (Q1); Utah Stage II: $< 16\%$ (Q2); Utah Stage III: $< 21\%$ (Q3) ; Utah Stage IV: $> 21\%$ (Q4)]. Therefore, from the initial 5 fibrotic distributions, fibrosis was grown. As described in Chapter 3 to avoid a radial growing that will produce circular fibrotic patches, we randomly changed the label of fibrotic patches into healthy tissue before each growing iteration was processed. That way, the fibrotic patches were not completely compact (as it has been observed in histological analysis), and some channels among the fibrotic patches appear. In total we obtained 25 different distributions of fibrosis on the 3D model. Note that from each of the 5 initial distributions, we developed two models for quartile Q4 that we called Stage IV and Stage V. Figures 4.2 and 4.3 shows the 25 distributions of patchy fibrosis used. The figure shows how fibrotic areas (red regions) can have any shape and include small islands of surviving tissue within the patches.

For a given stage the number of fibrotic patches can vary slightly depending on the proximity of the initial seeds and the regions growing. For instance, on State 3, the number of fibrotic patches varies between 31 and 43, however the total volume occupied by the fibroblast ranges $13 - 14\%$. As the stage increase, due to the larger volume of fibroblast the initial fibrotic regions grow to a point in which they merge with each other. Therefore, we have less patches with larger size.
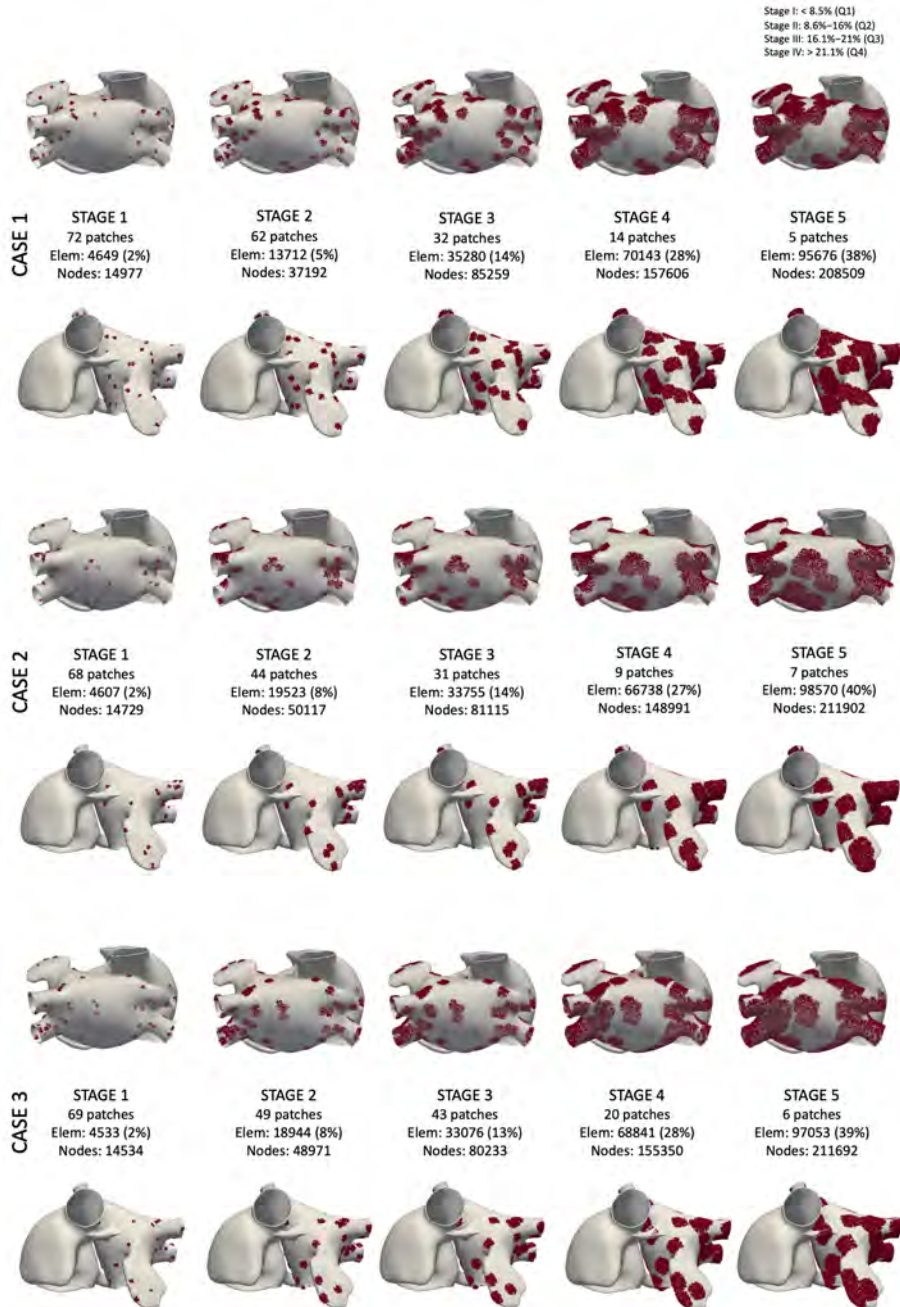
Figure 4.2: Fibrosis distribution for five different stages in Cases 1 to 3. Atrial models showed from two views, where red areas correspond to the fibrotic tissue patches. For each configuration, there is a description including the number of patches, the number of elements assigned to fibrotic tissue and the percentage of fibrosis (based on volume), and the number of nodes assigned to the fibroblast cellular model.
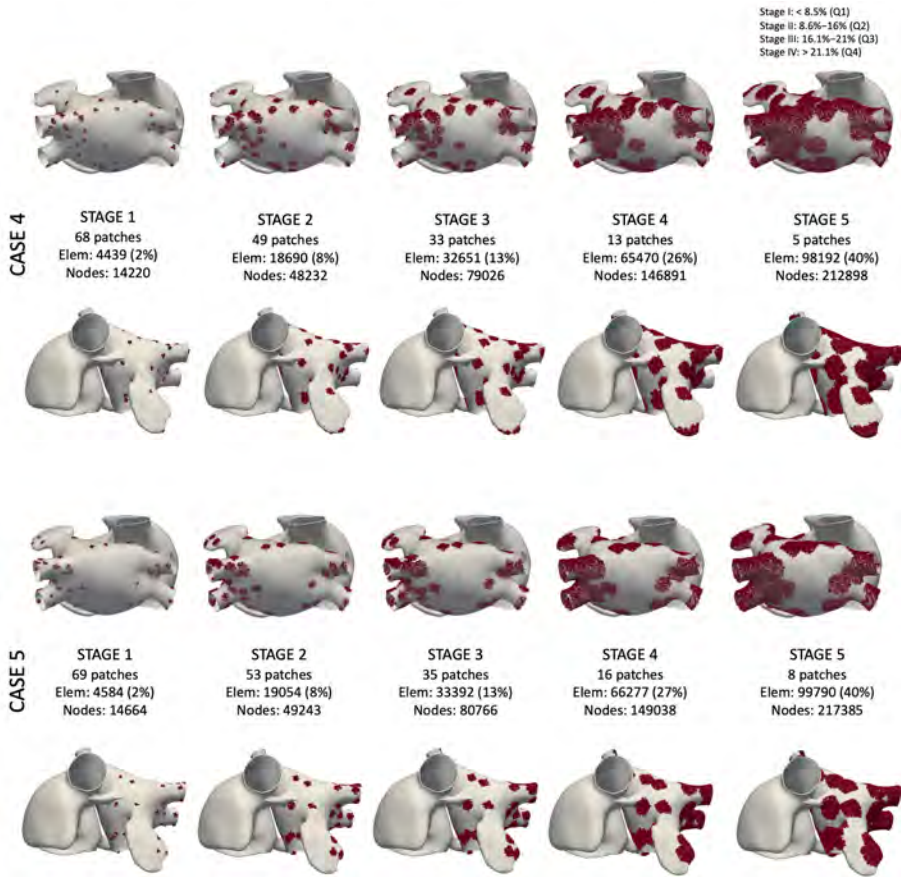
Figure 4.3: Fibrosis distribution for five different stages in Case 4-5. Atrial models showed from two views, where red areas correspond to the fibrotic tissue patches. For each configuration, there is a description including the number of patches, the number of elements assigned to fibrotic tissue and the percentage of fibrosis (based on volume), and the number of nodes assigned to the fibroblast cellular model.

4.2.2 Electrophysiological Modeling

Atrial Electrical Modeling

For the electrophysiology simulations, we considered electrophysiological cellular heterogeneity in 10 different regions by adjusting I_{to}, I_{CaL}, and I_{Kr} in the Courtemanche-Ramirez-Nattel (CRN) ionic model [59], plus the well-established fibroblast cell model by [93] coupled to the CRN model, as we did in Chapter 3. The tissue conductivities for each region defined together with their anisotropy ratios were obtained from [100] and summarized in Table 4.1. The first three rows are the multiplicative factors used for the maximum conductance of three (g_{to}, g_{CaL}, and g_{Kr}) ion channels with respect to the base Courtemanche-Ramirez-Nattel (CRN) ionic model [59], and the next three rows are the longitudinal conductivity (σ_l), the ratio between the transverse and longitudinal conductivities (σ_t/σ_l), and the longitudinal conduction velocity (CV_L).

Table 4.1: Parameters used to reproduce cellular and tissue atrial heterogeneity.

Prop.	RA	PM	CT/BB	TVR	RAA	LA	FO	MVR	LAA	PV	CS
g_{to}	1.00	1.00	1.00	1.00	0.68	1.00	1.00	1.00	0.68	1.00	1.00
g_{CaL}	1.00	1.00	1.67	0.67	1.00	1.00	1.00	0.67	1.00	1.00	1.00
g_{Kr}	1.00	1.00	1.00	1.53	1.00	1.60	1.60	2.44	1.60	2.20	1.60
σ_l	0.003	0.0075	0.0085	0.003	0.003	0.003	0.000	0.003	0.003	0.0017	0.006
σ_t/σ_l	0.35	0.15	0.15	0.35	0.35	0.35	1.00	0.35	0.35	0.5	0.5
CV_L	63.3	115.4	100.0	63.3	63.3	63.3	0.0	62.9	63.3	75.0	97.2
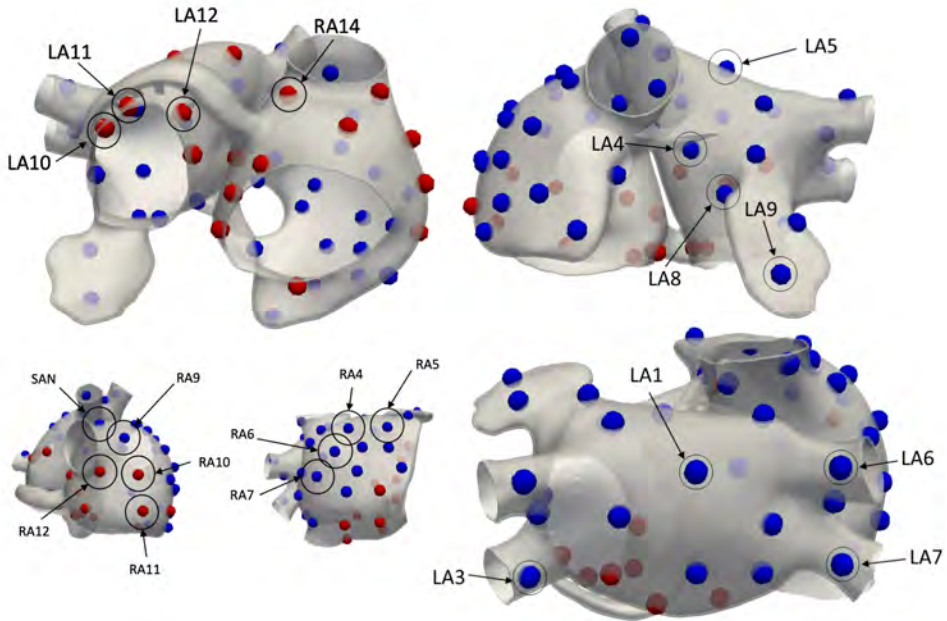
Figure 4.4: Location of 57 simulated ectopic foci on the atrial model marked with spheres. Those locations circled and labeled correspond to the 19 ectopic foci used in simulations that included fibrosis.

Stimulation Protocol

Before starting the FAT simulations, we carried out a stabilization myocyte-fibroblast coupling to ensure that the systems reaches a steady-state. This was necessary since adjacent myocytes and fibroblast interact to each other due through electrotonic currents, as was demonstrated in Chapter 3 and reported in several studies [132]. Since fibroblasts act as electrical sources while myocytes are in resting state, and electrical sinks during the myocyte activation and repolarization phases, myocyte-fibroblast alters the normal myocyte AP. Therefore, we simulated 20 heart beats with a frequency of 2Hz (BCL=500ms), stimulating from the SAN region. After the stabilization, the values of all the concentrations for each cell on the 3D model were stored and used as an initial condition for the FAT simulations.

To simulate the FAT, we consider 57 initial locations for the ectopic foci in an atria without structural disease (no fibrosis), and 19 locations for the 25 configuration of fibrosis, which made a total of 57 plus 475 simulations. Triggering points were present in both LA and RA, and were chosen to

cover most of the atrial wall, in regions prone to elicit ectopic activity. Only in the case of the atrial model without fibrosis, did we consider an additional set of 38 extra triggering points in order to have more information on the healthy activation maps as in [100]. Figure 4.4 shows the location on the atrial model (red and blue spheres) of the 57 ectopic foci used for the model without fibrosis. From those locations, we highlighted using a black circle the ectopic foci used in the cases with fibrosis. A label is included to easily associate the ectopic focus location to a particular simulation. Those locations were selected to match those reported in clinical studies [133].

Multiscale Simulation

The computation of the electrical propagation in the atria was calculated solving the reaction-diffusion, mono-domain equations, given by [101] with the finite element method using the operator splitting numerical scheme by ELVIRA FEM solver [69]. We used implicit integration for the parabolic partial differential equation (PDE) of the monodomain model (tissue level) and explicit integration with adaptive time stepping for systems of ordinary differential equations (ODE) associated with ionic models used at cellular level. The spatial discretization to solve the equations was dependent on the atrial FEM model, that have a fixed element length resolution of $300\mu m$. Time discretization (dt) was set to $20\mu s$.

Computational simulations of cardiac EP solved with ELVIRA software, were run on a multi-CPU computer (running Scientific Linux release 6.9, Carbon). In particular, the hardware architecture included 128 GB of RAM, and 4×64-bit AMD processors (Opteron 6376 processor) with a total of 64 cores at 2.3 GHz. The whole simulation study (532 simulations) took three months to be completed.

Torso Electrical Modeling

The extracellular potentials V_e in the torso model coupled to the atria were calculated using an approximation of the bidomain model. Note that, extracellular space is missing in monodomain model, which was the approach used at tissue level for our electrophysiology simulations. Therefore, to obtain the V_e, first we have to interpolate the transmembrane potentials (V) obtained in the hexahedral mesh nodes of the atria to the tetrahedral torso mesh, overlapping the atrial region. The second step corresponds to the

calculation of the extracellular potential, V_e, by solving the passive term of the bidomain model [134], Equation 4.1, using the finite element method with Dirichlet and Neumann boundary conditions [135].

$$\nabla \cdot \left(\mathbf{D}\nabla V\right) + \nabla \cdot \left((\mathbf{D}_i + \mathbf{D}_e)\nabla V_e\right) = 0 \; in \; \Omega_H \qquad (4.1)$$

where D_i and D_e are the volume-average conductivity tensors of the intra- and extracellular domains [136]. Considering the assumption on conductivity tensors from monodomain approach with previous equation, we obtain,

$$\nabla \cdot \left(\mathbf{D}\nabla V_e\right) = \frac{-1}{1+\lambda}\nabla \cdot \left(\mathbf{D}\nabla V_m\right) \; in \; \Omega_H \qquad (4.2)$$

$$n_H \cdot \left(\mathbf{D}\nabla V_e\right) = 0 \; on \; \partial\Omega_H \qquad (4.3)$$

where $\partial\Omega_H$ is the interface between the atria and the surrounding medium, and n_H is the unit vector normal to the external atria surface pointing outwards. Finally, we compute the extracellular potential in the torso domain by means of the Laplace equation,

$$n_H \cdot \left(\mathbf{D_T}\nabla V_T\right) = 0 \; on \; \partial\Omega_T, \qquad (4.4)$$

where V_T represents extracellular potentials within the domain of torso model (except for the ventricles) and D_T is the heterogeneous conductivity tensor of the 3D torso model defining the conduction properties specific to each organ.

Note that specific conductivity values were assigned to each organ included in our torso model as follows: bone (0.02 S/m), liver (0.0277 S/m), lungs (0.0389 S/m), blood (0.7 S/m), general torso (0.239 S/m). General torso conductivity was calculated as an average of the conductivities of several other tissues, including the skeletal muscle that was not considered as a specific region in the 3D torso model. The conductivity for all the organs was considered isotropic, except for the atrial models that included fiber orientation in all regions.

The temporal resolution used to solve the extracellular potential at the torso mesh was 1ms.

BSPM data Processing

The extracellular potential was calculated on torso mesh for each atrial simulation, obtaining the ECGs with a resolution of 1ms at all the torso
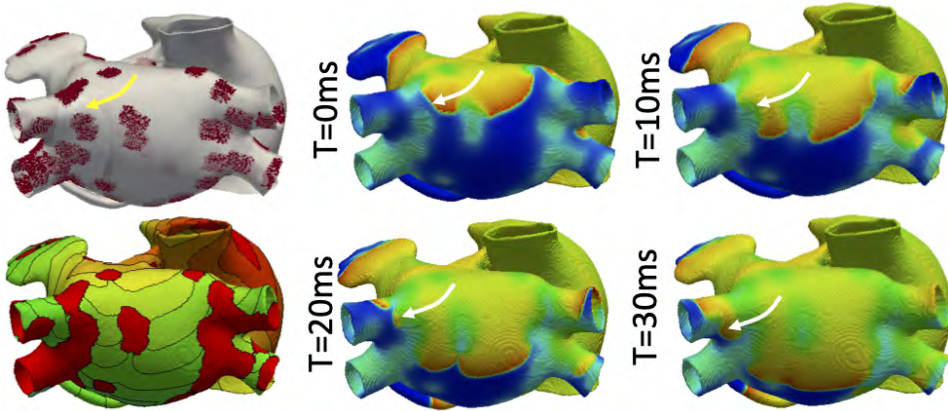
Figure 4.5: Changes in atrial activation sequence due to fibrosis. It can be appreciated a delay in propagation at T=0ms in the area of the PVs (white arrow), that crosses a conduction channel after 30ms. The areas associated to the conduction channel allowed that electrotonic interactions activated other regions but did they not show a full AP (red areas, first column, second row).

nodes. Following the approach in [100], we obtained for each simulation a biomarker based on the integral of the P-wave, i.e., the body surface potential integral map (BSPiM) [133]. This integral map represents the area under the P-wave (for each torso computational node), between the zero line and the curve outlined from the P-wave onset to its offset. These two fiducial points are defined as the time at which the atrial depolarization starts from the ectopic focus and the time at which the latest atrial node is already depolarized, respectively. That biomarker was very convenient cause after performing the integral of the P-wave, each signal was resumed into a number, and the whole BSPM could be summarized in an image, which allowed the easy comparison of results. The whole simulation BSPiM set was normalized globally between -1 and 1.

4.3 Results

Once the atrial simulations were completed, from the 475 simulations that included fibrosis, 54 of them were excluded because they did not trigger the FAT activity due to the proximity between the ectopic location and the fibrotic tissue. The excluded simulations were 5 from the Stage 3, 20 from the stage 4, and 29 from the stage 5.

Activation maps for stages with more than 15% of fibrosis showed both conduction blockades and delays in propagation, fundamentally around the PVs (see Figure 4.5), but also in some critical areas that prevented the electrical communication between both atria through standard pathways. For instance, as can be observed in Figure 4.5, there is a delay wave propagation in the region of the PVs of around 30ms. There were narrow conduction channels (see spaces between red patches in the top row, first column) that only allowed the conduction of electrotonic currents that did not reach the minimum threshold to trigger a full AP within the channel, but allowed to activate the tissue at the channel exit (see white arrow). In the LAT map (first column, second row) the areas where electrotonic currents allowed the activation of the pulmonary vein (white arrow) are depicted in red because the tissue was not considered fully activated within the conduction channel.

As expected the larger changes in LAT maps were for stages 4 and 5 due to the conduction delays and blockades that changed the standard activation sequences (see Figures 4.6 and 4.7). In Figure 4.6, we have the LAT map corresponding to the normal sinus node activation, i.e. not associated to FAT, for the 25 fibrotic models. Since all the models were activated from the same location (the SAN) the resulting LAT maps should be equivalent, and changes could only be due to the presence of fibrosis. For stages 1, 2 and 3, the only differences were areas not activated (solid red regions in PVs), and small delays in the propagation (observable on the isochrones contours), but as can be observed under the white arrows the sequence of activation proceeded normally. However, for stages 4 and 5 we observed large changes.
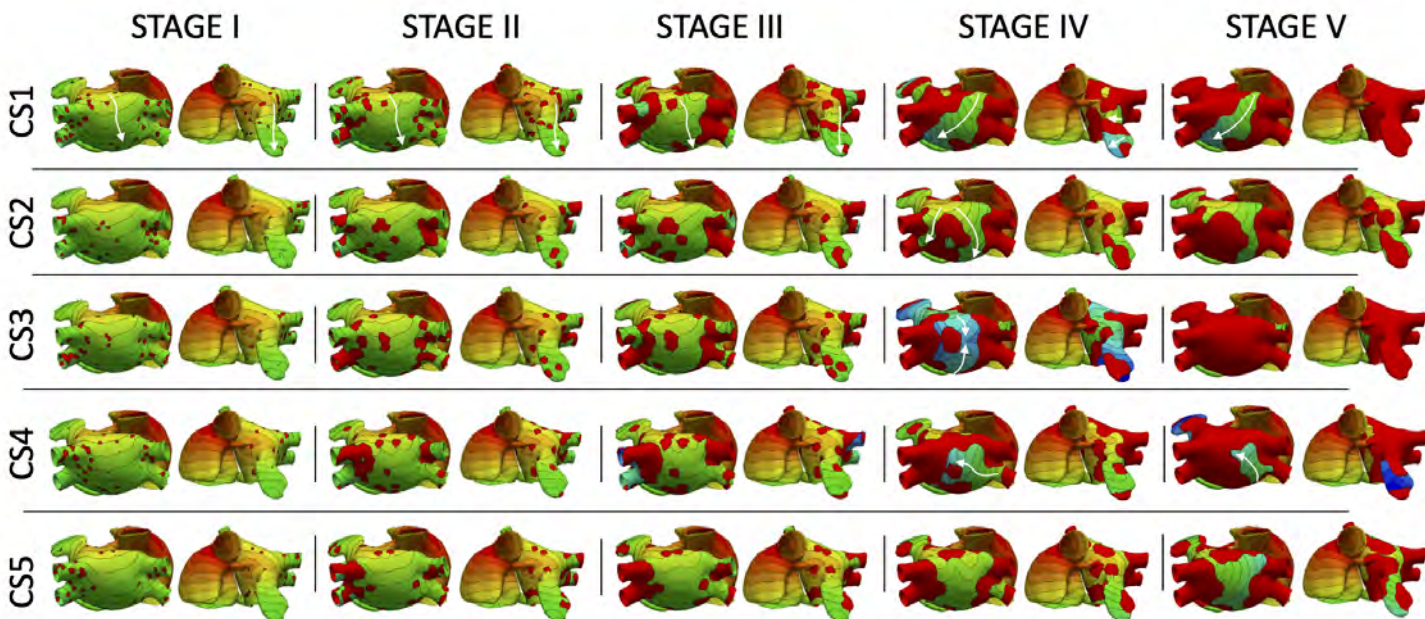
Figure 4.6: LAT maps for the 25 models including a fibrotic substrate in sinus rhythm.

In stage 4, there were conduction delays that alter the normal sequence of activation, as can be seen by the bluish colors in the LAT maps. For instance, for CS1 and CS3 (stage 4), due to a fibrotic barrier at the LA roof, the activation sequence was deviated and activated the lateral wall following a direction different to configurations with less fibrosis (see white arrow). Other cases, such as CS3, stage 4, were more serious since the fibrotic patches delays the conduction on the BB, which is one of the main fast communication ways between both atria. As a result there was a large delay between the activation of the RA and LA (bluish areas), and a change in the activation sequence (see both white arrows), that activated from the roof and base of the LA.

In stage 5, which correspond to high fibrosis density within level IV of Utah classification, there were complete conduction blocks. For instance, CS3 suffered a block in all the communication channels between atria, which prevented any activation generated in the RA to reach the LA. In other cases, activation was delayed, or simply activated the few regions that were not affected by fibrosis. This configuration was very extreme and would correspond to very damaged atria that cannot activate or contract normally.

The 25 fibrotic configurations show very different activation maps when triggered from ectopic foci distributed on the atria. Figure 4.7 shows the activation for CS1, activated from 6 different locations, 4 in the LA (LA1, LA3, LA4 and LA5), and 2 in the RA (RA5 and RA10) (see Figure 4.4 to see correspondence with labels). For a complete catalog of simulations from all the ectopic foci locations of CS1, see the Appendix A. Each ectopic focus produced a completely different activation sequence, and therefore the location of the fibrosis patches affected in a different way.
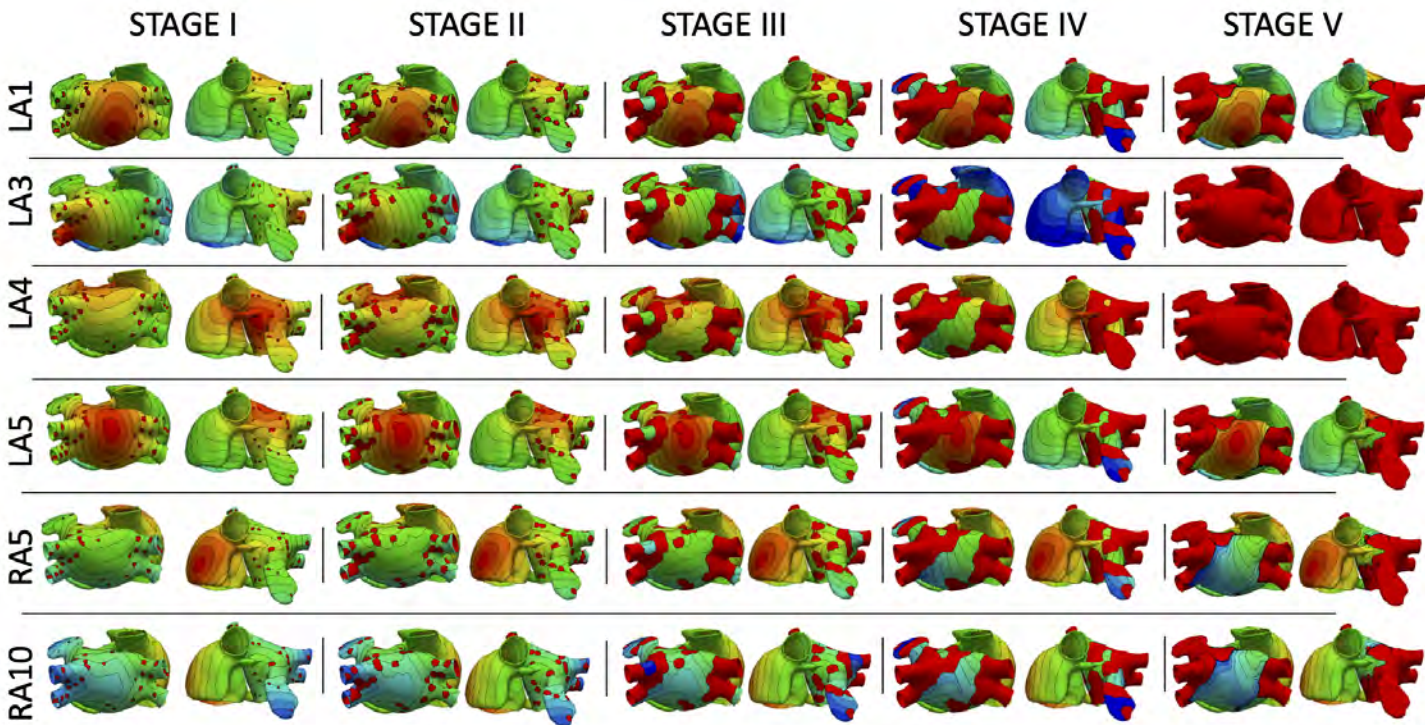
Figure 4.7: LAT maps for Case 1 (CS1, including a fibrotic substrate) triggered from 6 different ectopic foci. Labels indicate the origin of the stimulus.
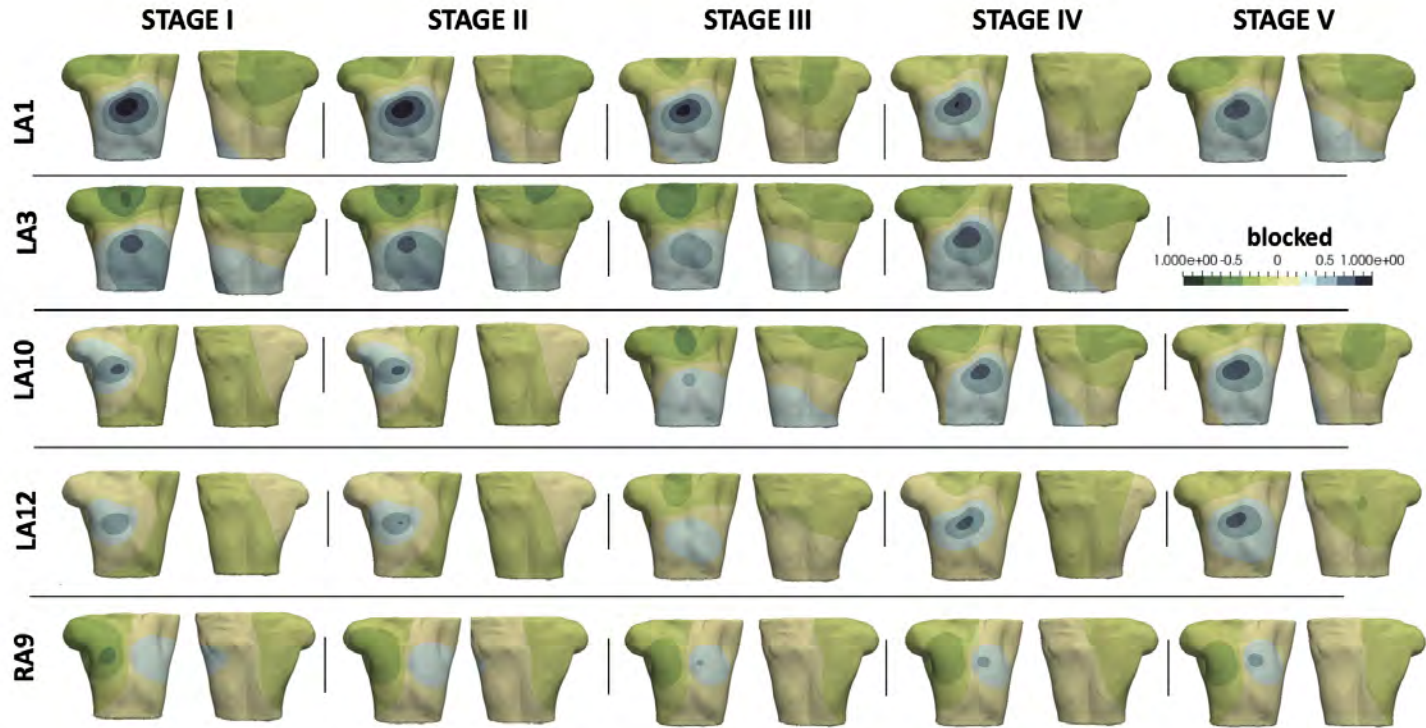
Figure 4.8: BSPiMs for fibrotic Case 1 (CS1) triggered from 5 ectopic foci.

In general, the higher the fibrosis stage, the more the overall delay in the total activation time. However, the largest differences were observed in simulations where special atrial conduction structures were affected by the fibrosis. It is very complex to predict a priori the effects on the activation sequence that fibrosis is going to introduce, specially due to conduction channels that delay the signal but do not block it completely. Therefore, analyzing the BSPiM is the best way to differentiate between cases and understand how the activation patterns changes.

Figure 4.8 shows the BSPiM calculated at all the torso mesh nodes. BSPiM have been normalized using the maximum and minimum values for the whole simulation study. The first remarkable point is the difference in BSPiMs for a given ectopic focus. For instance, LA1-BSPiM and LA3-BSPiM show a very stable pattern, where the location of maximum and minimum values of the map relocate slightly from stage 1 to stage 5. However, other ectopic foci such as LA10 and LA12 show large changes in the pattern, which means that due to fibrosis the surface ECG is going to change so much that could be difficult to predict its origin. Those two ectopic foci are located in the area of the coronary sinus, that connects electrically both atria. Changes in that regions can have large influences in the BSPiM.

Figure 4.9 shows the LAT maps and BSPiM for two ectopic foci, LA1 located in the posterior LA wall and LA10 located in the area of the bicuspid mitral valve ring embraced by the coronary sinus. LA1 activation sequence was not greatly affected by the fibrosis along the different stages, except for the left atrial appendage and the pulmonary veins which did show very low voltage potentials that did not contribute to the activation sequence (Figure 4.9A, red regions). The corresponding BSPiM patterns showed little differences where the maximum values drifted slightly and the isochrones expanded. On the other side, LA10 showed important differences between stages for several reasons.

Firstly, the communication between atria through Bachmann's Bundle was compromised, delaying the activation of the RA. Second, the activation of the LA appendage was also delayed as happened with LA1. As a result, LA10 BSPiM for stages 4 and 5 resembled LA1 more than LA10, which could hamper the training system that classifies ectopic foci.
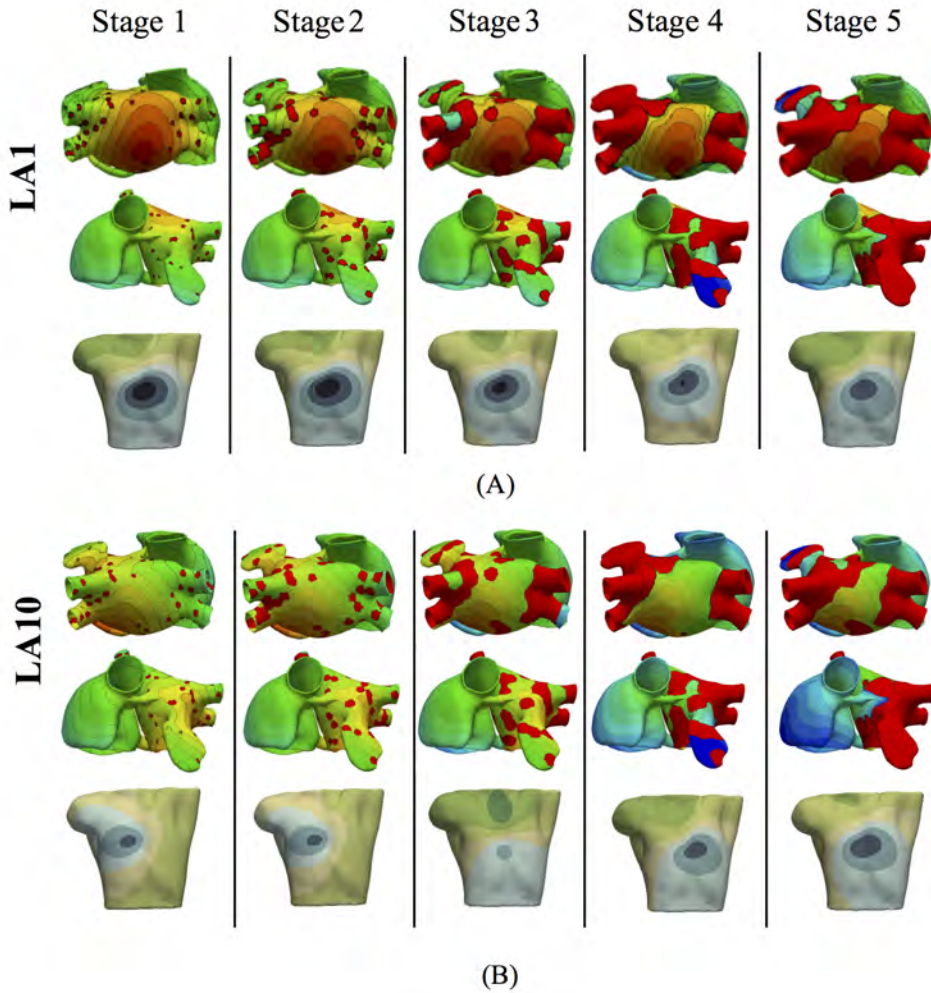
Figure 4.9: Local activation time (LAT) maps and BSPiMs generated by ectopic foci (A) LA1 and (B) LA10 for the 5 Stages of fibrosis and simulated for the Case 1, and the 5 stages of fibrosis.

4.4 Discussion

In this Chapter, we have build a computational model of the atria that includes different distributions and densities of fibrosis. The goal was to study how the fibrosis affects the sequence of activation of the atria at organ level as well as body scale when simulating FAT. We obtained the corresponding BSPMs for each FAT atrial activation and observed large changes in the patterns due to conduction blocks and propagation delays produced by the fibrosis patches. In [131] it was also pointed out the marked conduction delays and enhanced uni-directional propagation with both anisotropy and structure remodeling. In [137], they used a fibroblast model based on Maleckar [60] coupled to the human CRN atrial myocyte to investigate the effects of fibrosis on simulated 12-lead ECG. They concluded that fibrosis causes low amplitude and wide P waves at normal heart rate and significant prolonged and inverse P waves. Our simulations agreed with that observations, where for instance, in Figure 4.8 can be easily appreciated changes in the maximum values of the BSPiM, which are correlated to signal amplitude. This changes are mainly due to the disorganized activation and the inhomogeneous advance of the depolarization wavefront that has to skip obstacles and it is delayed in some regions. This is also the reason why there is not a clear evolution pattern as fibrosis increases, and it is difficult to predict the outcome of a given simulation.

We choose to model fibroblast at cellular level (McCannell fibroblast model [93]), and tissue model (decreased tissue conductivity), and couple them to the CRN atrial cellular model. Boyle et al. [108] and Roney et al. [89] reviewed the different techniques to model the fibrotic substrate for atrial arrhythmias. Other approaches to model the fibrotic substrate included, decrease in CV and anisotropy of affected tissue [138](due to CX43 downregulation, and lateralization of connexin-43). Atrial models incorporating transverse collagen deposition (as in reparative fibrosis) have highlighted the significant interruption and disarray in atrial conduction patterns caused by it [139, 140]. Furthermore, it was established that not only the total amount, but also the specific spatial distribution of collagen deposition (e.g., as generated by a stochastic algorithm) governed the occurrences of conduction block. This conclusions match exactly our observation from the simulation study carried out in more than 400 activation patterns. Our approach to include the effects of fibrosis has been extensively used in other computational works that model in 3D the LA [141, 142, 143]. Those studies found that for fibrotic lesions typical of human remodelled atria under the condi-

tions of persistent AF, gap junction remodelling in the fibrotic lesions was a necessary but not sufficient condition for the development of AF following a PV ectopic beat. The sufficient condition was myofibroblast proliferation in these lesions, where myofibroblasts exerted either electrotonic or paracrine influences on myocytes within the lesions.

4.5 Conclusions

In this Chapter, a coupled myocyte-fibroblast model has been used to investigate the effects of atrial fibrosis at human atrial levels. The virtual BSPM was also calculated to explore the index of clinical diagnosis of fibrosis during FAT. The results show that the fibrosis can greatly modify the atrial activation pattern, slow down wave propagation, conduction blocks and have rate adaptation. Fibrosis patches caused atrial electrical heterogeneity, and large changes in the BSPiM as a function of the fibrosis distribution. However, the increase of fibrosis affected in a different way as a function of the FAT origin, making it more difficult to relate some BSPiM to a FAT origin in certain cases. One of the major repercussions on the BSPiM was observed when fibrosis affected the conduction links between both atria.

A Machine Learning Pipeline to Study the Origin of FAT

Abstract – A machine learning (ML) pipeline that combines an unsupervised learning model and support vector machines was developed to learn the BSPiM patterns of each of the 532 activation sequences performed in Chapter 4, and relate them to the origin of the FAT source. Classification results were mostly above 84% for all the configurations studied when a large enough number of electrodes were used to map the torso. However, the presence of fibrosis increases the area where the ectopic focus can be located and therefore decreases the utility for the electrophysiologist. The results indicate that the proposed ML pipeline is a promising methodology for non-invasive ectopic foci localization from BSPM signal even when fibrosis is present.

96

5.1 Introduction

One of the main goals of the patient-specific cardiac models and related simulations technologies is the development of decision-based support systems that can aid doctors in personalized planning and treatment for ablation procedures [144, 3]. In that direction, there have been already some promising attempts by Zahid et al. [145] that compared model-predicted optimal ablations with clinical lesions that rendered arrhythmia non-inducible. Although that particular study was retrospective, all the patients underwent a recurrent post-procedure (due to left atrial flutter). A patient-specific model for each patient reconstructed from LGE MRI was able to predict the atrial flutter from the information of the first intervention, and the optimal ablation site to remove all arrhythmia in 7/10 patients. Other studies such as [119] focused on development of 3D virtual human atria with the aim of studying multi-scale electrical phenomena during AF arrhythmogenesis. In the same line, in [146] was demonstrated that a patient-specific modeling approach could identify non-invasively AF ablation targets prior to the clinical procedure.

One of the main drawback of the approaches based on multi-scale biophysical simulations is the requirements imposed, including: necessity of high computational power, time to perform simulations, expertise to build patient-specific models, and interpret results. That is the reason why novel approaches based on machine learning combined with multi-scale simulation are starting to be proposed for different clinical applications [147].

Based on the widely accepted principle that the origin of the ventricular activation largely determines the QRS complex morphology in 12-leads ECGs, in [148] the authors present an autoencoder model with inter-subject variations based on Sequential Deep framework (LSTM) that aims to separate the factors of variation within time series ECG data, when learning to predict the origin of ventricular activation. In order to acquire the necessary data to train the model, the authors use Pace Mapping, activating different sites of the ventricle and they also use patient specific models. The model learns from the ECGs obtained during the pace-mapping procedure, and requires patient specific anatomical data.

From patient specific pioneer models [149] that try to extract some rules (from multichannel ECG recordings) that are then interpreted by a doctor to localize the origin of the VT (i.e. not automated) to the current ML based research, there has been a high number of approaches. In [150] multiple

linear regression models were used, where the accuracy was highly influenced by the distance to the pacing sites (possibly overfitting the ML models) while in [151] the authors calculate patient-specific regression coefficients to predict the location of unknown sites of ventricular activation origin ("target" sites). In [152] the authors localize the ventricular segment (1/10) with the origin of the VT using support vector machines (SVM), and in [153] a template matching technique, with 16 segments, was proposed on the time integrals of QRS complexes. A common problem of this approaches is the low accuracy obtained with new patients.

Regarding atrial arrhythmia, there have been studies to characterize AF using in silico or clinical contact electrograms [154], as well as for the automated location of in silico re-entrant drivers using electrograms [155]. Different studies highlighted the need to localize the origin of the ectopic foci non-invasively providing potential distribution on the torso surface based on the analysis of the ECG and BSPM [100, 156, 157, 158]. These studies drew interesting conclusions about P-wave morphology (mainly related to lead V1) or specific RA-paced regions [158]. Although several shortcomings prevented authors from clearly relating torso surface electrical phenomena to atrial myocardial events, short time after BSPM arose as an integral part of the mapping protocol during radiofrequency catheter ablation procedures, the use of BSPiM shed much more light on how to noninvasively determine the arrhythmogenic target region for ablation using a single beat analysis approach [159].

In this context, there are also relevant computational approaches, such as, decision trees based on the P-wave morphology which have been used for the identification of the anatomic triggering atrial sites [111, 160]. In this last work, the tree was able to correctly identify the focus in 93% of the experimental cases while the accuracy decreased to an average of 85% (and even lower with biphasic P-waves) with their simulation results. In [161] authors aims to obtain the triggering site of the stimulus from a 64-lead ECG system with a success rate of 93%. This approach is based on dividing both the torso and the atria in 8 quadrants and used the P-wave polarity to quantify the differences in morphology.

These computational approaches have evolved to more complex algorithmic combinations and machine learning techniques. Regarding to machine learning techniques, in [124] the authors are focused on predicting ventricular pacing sites and in [162]] on classifying cardiac excitation patterns during atrial fibrillation on tissue patches. In [124] a set of features obtained from

simulated BSPM signals are learned using Kernel Ridge Regression.

In this chapter, we aim to predict the triggering site of a FAT using only BSPM data to help electrophysiologists pre- and intraoperatively, reducing the time to find and ablate the source. To achieve this goal, we have to be able to relate a BSPM-derived index with the source of a FAT even in the face of fibrosis patches that are present in different distributions and densities. We have used a single feature, the BSPiM, from a set of features analysed such as maximum, minimum, root means square and integral maps and then we train a SVM model. A difference with previous works is that in [124] they try to learn and predict the full ventricular activation time, whereas we associate each BSPiM to a class, which is related to a focal ectopic site. In addition, we set out to ascertain the effect of fibrosis on the BSPM-derived indices. The proposed method uses machine learning techniques to develop a prediction pipeline that should be able to learn the relationship between BSPMs and ectopic foci location. We trained this system with a simulation database, generated by means of a detailed biophysical model of 3D human atria, in which we have control of the input parameters, and can simulate the desired scenarios.

5.2   Methods

The simulation of ectopic foci in Chapter 4 allowed us to obtain a data set formed by the ectopic locations on the atria (3D points) and the corresponding BSPiMs they produced on the torso. Using this data set, ML techniques could be applied to establish a relationship between the location of an ectopic focus and the BSPiM map it produced. Following this idea, we designed the pipeline shown in Figure 5.1 to solve the ectopic localization problem. This pipeline had five main steps. Firstly, we performed the simulations for every ectopic focus on the atria and obtained the corresponding BSPiM. Next, we performed a dimensionality reduction on the BSPiMs, followed by a clustering of BSPiMs. We validated all the clusters obtained to evaluate their quality. Finally, we performed a stratified cross-validation, to assess the classification accuracy of the ectopic foci into the different clusters defined. Note that in this context, a cluster of ectopic foci corresponds to a region on the atria.

The first two steps in the pipeline can be considered as a pre-processing stage, and they were necessary to generate and reduce the resolution of the raw BSPiMs, which originally had more samples than those in a real clinical
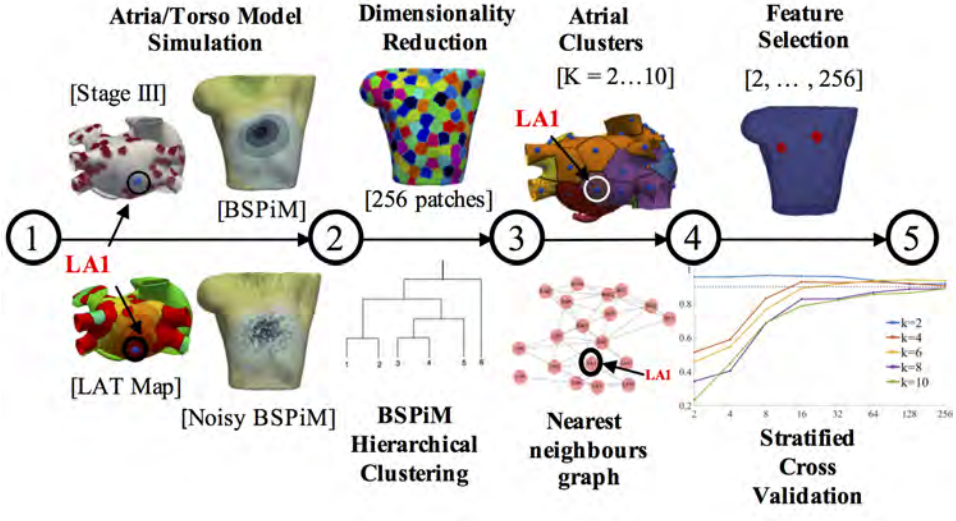
Figure 5.1: Machine learning pipeline. The pipeline consists of 5 steps. Steps 1 and 2 are performed for each ectopic focus and fibrosis configuration. Steps 3, 4 and 5 are the training and validation phases and carried out with all the simulation results. The different torso and atrium figures shown correspond to ectopic focus LA1, located on the LA posterior wall.

setting. In this pipeline, we used two datasets, one corresponding to the 57 ectopic foci simulated without fibrosis, which contained 57 activation sequences. The second data set corresponded to the 25 fibrotic configurations × 19 triggering locations containing 475 activation sequences.

5.2.1 Atria/Torso Model Simulation

In this step, we made use of the original BSPM simulated in Chapter 4. To obtain more realistic results, we added white Gaussian noise to simulate the effect of noise from muscles or other sources on the BSPM. An average P wave had a mean power of 0.003 mW (i.e., -55.2 dBW), and we added white Gaussian noise with a mean power of 0.001mW (i.e.,-60.0 dBW), yielding an approximate power ratio of 3 and S/N ratio of 4.8 dB. Afterward, we filtered the signal using a Savitzky-Golay smoothing filter that minimizes the least-square error in fitting a polynomial to frames of noisy data. It is optimal in the sense that performs much better than the standard FIR filters, which tend to filter out a significant portion of high frequency content along with the noise [163]. Once all the filtered noisy BSPMs were

obtained, the body surface potential integral maps (BSPiM) were calculated, as described in [159]. As a result, for each ectopic focus simulated we summarized each P-wave signal on the torso surface into a single value obtained from integrating the corresponding P-waves at each torso point, which resulted in the BSPiM. The integration of the BSPiM is equivalent to the average of the electrical cardiac vector over time, and therefore Figure 5.1 (step 1) contains the activation patterns produced by the ectopic focus LA1 (located on the LA posterior wall), for a configuration with fibrosis remodeling in stage III, together with the corresponding BSPiM with and without noise (frontal views) for the same ectopic focus.

5.2.2 Dimension Reduction and BSPiM Clustering

This step corresponded to an unsupervised learning phase to classify the filtered noisy BSPiMs that result from the activation of the different ectopic foci (457 + 57 simulations). The computational torso model used in this pipeline had 14,157 surface nodes, and therefore provided BSPiMs with that resolution. Before the clustering phase, these dense BSPiM data sets were reduced to a more feasible clinical scenario, since current BSPM vest system technologies allow a maximum of about 256 electrodes placed on the torso of a patient [123]. Therefore, the dimension of each input data set of filtered noisy BSPiM, was homogeneously reduced to a maximum of 256 nodes, (i.e., features) (see Figure 5.1, step 2, top). To select the nodes, we divided the torso domain into 256 equally-sized patches (55 nodes per patch in average), and choose randomly one of the nodes in each patch to represent the whole region. This is a sensible approach since in a clinical BSPM acquisition system the exact location and spacing of the mapping electrodes may not be perfectly preserved across patients.

The unsupervised clustering of the 256-dimensional BSPiM patterns was performed using hierarchical/agglomerative clustering. One of the benefits of hierarchical clustering is that one does not need to know in advance the number of clusters K in the dataset, assigning each sample to its natural class. We used the Ward et al. variance minimization algorithm [164].

We started with a single cluster for each sample and iterated by finding, at each step, the pair of clusters that, after merging, produced the minimum increase in the total within-cluster variance. We also used dendrograms for visualization in the form of trees showing the order and distances of merges during the hierarchical clustering process.We repeated this phase imposing

a distance limit in the algorithm, obtaining K clusters ranging from 2 to 10 clusters (see Figure 5.1, step 2, down).

5.2.3 Clusters Validation on the Atrial Surface

The association of every BSPiMs to a cluster induced a clustering on the set of ectopic foci that produced the corresponding BSPiM; if a certain BSPiM was assigned a label j by the clustering algorithm, then we assigned the same label to the ectopic location that produced that BSPiM. Now, the question to resolve was whether the clustering that was mapped onto the atria had some geometrical meaning to identify the location of the ectopic focus.

To analyze this, we associated to each ectopic focus a region or patch formed by the points in the atria closer to that focus than to any other. From the clustering induced in the atria, we could associate also a patch to every BSPiM cluster, built as the union of the patches of the associated ectopic foci. In Figure 5.1 (step 3, top) we show an example of the clustering generated on the atria surface. Each atrial patch associated to an ectopic focus has a color that corresponds to its class. In the example, ectopic LA1 (for K = 6 groups and fibrosis Stage III) was associated to the purple class.

Recall that our goal was to build a system that takes a measured BSPiM and predicts the location of the ectopic focus that generated it or, at least, a region where it could be located. Thus, the ideal situation would be that two BSPiM that are in the same cluster are the result of the same ectopic focus or, at least, of two ectopic foci that are in nearby patches in the atria. By contrast, an adverse situation would happen when similar BSPiM would be clustered together due to their similarity, but the ectopic foci that generated them were distributed along the atria and did not form a connected region on the surface. We defined a well formed region/cluster as a union of ectopic patches that was connected and only included ectopic foci from the same cluster.

Thus, we sought to assess the quality of the patches formed from the BSPiM clustering. To be able to verify this requirement we created an ectopic graph, where the nodes represent the ectopic foci and are connected by an edge if their associated patches share a border. The geodesic distances on the atria were obtained by a Fast Marching algorithm (Kimmel and Sethian, 1996). According to the ectopic graph created, a well formed patch could be identified as a connected subgraph containing all the ectopic foci of a

102

class (see Figure 5.1, step 3, down). In this way, we reduced the problem of deciding if a cluster is well formed to a connectivity test on the associated subgraph. It is important to note that for each ectopic location we had 25 simulations (5 different fibrosis configurations × 5 different fibrosis stages) with differing fibrosis distribution. An ideal result would be that all the BSPiM simulations produced by the same ectopic focus end up in the same cluster, regardless of the fibrosis configuration or stage. However, due to the changes in LAT due to fibrosis such a result would have been highly unlikely.

Considering K as the number of clusters, we define the persistence of an ectopic location x as the number of different clusters that contains ectopic foci located at x, divided by the number of clusters, K. The best situation for an ectopic is produced when it only appears in one class (fully persistent), with a persistence value of $1/K$, while the worst situation occurs when it appears in all the classes, with a persistence value of 1. Ectopic locations with a poor value of persistence would indicate that several cluster patches overlap on that ectopic patch. This situation will be represented in our figures with regions that have spots of more than one color. It is noteworthy, however, that a poor persistence value does not necessarily lead to a bad prediction situation. Although an ectopic location is in, say, three clusters, if the three clusters are well formed the system will still be able to indicate a meaningful region for the ectopic when a BSPiM is processed.

5.2.4   Feature Selection

In addition to the dimensionality reduction carried out before the clustering step, we performed a feature selection step, in this case to select the best features among the 256 (see Figure 5.1, step 4, top). The reason for this further selection is that in many clinical procedures the number of available electrodes is far below 256.We wished to establish the minimum number of electrodes necessary to build a successful prediction system and to determine what their optimal locations are.

In our context, we will consider that a feature (representing an electrode location) is less relevant than another when its value is independent of the classification of the sample, from a probabilistic point of view. We performed a hypothesis contrast on the data set to assess the dependence of each component of the BSPiMs data with the class distribution of the samples.

Given a feature, we consider its value and the class of the samples in the data set as random variables. Using the chi-square (Xi^2) test, if a small p-value is found for a given feature, it shows statistical evidence that the value of that feature is not independent from the class of the sample. Then, we keep the N best features and disregard those that are most likely to be independent of the class label. This process is repeated for N = 2, 4, 8, 16, 32, 64, 128, 256, which permits us to compare the performance of the system as a function of the final number of features selected.

5.2.5   Ectopic Foci Classification

As a result of the cluster validation process, the generated clusters can be viewed as groups of patches on the atrial surface that relate to BSPiMs patterns. We trained a classifier able to assign any BSPiM into one of the clusters defined, that would point to a patch group [atrial region(s)]. For each number of clusters (K = 2,...10), we constructed a supervised learning model using a SVM using the implementation in [165, 166]. The SVM does the classification of the data finding the best hyperplane that separates all data points of one class from those of other classes. We used a 4-fold stratified cross validation process where different SVMs were trained to avoid over-fitting and to evaluate the prediction accuracy and the generalization level obtained. We adjusted the parameters (i.e., a regularization term) of a radial basis kernel for the decision function. Folds were selected so that the mean response value was approximately equal in all of them. Each fold contains the same proportion of ectopic foci from each cluster, and all the ectopic foci were tested. Having 4-folds leaves 75% of samples for training and 25% of samples for testing in each fold.

5.3   Results

5.3.1   Clustering of BSPiM Maps

For the clustering, learning, and classification of the ectopic foci we created six different subsets of BSPiMs named M0, ... , M5. Table 5.1 summarizes the data included in each of those models. Model M0 includes the control data set without fibrosis, where FAT is triggered from 57 ectopic foci. The rest of models M1–M5 include fibrosis and are triggered from 19 locations. For instance, model M1 includes cases 1 to 5 with fibrosis stage 1 which

Table 5.1: Models created for the clustering, learning, and classification steps of the pipeline. The table shows the levels of fibrosis and the number of BSPiMs included in each model as data set

Model	Fibrosis	Stages	# BSPiMs
M0	no	-	57
M1	yes	[1]	95
M2	yes	[1,2]	190
M3	yes	[1,..,3]	280
M4	yes	[1,..,4]	355
M5	yes	[1,..,5]	421

makes 95 simulations. In some models simulations that did not propagate were excluded: 5 for M3, 20 for M4, and 29 for M5.

The clustering of the BSPiM maps obtained with the hierarchical/agglomerative clustering predicted a number of groups. Figure 5.2 shows, as an example of the performed hierarchical/agglomerative algorithm, the dendrograms for the model M1. The hierarchy levels (from 1 to 9) as a function of the separation distance (green arrow) are indicated by the horizontal dotted lines, and the clusters (K) being formed at each iteration, which are shown on the y right axis from K = 2 to K = 10. At each iteration the clusters being split have the smallest distance according to the Ward et. al. linkage algorithm [164]. Figure 5.2 shows how in its first iteration the linkage algorithm decided to split the 95 original samples of model M1 in two clusters (K = 2), one with 30 samples (number of samples per cluster shown in blue) and the other with 65 samples, with a large separation distance. In the second iteration, the cluster with 65 samples was divided by the algorithm in two clusters, generating 3 clusters in total with 30, 25 and 40 samples respectively (K = 3). Following iterations keep dividing and merging the data set, up to the imposed limit of level 9 and K = 10, where the clusters formed had few samples and a quite small separation distance, making further iterations pointless in terms of the subsequent classification stage.

The x axis shows the color coded labels of the ectopic foci grouped for K = 10 (i.e., level 9 and last iteration). It is important to recall that a particular ectopic focus should be the same for any of the 5 different distributions of fibrosis (i.e., Case 1 to Case 5). The groups formed are shown separated by a thick black vertical line. At this hierarchy level, the simulations for ectopic focus LA5 (simulated 5 times for M1, corresponding to Case 1 to

Table 5.2: Clustering performance results for the models M0 to M5

K_i	Measure	M0	M1	M2	M3	M4	M5
K2	$\hat{\text{x}} \pm \sigma$	66 ± 41	68 ± 39	78 ± 53	81 ± 49	68 ± 67	84 ± 44
	OR	-	-	10.53	15.79	-	21.05
	CR	100	100	100	100	100	100
	CA	0.98	1.00	1.00	0.99	0.97	0.91
K4	$\hat{\text{x}} \pm \sigma$	33 ± 14	34 ± 16	39 ± 22	40 ± 30	52 ± 28	61 ± 17
	OR	-	-	10.53	15.79	42.11	52.63
	CR	100	100	100	100	100	100
	CA	0.94	0.85	0.93	0.84	0.90	0.90
K6	$\hat{\text{x}} \pm \sigma$	22 ± 10	22 ± 13	27 ± 14	32 ± 20	42 ± 25	44 ± 25
	OR	-	-	15.79	36.84	63.16	68.42
	CR	100	89.4	100	94.7	94.7	94.7
	CA	0.91	1.00	0.96	0.97	0.96	0.93
K8	$\hat{\text{x}} \pm \sigma$	16 ± 9	17 ± 7	20 ± 13	27 ± 15	37 ± 20	43 ± 19
	OR	-	-	15.79	47.37	68.42	73.68
	CR	100	84.2	89.4	94.7	89.4	89.4
	CA	0.92	1.00	0.98	0.96	0.93	0.88
K10	$\hat{\text{x}} \pm \sigma$	13 ± 8	14 ± 8	17 ± 11	24 ± 15	32 ± 17	37 ± 17
	OR	-	5.26	21.05	52.63	78.95	78.95
	CR	100	78.9	84.2	89.4	89.4	89.4
	CA	0.85	1.00	0.98	0.96	0.89	0.88

$\hat{\text{x}} \pm \sigma$: Mean Area ± Standard Deviation (cm^2)

OR: Overlapped ratio (%)

CR: Connectivity ratio (%)

CA: Classification Accuracy - Results for 256 characteristics
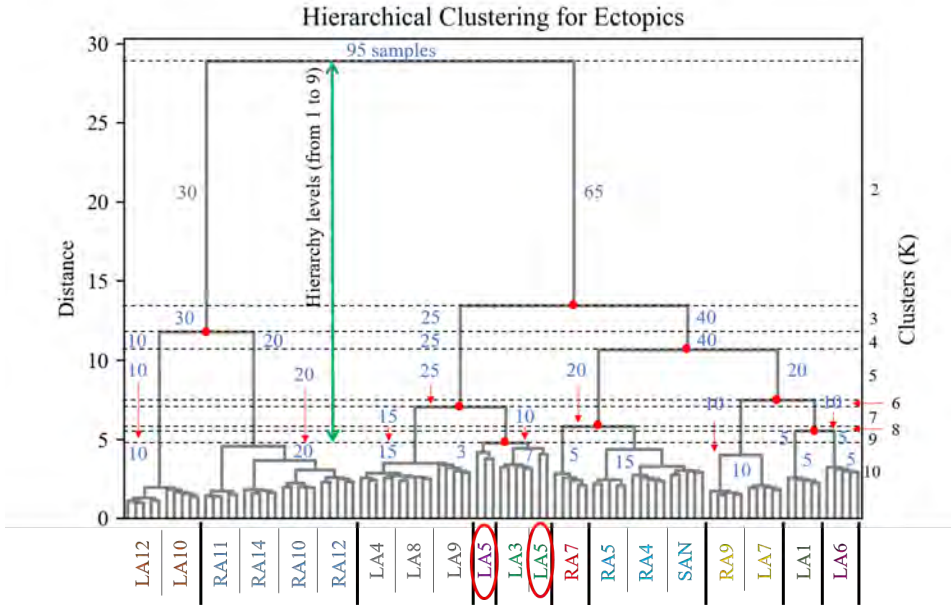
Figure 5.2: Dendrogram of the hierarchical/agglomerative clustering algorithm for the model M1. Hierarchical levels are indicated by the horizontal dotted lines from 1 to 9 (green arrow), the y axis on the left shows the distance between levels, and on the right the clusters being formed after merging and splitting samples (number of samples in blue) at each level from K = 2 to K = 10. The x axis shows the color coded groups of ectopic labels separated by the thick vertical black line. The red ellipses show the particular case of the BSPiM produced by the ectopic LA5, being grouped in two different clusters, 3 samples to cluster 3, and 2 samples in cluster 4.

Case 5) did not fall in the same cluster, but 3 BSPiMs were classified into Class 3, and 2 BSPiMs to Class 4 (see Figure 5.2, encircled labels). This fact indicates how the presence of fibrosis, already in Model M1, starts to affect the BSPiM profiles, and consequently the clustering process. The clustering of the BSPiM maps obtained above corresponds to groups formed by ectopic locations on the atria. When we choose K = 2, for example, all ectopics were arranged into cluster 1 or 2, if we chose K = 6, all ectopics were then distributed into clusters 1–6.

5.3.2 Association of BSPiM Clusters to Regions on the Atria

After clustering the BSPiM maps, we associated to each cluster the ectopic beats that generated the corresponding BSPiM in the cluster. Next, for each cluster, we summed the areas on the atria surface that were linked to each ectopic beat, i.e., the ectopic patches. We obtained this measure for K =2 to K = 10. For example in the case of K = 2 we had the area of cluster 1 and cluster 2, and then calculated the mean area, and the standard deviation in the areas, to obtain a single representative measure of the atrial regions. Note that if a given patch in the atria had two labels (it was expected to have a single label), its area would be summed twice to take into account the existence of region overlaps.

This measure is shown in Table 5.2 as X $\pm$ σ (cm^2). The results show, as expected, a decrease in the mean and standard deviation of the region area as we incremented the number of clusters from K = 2 to K = 10 (row wise). When we analyzed those areas moving from M1 to M5 (column wise), there was an increase of the areas as the level of fibrosis increased. This finding is due to the region label overlap, since when a patch is labeled with more than one label it contributes to the sum of areas of more than one region. Therefore, the sum of all areas of all regions is larger than the area of the atria surface when there is label overlap. This increment is explained with another measure which is the ectopic persistence within the clustering process. Figure 5.3 shows the 19 atrial patches for the models M1, M3, and M5 (an increasing level of fibrosis) color-coded with the assigned label for K =6 and K =8 (in three different atrial views).

Patches with the same color form a unique region that relates to a group of BSPiM patterns. When a patch within a region shows more than one color or label (a region with different colored dots), it means that two different BSPiM could be mapped to the same patch due to the variability introduced by the fibrosis.

Therefore, patches colored as "red" and patches with "red dots" were all considered as a single region. However, our goal was to create regions that were as small as possible, in order to reduce the search area of the ectopic focus.
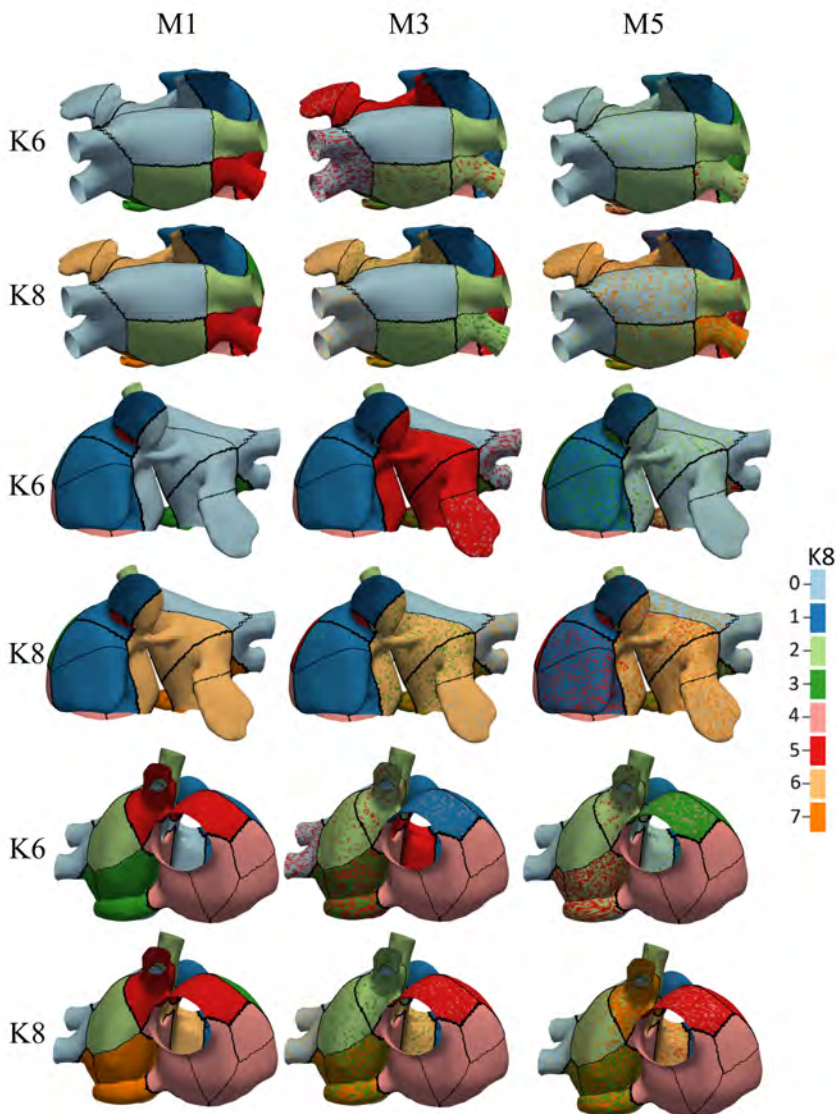
Figure 5.3: Associated BSPiM clusters for models M1, M3, and M5, for K = 6 and K = 8 (color coded) to the 19 patches defined by the atrial ectopic foci simulated with fibrosis (three different views). Regions including color dots indicate that samples of a particular ectopic focus have spread into two or more clusters, and the corresponding atrial patches overlapped on the atrial surface exactly at that ectopic focus. Model M1 shows no overlapping for K = 6 and K = 10, and models M3 and M5 show an intensification of overlapping as the fibrosis stage increased.

5.3.3 Ectopic Focus Persistence Within a Clustering Process

When models with fibrosis were included, they did not cluster properly into non-overlapped groups since BSPiM were highly altered by the conduction blocks. From stage 3 (i.e., 15% fibrosis) onwards the BSPiMs showed large differences for ectopic beats placed in the pulmonary veins, as can be seen in the example of Figure 5.7B, where the LATs of ectopic LA10, from Stage 3 to Stage 5 of fibrosis, show clear blockades at the pulmonary veins and left atrial appendage, and consequently completely different BSPiMs with a lesser level of fibrosis.

From the dendrogram of Figure 5.2 we observed that for the Model M1, when K = 10, due to the variability among these BSPiMs, we found that 3 of the LA5 BSPiMs were grouped into cluster 3 while the 2 remaining BSPiMs (with more fibrosis) were in cluster 4. This result indicates that samples of the ectopic LA5 have been spread into two clusters, so the corresponding atrial patches will overlap on the atria surface exactly on LA5.

In Figure 5.3, ectopic foci locations with poor persistence values show regions that have spots of more than one color, indicating overlap. Figures 5.5 and 5.6 show, as an example, the BSPiM together with their labels for model M3 and K = 6. A given ectopic focus can be classified into two different classes as a function of the fibrosis, e.g., class green and red for LA1.

For the results of the persistence analysis, we calculated the ratio of ectopics that appear in more than one cluster with respect to the total number of ectopic foci in the atria, (i.e., 57 ectopics for model M0, and 19 ectopics for models M1 to M5); Table 5.2 displays this measure as overlapped regions (OR).

The Model M0 (no fibrosis), showed, as expected, no overlap, given that there was no more than one label per ectopic focus (i.e., OR = 0). Results are summarized in Table 5.2. For the models with fibrosis, there was an increase of overlap as we incremented the level of fibrosis from M1 to M5 (column wise) and an increase of overlap as K increased from 2 to 5 (row wise), with the particular case of M1 with no overlap except for K = 10 with LA5 being spread in two clusters and OR = 5.26.
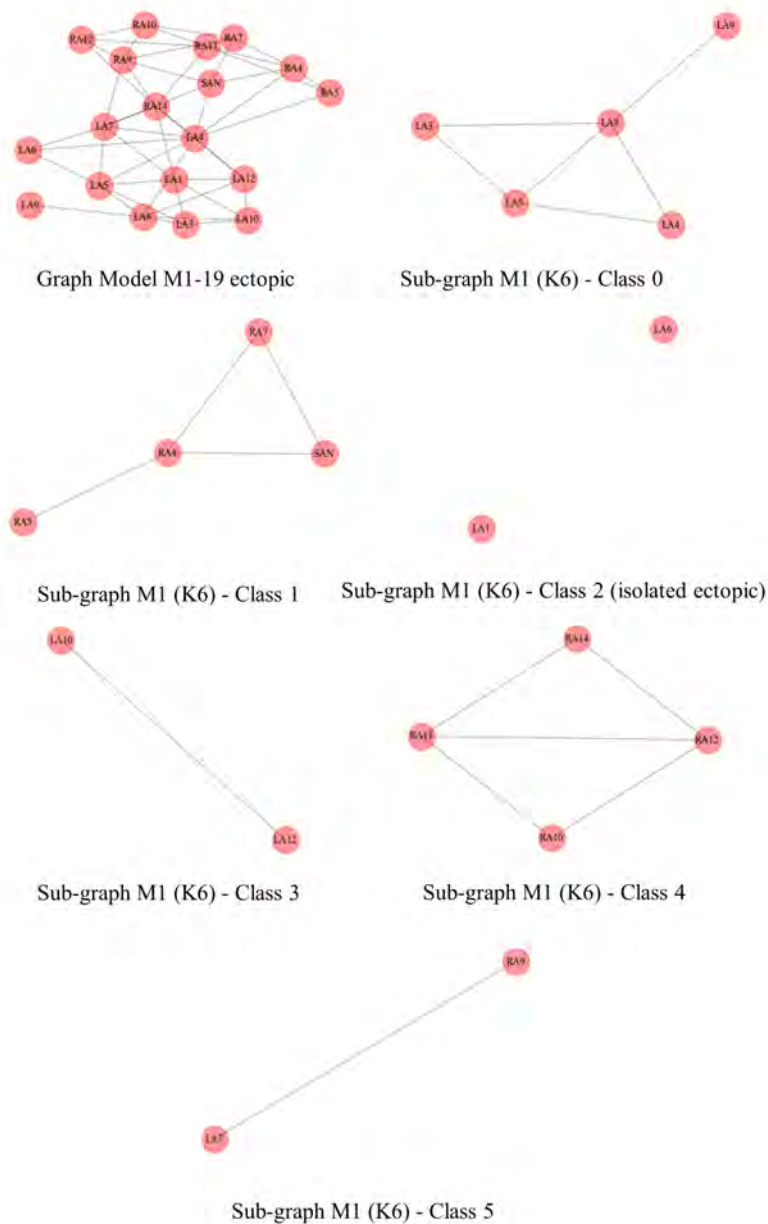
Figure 5.4: Geometrical consistence of clusters. Top row, on the left, shows the complete graph of the atria where the nodes represent the ectopic foci connected by edges. The rest of the figure shows all the subgraphs that represent the classes of the model M1 and $K = 6$. All of them are well formed connected subgraphs, except for the one at the middle row, on the right, representing ectopic foci LA1 and LA6 of the class 2 and indicating no connected nodes.

111

5.3.4 Geometrical Consistence of Clusters

The analysis of the cluster connectivity using graphs permitted us to identify which clusters were not well formed, i.e., were not connected. We always preferred connected regions without holes or islands over the atria surface, otherwise when we associated an ectopic focus to a cluster, the cluster was scattered in several regions of the atria instead of having a connected and delimited one.

We calculated the ratio of well-formed clusters or connected clusters (i.e., well formed over all clusters) as the measure Connection Ratio (CR) from the validation process of the model M0 without fibrosis, and the five model configurations (M1–M5) with fibrosis, for K ranging from 2 to 10 clusters. Results are summarized in the Table 5.2. For the Model M0 (no fibrosis), from K = 2 to 10, the Connection Ratio (CR) was 100%. The results for the model M1 (with fibrosis), for K = 2 and K = 4 show that the connection ratio was 100% and maintained with all models and levels of fibrosis (column wise).When we increased the number of groups from K = 6 to K = 10 (row wise), but also with the increase of fibrosis from M1 to M5 (column wise) there was a variable decrease of the ratio CR, implying the loss of connection or isolation of some ectopics from the groups. This effect depended on the different configurations of the patchy fibrosis (see Table 5.2).

As an example, the Figure 5.4 depicts at the top row, on the left, the complete ectopic graph of the atria with the nodes representing the 19 ectopic foci connected by edges; the rest of the figure shows the 6 subgraphs of each class, formed after clustering the model M1 for K = 6. The subgraph in the middle row, on the right, shows the ectopic foci LA1 and LA6 with no connection, (i.e., 2 isolated nodes with respect to 19 total nodes, therefore a CR of 89.4%).

We observed that the isolated ectopics for the particular case of model M1 were mainly the LA1 and LA5, both located at the center of the posterior wall of the left atrium, lower and upper regions, respectively, and LA6 at the upper Right pulmonary vein. More ectopics were located in the right atrium, RA7 and RA11, right above the pectinate muscles. In the case of the model M2, the isolated ectopics were the same as in model M1, except for LA1; for the models M3 to M5, the isolated ectopics were LA7, at the lower right pulmonary vein, and LA9 at the left appendage.

As can be observed in Figures 5.5 and 5.6, for a given ectopic location BSPiMs change their pattern as the fibrosis stage changes, and therefore

they are reclassified into a different group. For instance, LA3 is classified in the blue group for stages 1 and 2, but changes to the red group in stage 3 for three of the cases. Other ectopic focus, such as LA6 are very stable for the different configurations.
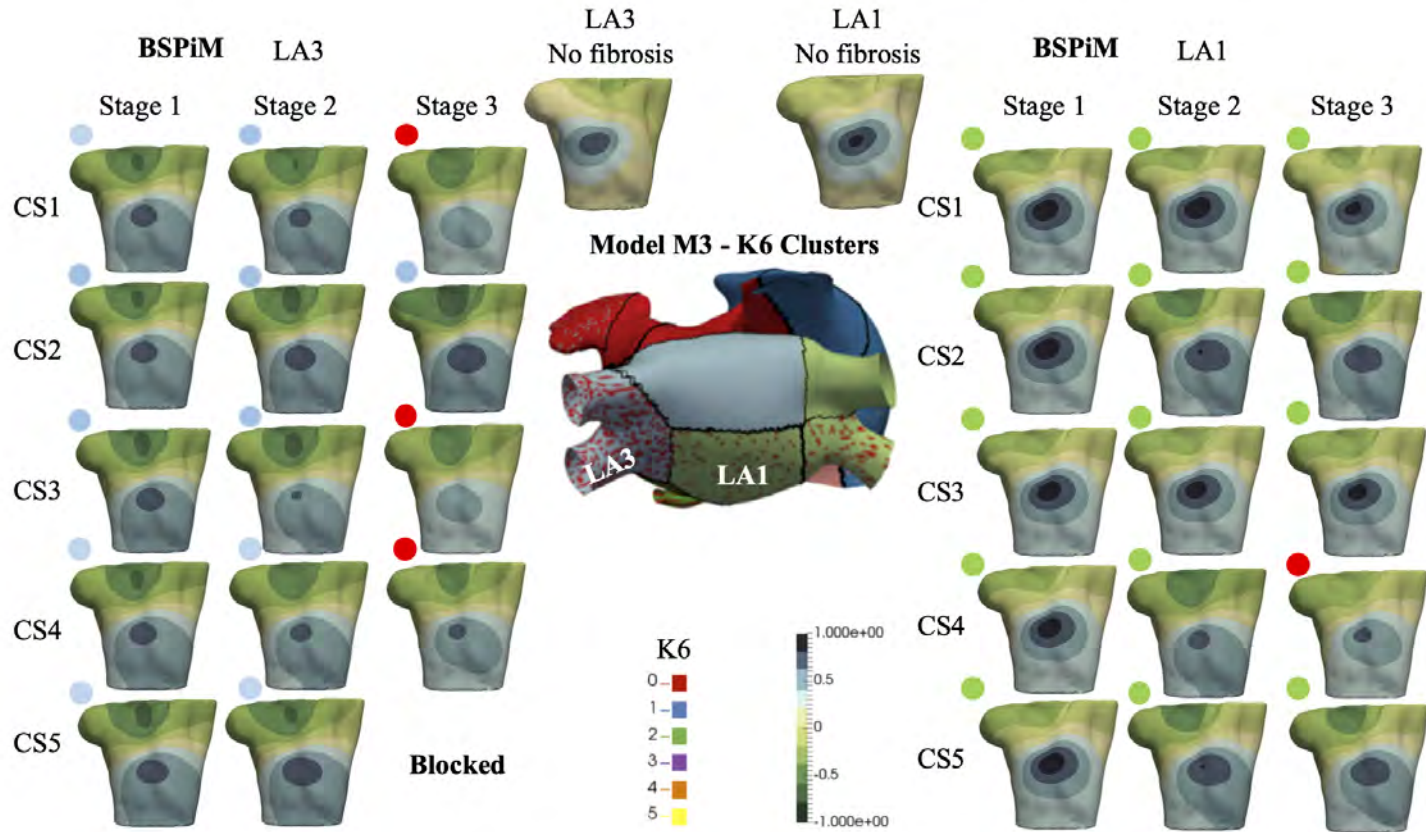
Figure 5.5: BSPiMs for CS1-5, and ectopic locations LA1 and LA3. The color disc indicated the class assigned to each BSPiM.
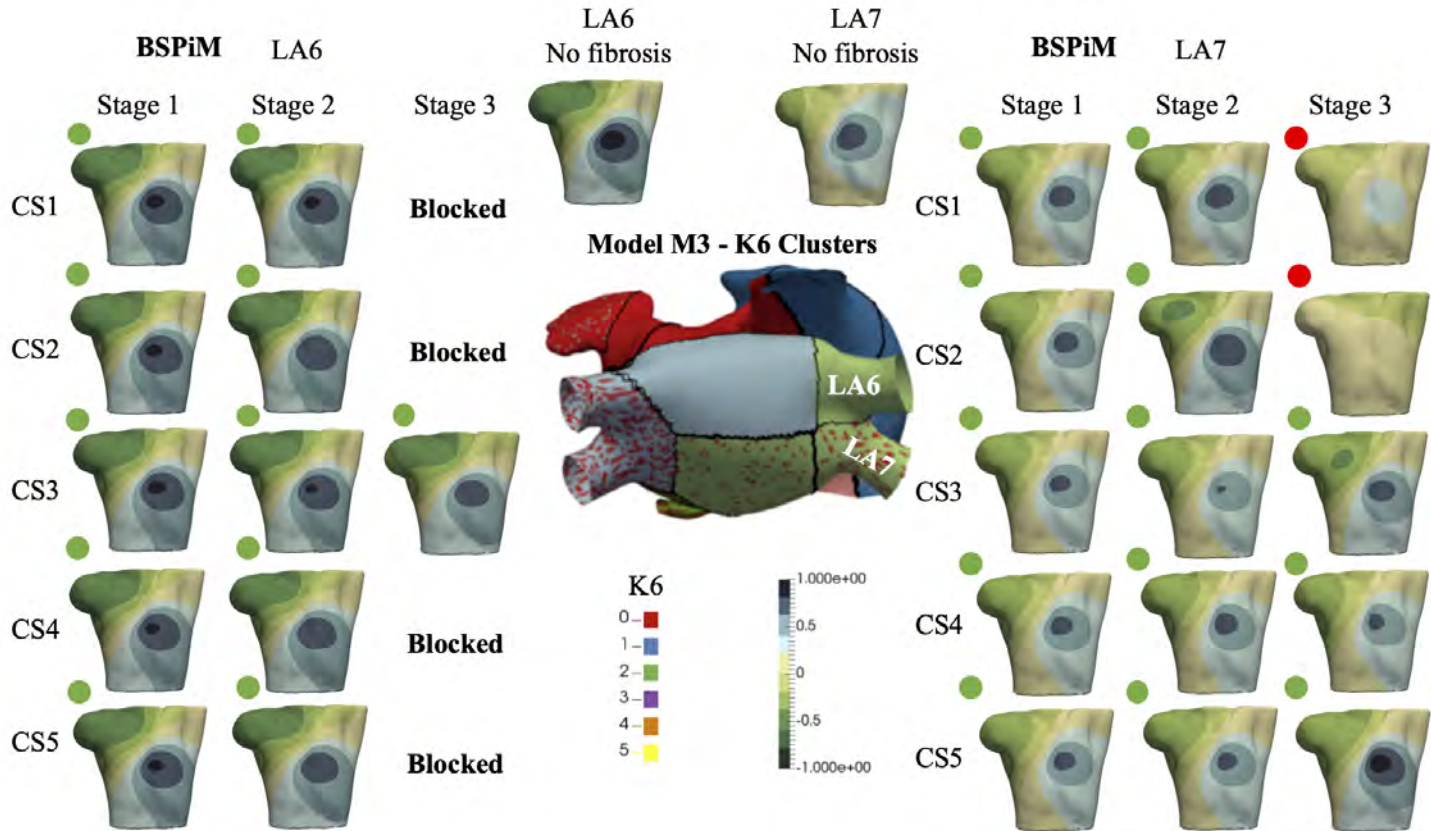
Figure 5.6: BSPiMs for CS1-5, and ectopic locations LA6 and LA7. The color disc indicated the class assigned to each BSPiM.

5.3.5 Classification of Atrial Ectopic Focus

After the analysis of the persistence and geometrical consistence of the clustering process, we performed a classification of the ectopic foci, according to the step 5 of our pipeline. The Figure 5.7 gives an example of the calculation of the accuracy for the model M0, no-fibrosis, and the extreme case of the model M5 that includes all the stages of fibrosis. The values obtained came from the cross-validation process which averages the accuracy obtained for each fold and summarizes the result. We used 4- folds to split and stratify homogeneously the training set and the test set.We have also included in the plot a dotted line (accuracy = 0.90) that is the minimum level of accuracy that we considered necessary to use the model in a clinical environment.

Classification of Non-fibrotic Cases

Table 5.2 shows the measured classification accuracy (CA) for 256 features for the model M0 (i.e., no-fibrosis) and for K = 2 to K = 10. The results show that for this case of no-fibrosis we obtained an accuracy CA ¿ 0.90 for K = 2 to K = 8, and a minimum accuracy CA = 0.85 for K = 10. Figure 5.7A, shows the complete accuracy obtained by the classification of the model M0 for features or electrodes from 2 to 256. In the cases K = 2 to K = 8 we recorded an accuracy of CA ¿ 0.90 even with only 64 features or electrodes, and for K = 10 the accuracy was entirely below the dotted line of CA = 0.90. Inset Figure 5.7A, shows a torso with an example of the optimal electrode locations selected from the 256-electrode BSPiM to perform the ectopic foci classification in groups. For example, yellow spheres correspond to the best set of 2 electrodes, whereas yellow together with green spheres correspond to the best set of 4 electrodes. Larger sets of optimal electrodes always contained smaller sets. There were no intersecting classes, and all the ectopic groups were associated to different regions.

Classification of Fibrotic Cases

We introduced incrementally in the training phase for classification those fibrotic cases from model M1 to model M5 (i.e., data from all FAT simulations, and all configurations of fibrosis). Table 5.2, shows the measured CA for the models M1 to M5 for K = 2 to K = 10 and 256 features, where the
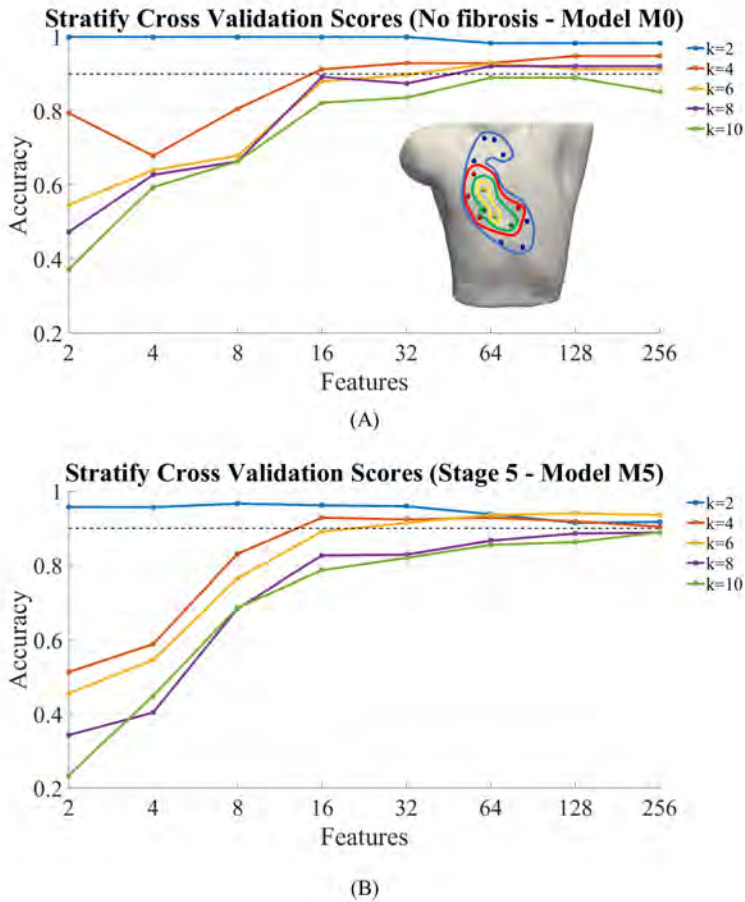
Figure 5.7: Classification of ectopic foci. (A) Accuracy of classification for the model M0, no fibrosis; (B) Accuracy of classification for the model M5, extreme case of fibrosis (i.e., from Stage1 to Stage 5). In both cases, the graphs were performed for different number of ectopic clusters (from K = 2 to K = 10), and different number N of features used (i.e., 2, 4, 8, 16, 32, 64, 128, and 256). Inset panel (A), example of optimal selected features (electrodes) for: 2 (yellow), 4 (+green), 8 (+red), 16 (+blue) features.

values of accuracy remained almost all above CA ¿ 0.90 for all the models with slight variations, except for model M3 and K = 4, that showed a minimum of CA = 0.84.

Figure 5.7B shows the complete accuracy obtained for the extreme case of M5 (i.e., Stage 5 of fibrosis). We see, in this case, from K = 2 to K = 6 that we need a minimum of 16 features to obtain an accuracy CA = 0.90, and a maximum of CA = 0.93 with 256 features for K = 6. From K = 8 to K = 10 the values of accuracy are below the dotted line of 0.90, obtaining values of CA = 0.8 for both, K = 8 and K = 10.

5.4 Discussion

Computational modeling of the human atria has changed during the last 15 years, evolving from very simple structures to very detailed models including atrial wall and fiber directions [167]. Several models exist today that include structures of intracellular compartments and atrial heterogeneity, and furthermore they include pathological structures, modeling atrial remodeling and fibrotic tissue. MacLeod et al. [168] emphasized the importance of including information about structural changes of the atrial myocardium into geometrical models. Previous results from [111] suggest that FATs have a particular electrical pattern on the torso [169, 170, 171], and that those patterns have a singular P wave morphology in specific locations providing a potential way to predict the origin of FATs. They developed a decision tree algorithm based on the P-wave morphology in specific surface ECG leads to provide some help in the search for ectopic foci sources to allow for the identification of the origin of the tachycardia. Therefore, using only the P wave morphology, they prospectively evaluated the algorithm with a number of patients, finding a predictive accuracy of 93% for a few focal trigger locations that could be distinguishable.

Other biomarkers such as P-wave integral maps [133] have been recommended to summarize different atrial activation sequences and relate them to ectopic foci. In the ventricles, other complex techniques such as electrocardiographic imaging (ECGi), have been widely studied in the last few decades to directly compute the cardiac action potentials by solving an ill-posed inverse problem [2, 172].

However, many of those approaches use a priori information to improve their results, such as constraints in spatial and temporal domains, physiological

knowledge about the activation sequence or localization of activation onset. In addition, those methods need a segmentation of the atria and torso models from an image sequence stack, and the construction of a finite element model to simulate cardiac electrophysiology. All those requirements, which are very time consuming, hamper the use of those tools in clinical environments. In our previous work [100], we used machine learning techniques to spatially cluster and classify ectopic atrial foci into clearly differentiated atrial regions by using the body surface P-wave integral map (BSPiM) as a biomarker. Ectopic foci with similar BSPiM naturally clustered into differentiated, non-intersected atrial regions and new patterns could be correctly classified with an accuracy of 97% when considering 2 clusters and 96% for 4 clusters ([100]. However, we only considered non-fibrotic cases, which are not very common cases clinically.

To learn this association, (i.e., ectopic location-BSPiM), regression techniques could appear to be a reasonable approach. However, as the total number of ectopic locations is reduced (i.e., 57 = 19 with fibrosis + 38 without fibrosis), there are not enough ectopic locations to apply regression techniques.

In this multi-scale biophysical 3D model simulation study, we used machine learning techniques to focus also on the localization of the arrhythmogenic electrical drivers (i.e., ectopic foci), that contribute to the generation of focal atrial tachycardia (FAT) with regional LA patchy fibrosis as a variable of structural remodeling according to the Utah classification scale [98]. This study introduces a new methodology which improves previous results and obtains an accuracy above 90% for classifying ectopics into 6 different atrial regions (i.e., from K = 2 to K = 6). In addition, we reduced the dimensionality of the BSPiM patterns and included noise to obtain data similar to that acquired in a clinical environment. It is important to remark that our simulated P-waves do not include QRS complex and are not affected by baseline wandering. In a real scenario, it will be fundamental to use filters such as bidirectional high-pass Butterworth filter to correct baseline wandering, or Template Matching Subtraction to eliminate the QRS complex. Feature selection analysis was used to find the minimum number of electrodes required to predict, with high accuracy, the location of ectopic foci during FAT. For cases without fibrosis, we could obtain predictions (dividing the atria in K = 4 regions) with an accuracy of 0.90 with only 16 features or electrodes placed on the torso front. When detection considered more and smaller regions (from K = 6 to K = 10), the accuracy was reduced to a minimum accuracy of 0.81 for K = 10, and a maximum of 256

electrodes.

As soon as LA patchy fibrosis comes into play, (i.e., Stage 1 to Stage 5), together with an increase in the number of regions analyzed, (i.e., K = 2 to K = 10), the measure of overlapped regions ratio increases, confirming that overlapping, and the ratio of well formed clusters, or convexity, decreases, demonstrating the presence of ectopics disconnected or isolated from their group. However, the classification accuracy, remained above the value of 0.90 for numbers electrodes ranging from 128 to 256, even for the most extreme case, which is the model M5. The high accuracy was obtained because we allowed the clusters of patches to be disconnected. Therefore, if the model predicts that a given BSPiM relates to class n, the patches that form the class could belong to more than one single atrial region. From a clinical point of view, the location of the atrial trigger will not be so efficient since the area of search increases, but still the method improves current clinical practice. A positive point is that in cases in which a given atrial patch has more than one label, the main patches associated with the label are in general neighbors. That means that patches in the borders of two regions sometimes are classified as label "a" and sometimes a neighboring region "b."

5.5   Conclusions

The methodology presented here could be useful to help an electrophysiologist to reduce the search area of an ectopic focus non-invasively and plan the intervention a priori. The pipeline presented can produce results in real time, since all the simulations and the training phase are performed offline and a priori. The effect of fibrosis on the atrial activation and BSPiM is large when stage 3 (¿15% fibrosis) is used. The machine learning system obtains high accuracy at the expense of increasing the size of the region where the ectopic focus is located. The most complex locations determined in our simulation study were in certain pulmonary veins when the stages of fibrosis were 3, 4, or 5. However, patients that show a stage of fibrosis higher than 3 are not recommended for treatment.

6

Validation of the machine learning pipeline. A case study.

Abstract

This chapter summarizes the clinical validation of the full pipeline on an exemplary clinical case carried out at the electrophysiology laboratory (EP-lab) at the "Hospital La Fe" in Valencia. We have designed a clinical protocol based on pace-mapping to acquire a collection of BSPMs from a patient together with the pacing locations. We locate the position of the BSPM electrodes using a 3D camera installed in the EP-lab. We automatically process the P-wave signals from the multi-electrode system to obtain BSPiM. Finally, we assess the accuracy of the system trained with simulation, in predicting several sites of origin for the FAT from a reduced set of electrodes.

6.1   Introduction

The combination of computer simulations, which can integrate patho phys-
iological data to create detailed models of arrhythmogenic substrates, and
machine learning technologies is expected to solidify the understanding
of ablation mechanisms and to provide theoretical arguments supporting
substrate-specific ablation strategies [173].

The final goal of such hybrid model is to aid in therapy planning and opti-
mization of ablation of atrial arrhythmias triggered by non-pulmonary vein
triggers, for instance in the left posterior wall and near the venae cavae
[174, 175]. A step wise ablation strategy may include successively eliminat-
ing these focal sources, which has been already applied to paroxysmal AF
patients [176].

Computer models can be used to determine what the outcome would be
if the ablation strategy was perfectly executed, reinforcing the need for
improved signal processing tools for ectopic focus detection. The use of
patient-specific models, although promising, are still based on the use of
high performance computing. On the contrary, machine learning tools can
be easily integrated and executed in real time in clinical environments.

The clinical case study presented in this chapter illustrates a major ad-
vantage of machine learning, where the integration of simulated patho-
physiological data in the training set, could help to consider different sce-
narios.

6.2   Material and Methods

6.2.1   Clinical Data Acquisition

Data from a single patient was acquired from the electrophysiology labo-
ratory (EP-lab) at the Hospital Universitario y Politecnico la Fe de Va-
lencia, with a favorable outcome report from "La Fe" Health Department
Ethics Committee for biomedical research, responsible for ensuring medical
experimentation and human subject research in accordance with national
and international law. The data corresponds to a male, that suffered from
paroxysmal atrial fibrillation (PAF), and was candidate for RFA to stop it.
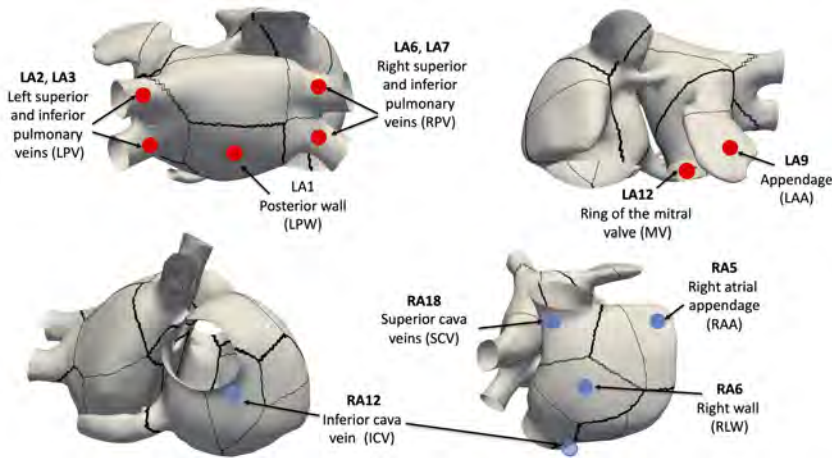
Figure 6.1: Location where patient was paced from a catheter, to emulate ectopic locations.

During the RFA, a custom tailor-made multi-electrode system was used to acquire the surface ECG from 40 locations on the patient torso. The multi-electrode set was connected to the EP room polygraph together with the intra-cavitary catheter electrodes and the surface precordial leads, so that all the signals where temporally synchronized.

Before the RFA was performed, the electrophysiologist mapped and reconstructed in 3D the atria using electro-anatomical mapping system CARTO 3 (Biosense Webster) and the Confidense high-density mapping module. Following, with the patient in sinus rhythm, a pace-mapping protocol was carried out to stimulate the atria with a BCL=500ms (to override natural SAN pacing) from 11 locations (4 RA and 7 LA) (see Figure 6.1) with a stimulation catheter. During the protocol, surface electrodes were acquiring data and associating it to the intra-cavitary pacing locations. The EAM system provided a reconstruction of the atria, and permitted to accurately locate the position of the catheter while the pace-mapping protocol was carried out. However, the LA mesh model was not transferred from the hospital, and was deleted few days after the acquisition. Nonetheless, the RA model could be obtained and was reconstructed, together with the position of the stimulation points, which allowed to compare them with the simulated scenarios. Figure 6.2) shows the EAM of the RA from two views, where the left panel corresponds to Fig. 6.1 bottom-right in the model. The MRI of the patient was not acquired and therefore, we had to rely on the EAM anatomy.
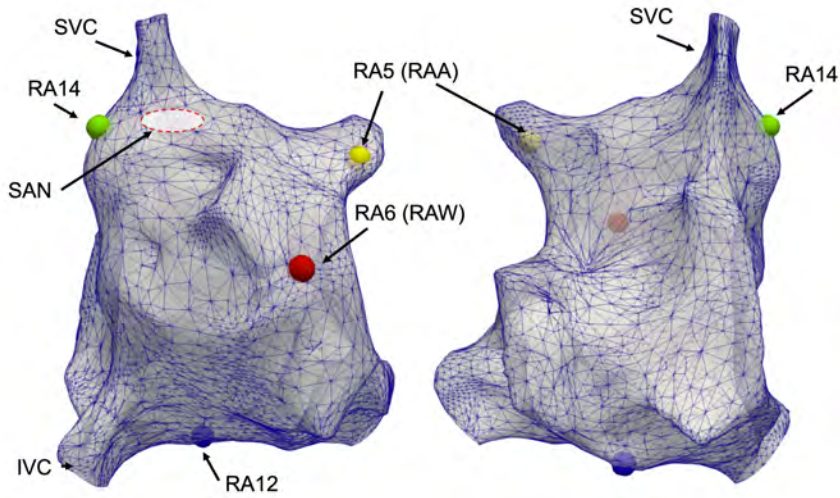
Figure 6.2: EAM reconstructed for the patient RA from two views. Color spheres indicate the location of the patient catheter for each of the four simulated ectopic focus. SCV stands for superior cava vein, and ICV, inferior cava vein.
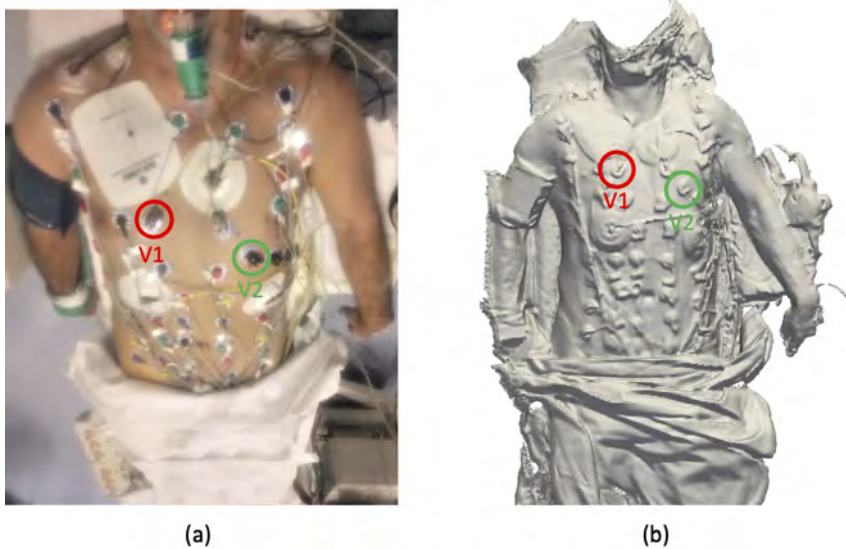
Figure 6.3: Image acquisition with 2D and 3D cameras of the patient laying doing in the EP-Room bed. Electrodes are already placed on the patient chest. Leads V1 and V2 are highlighted in both views.

The location of the surface electrodes is very relevant to compare data with the simulation pipeline developed in Chapters 4 and 5. Therefore, we captured the location of the electrodes on the patient's chest by using a 3D camera based on Kinect hardware, and generated a torso surface with high resolution that allowed us to identify all the electrodes. Figure 6.3 (a) shows a 2D picture of the patient's torso acquired with a conventional camera where it is visible the location of each color-coded electrode. Figure 6.3 (b) shows the same scene (acquired from a slightly different angle) acquired from the 3D camera and reconstructed as a surface triangular mesh, where it can be clearly appreciable the location of each node (the location of precordial leads V1 and V2 are highlighted in both views). Note that the EAM navigation system required the placement of several large patches and electrodes that prevented to locate our electrodes in some regions. One of the advantages of this methodology is that we do not need to irradiate the patient using a CT scan to determine the location of the electrodes.

6.2.2 Torso Registration

Since we need to compare the data generated with the simulations described in Chapter 4, and validate the pipeline developed in chapter 5, we have to identify the exact location of the torso electrodes with respect to the biophysical 3D atria-torso model. Therefore, we carried out a rigid registration between the computational mesh and the mesh obtained in the EP-room with the 3D camera.

Taking advantage of anatomical landmarks, which were the shoulders of the patient and the model, together with the ribs (model), we obtained a good initial alignment. Using an iterative closest point algorithm (ICP), we obtained the transformation which was subsequently applied using Paraview software. We finally refined the alignment manually to adjust it perfectly. Figure 6.4 shows the 3D patient acquired model (blue), with the biophysical torso mesh model (white mesh) overlapped. Details on the right of the figure show the fit from both sides of the torso, including the location of the ribs (yellow) and the heart. The match between models was very good, although the biophysical model does not include the abdomen (lower region), and hence some of the electrodes placed on the patient had to be discarded.

Once both models were registered, the location of the 40 patient electrodes was determined on the computational high resolution biophysical model of 14,157 nodes. In addition, the patch or region of the torso, as described in
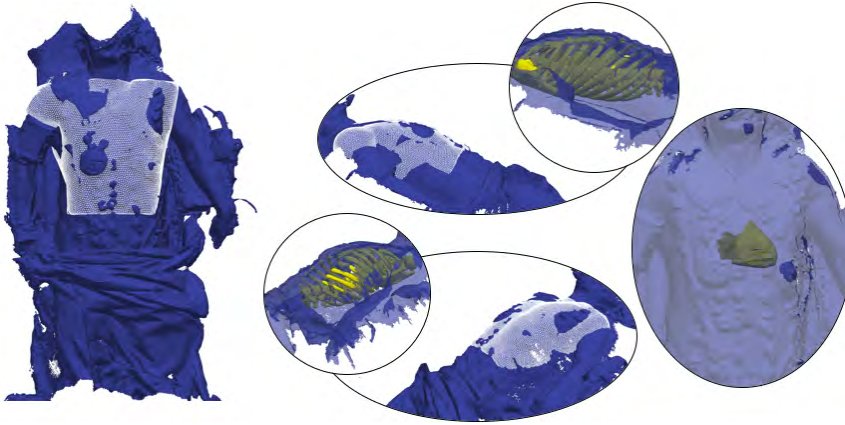
Figure 6.4: Rigid registration of acquired mesh to 3D torso model. Several views of the torso model can be observed, where after merging the meshes the torso surface mesh, the ribs and the heart are placed on the patient acquired mesh.

Chapter 5, was determined in order to be able to classify each of the atrial activation sequence generated with the pace-mapping protocol.

Figure 6.5 (a) and (b) show the patient together with the 3D reconstruction of the kinect camera, where the electrodes have been detected. We used Paraview software to determine the location of each electrode, which could be observed by a heap in the 3D model. After identifying the electrode locations, we labeled them and searched the corresponding nearest neighbor in the computational torso model (Figure 6.5 (c)). As can be observed some of the patient electrodes fall outside the computational model and had to be discarded (red numbers). In addition, electrodes 38 to 40 where outside the field of view of the 3D camera and their position could not be determined. In total, we obtained signals from 28 electrodes on the torso surface (not taking into account the precordial leads).

6.2.3 Signal Data Processing

We obtained from the polygraph a bulk data file that contained the 40 different signals from the beginning to the end of the intervention, which included several hours of recordings. This raw data consisted of a N = 6,126,672 points with a sampling frequency of fs = 1 KHz. However, we selected only the period where the pace-mapping was carried out, and split it

Figure 6.5: Detection of electrode locations, and labeling in the patient torso and the computational model. (a) Patient picture with electrodes placed, (b) 3D patient model with electrode position detected and labeled, (c) computational 3D fitted model with electrode positions. Labels in red contour disk correspond to the precordial leads. Red numbers correspond to labels that fall outside the computational torso and have to be discarded.

in temporal sections corresponding to each location paced from the catheter by the electrophysiologist.

Figure 6.6 (a) shows the raw signal (voltage over time) acquired at electrode 18 (see Figure 6.5 (c), near lead V1) while pacing at location RA5 (see Figure 6.1, Right atria appendage (RAA) region). Thanks to the increased heart rate, we could determined for each ectopic the beginning and the end of the catheter stimulated period.

The raw signals for each stimulated location were processed to obtain clean P-waves as follows. We eliminated the base line wondering using a bidirectional Butterworth high-pass filter with cut-off frequency of 0.5 Hz [177, 178]. We used a zero-phase forward and reverse digital IIR filter. The Zerophase filtering helps preserve features in a filtered time waveform exactly where they occur in the unfiltered signal. After filtering in the forward direction, the filtered sequence reverses and ran back through the filter; the output is the second filtering operation. The resulted signal has zero phase distortion, and a magnitude modified by the square of the filter magnitude response [179].

The high-frequency noise elimination was carried out with an IIR bidirectional Chebyshev low-pass filter with: i) a cut off frequency of 45 Hz, ii)
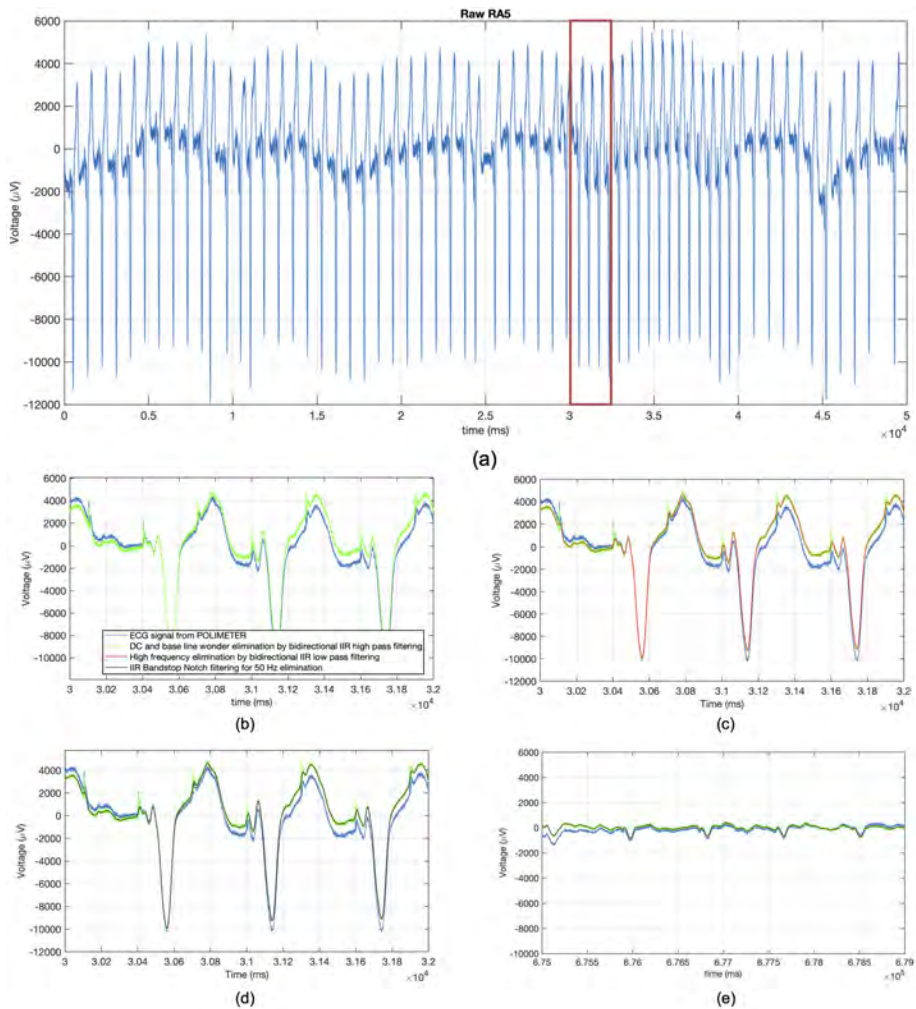
Figure 6.6: Output of all filters overlapped. (a) Raw signal obtained in electrode 18 while stimulating from RA5 (Right atrial appendage), (b) Overlapped on the raw signal the output of the high-pass filter for DC and base line wondering elimination. (c) Shows the output of the low-pass filter for high frequency interference elimination (red line). (d) Output of the notch filter for mains interference elimination (black line) and final output of all filter stages. (e) signals obtained from electrode 15, when stimulating at location RA12.

129

less than 3dB of ripple in the pass-band from 0 to 45 Hz, and iii) at least 60 dB of attenuation in the stop-band [177, 178]. We also implemented a zero-phase distortion filter [179].

The mains interference was treated using a band-stop notch filter for the fixed frequency of 50 Hz elimination. A notch filter is a band-stop filter with a narrow bandwidth (high quality factor). It rejects a narrow frequency band and preserves the rest of the spectrum mostly unchanged [163].

Figure 6.6 shows the output of each filter stage overlapped to the raw signal from the polimeter, where (b) is the output of the high pass filter for the DC and base line wondering elimination (green line) (c) is the output after applying the low-pass filter (red line) and (d) is the notch filter for mains interference elimination (black line) and also the final output of the filter bank.

The separation of the auricular activity (AA) from the ventricular activity was carried out using a Template Matching Subtraction (TMS). The TMS method is based on the cancellation of each QRS complex + T through the subtraction of an average QRS complex + T computed over the recording under analysis [180] [181].

Figure 6.7 shows the extraction process of VA, where (a) is the filtered ECG after the filter bank, (b) shows the detection of the R wave [182, 183], (c) shows the extracted QRS complex +T complexes after applying the generated template (d) from a window of 60 complexes.

The average QRS complex + T is aligned to each R wave of the ECG and subtracted, obtaining at the end a residual signal containing the AA for each analyzed derivation (see Figure 6.8 (a), filtered ECG (blue line) and the overlapped AA (red line)). After the subtraction, the signal was Band-Pass filtered in the band of 3 – 12 Hz [163].

From the filtered signal, we selected manually a P-wave within the stimulated period for each ectopic (see Figure 6.8 (b), vertical dashed lines) to determine the activation time of the P-waves of the ectopic for the 40 electrodes (i.e., [activation time x 40 channels] in milliseconds). As a result, for each atrial location paced, we summarized the P-wave signals on the torso surface into a BSPiM. The BSPiMs were all globally normalized (considering all the BSPiMs) within the range (-1, 1).
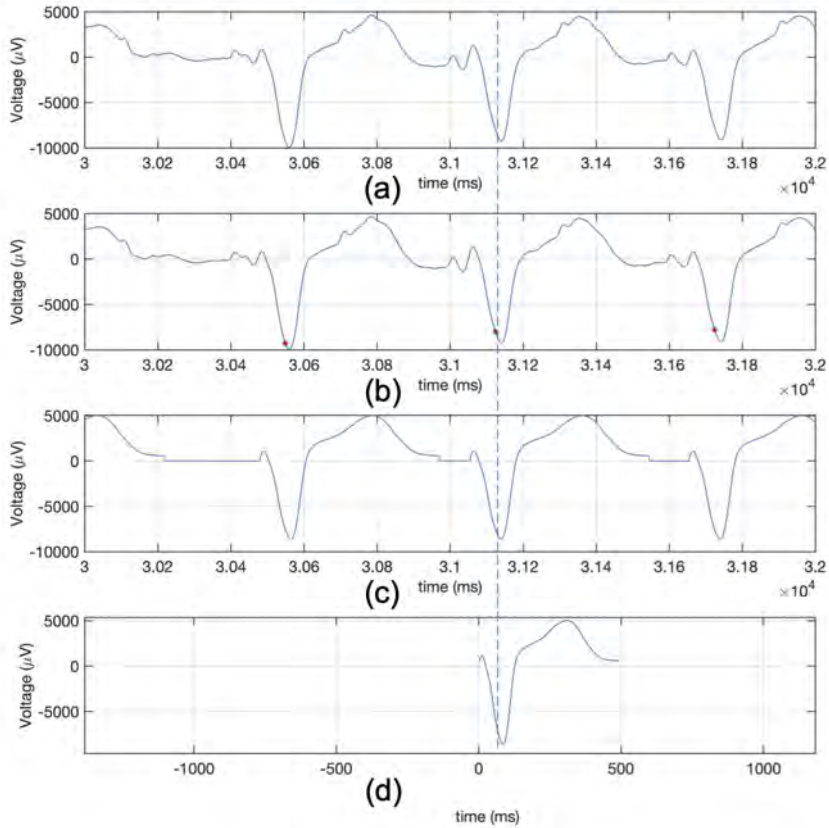
Figure 6.7: ECG Template extraction. (a) Filtered ECG signal, (b) Detection of the R wave (red asterisks), (c) Chain of extracted QRS complexes + T wave, (d) Template of 60 QRS complexes + T window
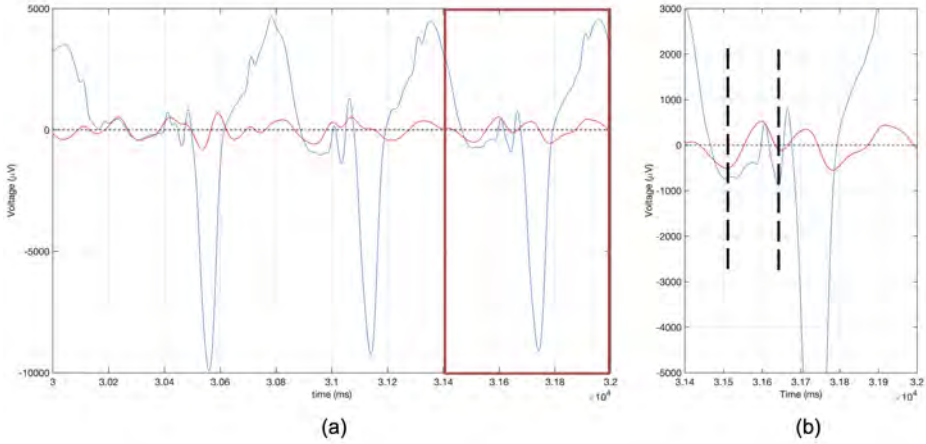
Figure 6.8: P wave activation period. (a) Overlapped filtered ECG (blue line) and obtained AA (red line), (b) Selected P-wave within the stimulated period (vertical dashed lines)

6.3 Results

The electrical signals acquired for the the 11 stimulated location were processed as describe in previous sections. However, two of them, RA12 and LA2, show very low-amplitude electrocardiograms for reason that we could not determine. Figure 6.6 (e) show the signals corresponding to electrode 15 in RA12, where due to the low amplitudes, after processing the signal, we could not distinguish the P-wave. Therefore, after discarding those cases, the final dataset consisted of 9 BSPiM (stimulated locations) with 28 samples each.

To calculate the classification accuracy of our method in the patient, first we need to adjust the simulated dataset. Our simulated data consisted on BSPiMs sampled at either 14,157 or 256 locations, covering the whole front and torso back, however the patient data only included 28 front torso electrodes. Therefore, we performed a dimensionality reduction, by selecting from the full high-resolution BSPiM (HR-BSPiM) the 28 electrodes recorded in the patient, and generated new reduced low-resolution BSPiM (LR-BSPiM) for each simulated ectopic focus.

In order to visualize the resulting pattern, we carried out an interpolation of the data on the torso mesh using a custom-code based on the VTK
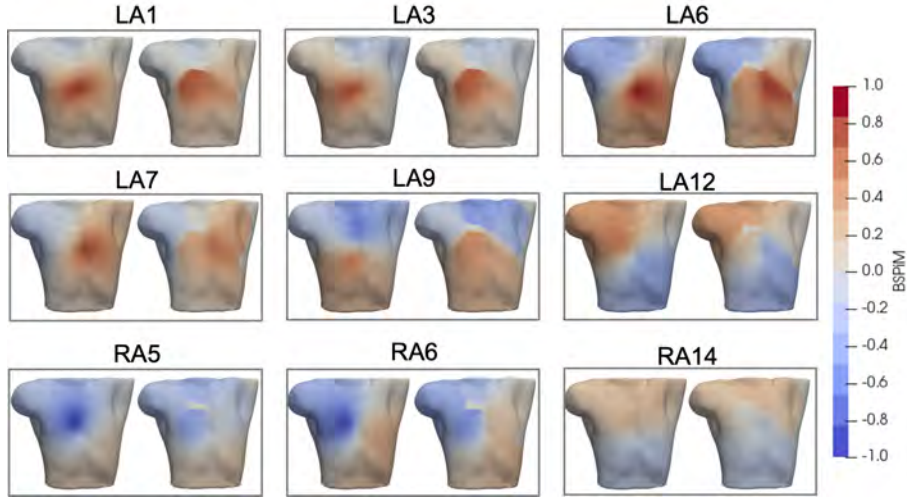
Figure 6.9: Change on the BSPiM due to a reduction in the number of electrodes. In each subfigure the left image corresponds to a BSPiM with 14157 electrodes, whereas the right image corresponds to the 28 electrodes used in the patient.

library. Figure 6.9 shows the BSPiM for the nine different stimulated locations, where left subfigures correspond to simulated HR-BSPiMs, and right subfigures to simulated-interpolated LR-BSPiMs. The original HR-BSPiM was normalized in the range [-1, 1] and the down-sampled versions kept the original values, i.e, we did not normalize again considering only the 28 electrodes. One of the most clear effects due to the poor sampling density is that the maximum and minimum values in the HR-BSPiM are usually smooth and displaced in the LR-BSPiM. The central area of the torso, which had the lowest density of electrodes due to the placement of other large patches of the EAM system, had a negative effect on the BSPiM accuracy. However, the main pattern and polarity is kept and therefore the LR-BSPiM are still informative, and can allow the differentiation of the activation origin.

Next, we compared the simulated LR-BSPiM with the patient BSPiM (P-BSPiM). Figure 6.10 shows a visual comparison for the nine stimulated locations, where differences can be appreciated in some cases. The main polarity in the pattern, positive (redish) and negative (bluish), was similar in both patient and simulated data, but in LA12, where the pattern was inverted. The polarity pattern in the patient was also in agreement with recordings from other clinical studies [133] (see Fig. 6.10, detail between torso models). Since LA12 lies very close to the coronary sinus (CS), the
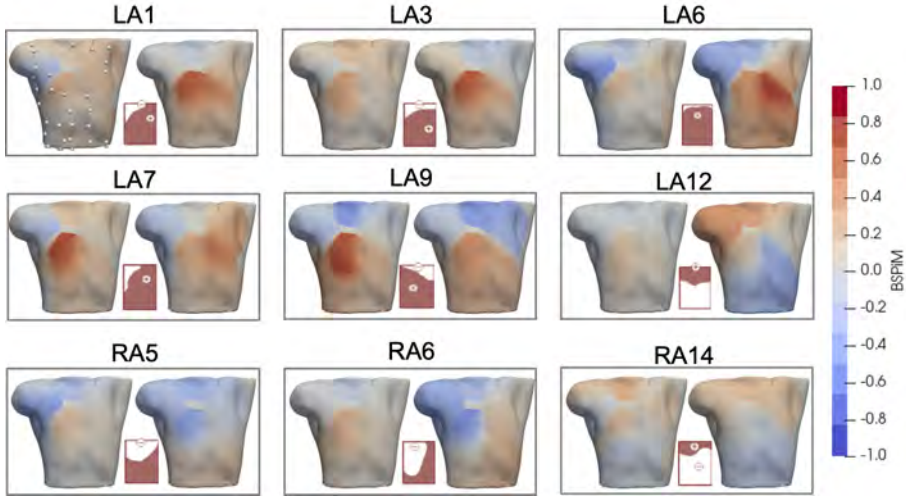
Figure 6.10: Visual comparison of the nine patient BSPiM (left subfigures) and the corresponding simulated ones (right subfigures). Squared subfigures in the middle are the BSPiM clinically measured for a set of patients in [133]. Subfigure LA1 left shows the location of the electrodes.

stimulus could cross to the RA throughout the CS pathway. However, we already observed in a simulation study [184] that ectopics foci in this location invert when there is a conduction block throughout the CS, often due to the presence of fibrosis. This effect was also observed in our study, as can be appreciated in Figure A.6 CASE 1, LA10 (Appendix) where the pattern rotates form Stage 1 to stage 5.

We analyzed the clusterization of simulated ectopic foci on the atria (patches) when using only 28 electrodes, to compare with our previous model with 256 electrodes. We used a K-means clustering with K ranging from 2 to 6 groups on the LR-BSPiM. As a result, each LR-BSPiM was assigned to a group, which was subsequently projected to the atria space. Figure 6.11 shows the label, i.e. group, that each atria patch was given for K=6 using a color-coded representation. The equivalent patch division from 256 electrodes and K=6 can be seen in Figure 5.3. The labels assigned to the atria patches in M1 model are mostly preserved when we use the LR-BSPiM data, and some differences are appreciated for M3.

When we included the patient P-BSPiMs into the M1-M3 group to analyze how they cluster into groups, we obtained that most of them tend to cluster in the same group, independently of the ectopic location. That means that

134

all of them share a certain property that makes them similar among them and different to the simulated data, which is probably related to the P-wave amplitudes. Although both the simulated data and the patient data are globally normalized between [-1,1], we still consider in the normalization a different amount of BSPiMs in the training set (95 simulated BSPiMs in M1) and the test set (9 patient BSPiMs).

We trained a SVM using the simulated data (M0, M1, M2 and M3) and the labels obtained from the Knn, and used the patient data as a test set to check the classification accuracy. Figure 6.12 shows the atria with the patches colored as a function of the cluster groups using models M0, M1 and M2, together with the location of the 9 patches stimulated in the patient model. The color of the patient stimulated patch corresponds to the output of the classifier, e.g. for M0-LA1P is correctly colored (classified) in light green, and as can be seen by the line connector it belongs to the light green region, however, for M0-LA3P, the classifier puts it into the dark blue group, while it is part of the light green one. In summary, for M0 5 locations are properly predicted (LA1P, LA6P, LA7P, RA5P, LA9P), three of them are incorrectly predicted (LA3P, RA6P, RA18P), and one of them corresponding to the neighboring region (LA12P).

Since we do not have information about the level and distribution of fibrosis in the patient, we classified the 9 ectopic focus using the 3 different models to analyze the number of hits. In this particular patient, we correctly classified 5 ectopics foci for model M0, 3 ectopic foci for model M1, and 2 ectopic foci for model M2. Therefore, model M0 was the most accurate in terms of classification.

6.4 Discussion

The use of non-invasive electrical recordings to plan RFA interventions is becoming feasible in clinical environments. Several multi-electrode devices in the market are offering the possibility to detect the source of arrhythmia before the RFA, so that operation times can be reduced and the therapy can be optimized in complex cases. Most of the systems rely on the solution of the inverse problem in electrophysiology, using a technology called electrocardiographic imaging (ECGI). Those systems have been tested mostly in the ventricles due to the stronger signals, and have started to be applied now to atrial arrhythmia [125, 126].
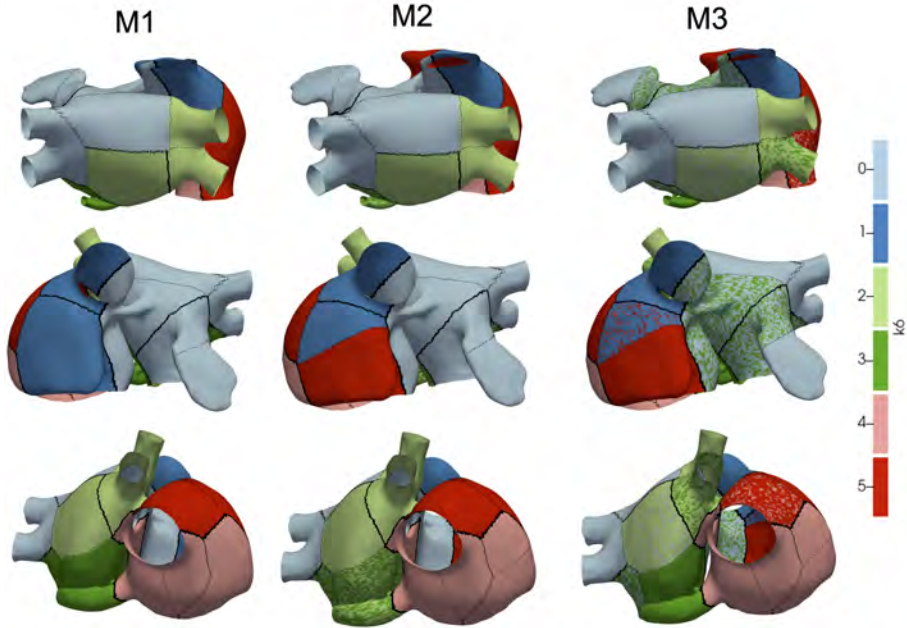
Figure 6.11: Clustering of LR-BSPiM using K-means with 6 groups, and projected to the atria space. Each color indicates the group to which the particular ectopic focus is assigned. Figure 4.4 shows the labels corresponding to each atrial patch. Results are shown for three different levels of fibrosis M1-M3.

In this sense, we present an alternative method, that also uses a custom-made multi-electrode system, with a novel method to determine the origin of the atrial arrhythmia based on machine learning pipeline trained only with biophysical simulations. However, we face several common challenges in order to process the patient data that has to be compared with our trained models. First, we have to analyze and characterize automatically atrial activity (AA) from electrocardiograms (ECG) recordings, regardless of the leads being used, which requires the extraction or cancellation of the signal components associated with ventricular activity (VA), that is, the QRS complex and the T wave (QRS-T). Since we are using electrodes in areas remote to the atria, AA presents in the ECG lower amplitude appearing in some cases well under the noise level, this amplitude is much lower than the ventricular equivalent. In addition, both events possess spectral distributions that especially overlap, making linear filtering solutions ineffective. In order to cancel out VA in the ECG, we choose to suppress the QRS complex and T wave through the subtraction of a fixed template being
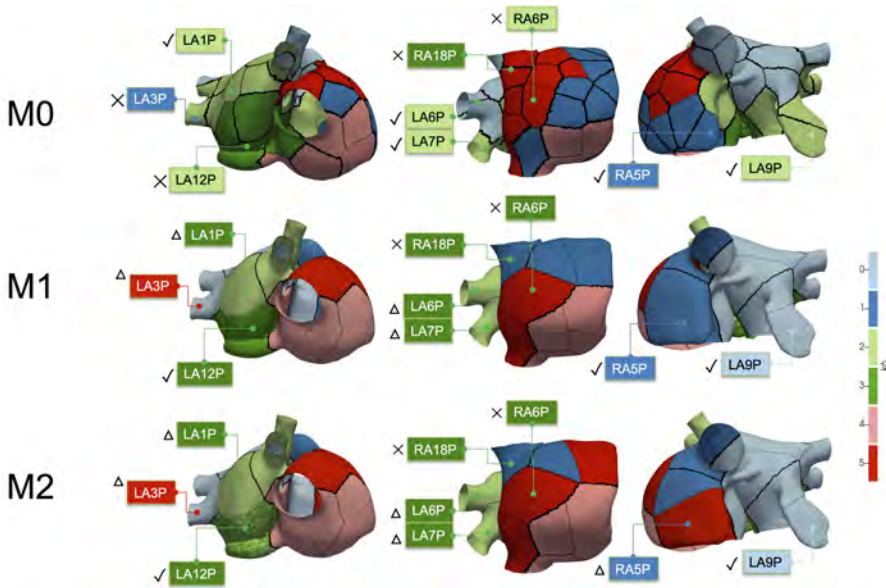
Figure 6.12: Classification of patient ectopic foci into atrial regions. Labels indicate the origin of each ectopic focus (connected with a line to the patch), and their color indicate the region in which they were classified.

called Template Matching Subtraction (TMS) [181, 180]. Other studies in the literature used an adaptive template in conjunction with the correct spatial-temporal alignment of every QRS complex [185]. More recent methods have focused on extracting the VA using artificial neural networks and subtracting it from the ECG [186], or on the decomposition of the original ECG in a set of coefficients that obtain the AA using discrete packet wavelet transform [187].

After extracting the P-wave, we have to accurately determine the start and end time points, which are crucial to calculate the BSPiM. Changes in the P-wave morphology, the P-wave line wondering or the definition of the P-wave time period would affect the BSPiM and could prevent the correct classification of an ectopic focus.

It is important to remark that in this study, we only made use of 28 frontal electrodes, that were not homogeneously distributed, which makes it more difficult to determine the BSPiM patters. We solved the problem of finding the location of the electrodes on the torso patient using a novel techniques based on a 3D camera, which allowed us to virtually place them anywhere in the torso. In addition, we avoid the need of a CT, which turns out in

less radiation for the patient, and a simple clinical management.

Our results for a single patient show a good visual agreement between most of the BSPiM and the simulated cases with some exceptions, for the ectopic foci arising from the mitral ring close to the attachments of the coronary sinus. We already reported in another study [184] that the connections between atria through the coronary sinus are not always functional, and therefore the BSPiM patterns for ectopic foci in this area might be inverted. However, since the patterns are inverted, the learning system would be confused if we assign the same label to both of them, and we chose to keep only the version where CS conducts.

Finally, in the future it will be necessary to collect more patients using the same methodology, and making sure that the computational model can include all the electrodes placed on the patient to increase the amount of information available. It would be also interesting to carry out a sensitivity study on some input parameters, such as the start and end of the P-wave.

6.5   Conclusions

This study of our machine learning system on one patient is the first step towards a larger validation of an automatic system for non-invasive detection of FAT origin. The system could identify, on a reduced number of cases, the origin of the FAT. A larger database of simulations together with an increase number of patient data will be necessary in the future to obtain the real accuracy of the system. The pipeline presented can be fully automatized and run in real time in a EP Lab in a hospital with a minimal additional equipment.

7

Conclusions and Future Work

7.1 Summary

Tachycardia derives from abnormal impulses triggered in the heart that result in fast rhythms, above 100 beats per minute, which can range from 140 - 200 beats per minute. Atrial tachycardias, excluding atrial flutter, are thought to represent about 5% to 15% of sustained supraventricular tachycardias in the adult. When the source of the tachycardia is an ectopic focus, e.g. focal atrial tachycardia (FAT), the electrical impulse comes from an abnormal pacemaker rather than the SAN, changing the normal activation sequence since it can be located at any point in the atria [30]. FATs are characterised by radial, circular, or centrifugal spread of activation from a single focus or point source and the activation is shorter than the flutter case (i.e., it is a short activation; there is no activation spanning the whole tachycardia CL) [31]. FAT often originates from well-characterized sites within the left and right atrium such as the tricuspid annulus, crista terminalis, pulmonary veins, ostium of the coronary sinus, and mitral annulus [32, 33, 34, 35, 36], however they can be found virtually in any region of the atria, which makes their treatment difficult. FAT is commonly treated by RFA with a high long-term success rate. The catheter ablation treatment targets the arrhythmogenic electrical drivers and terminates them by localized energy delivery. The end point of catheter based ablation is to eliminate the triggers with the least amount of ablation necessary [110].

Experimental studies have provided convincing evidence that fibrotic transformation of atrial myocardium results in deterioration of atrial conduction, increasing anisotropy of impulse propagation and building of boundaries that promote re-entry in the atrial walls that maybe directly relevant for the mechanisms responsible for maintaining atrial arrhythmias [20]. Myofibroblast are non-excitable tissue, but it has been shown that they can interact electrically with surrounding myocytes, affecting their normal function [18, 19]. Experimental and numerical studies have shown that the texture and spatial distribution of fibrosis may play an important role in arrhythmia onset.

Over the last years, new medical imaging technologies have allowed obtaining clinical information with a high level of detail, and specific to each patient. In this context, a huge amount of information has been generated in recent years at different levels: sub-cellular, cellular, tissue, organs and systems [37]. In addition, there are mathematical models to simulate ventricular myocytes, atrial myocytes, specialized conducting tissues such as

Purkinje cells or fibroblast. Most of the models have also been adapted to take into account the electrophysiological heterogeneity present in real tissues. Among the most used detailed models to simulate human atrial myocytes we can highlight, the Courtemanche-Ramirez-Nattel (CRN) ionic model [59], the Maleckar et al. ionic model [60], the Nygren et al. ionic model [61], the Koivumaki et al. [62], or the Grandi etl al. ionic model [63].

There have been also proposed several ways to model fibrosis within the LA there are those who opted for including structural changes affecting tissue properties such as interstitial conduction barriers [90], probabilistic percolation [91], or modified conductivities [92], and those who include electrical changes at cellular level such as incorporation of fibroblast [93, 94, 95], or modification of ion channels [96], or both [97]. Detailed biophysical and anatomical models of the atria and torso have been successfully employed to reproduce complex electrical activation patterns observed in experiments and clinics [118, 119]. One of the main goals of the patient-specific cardiac models and related simulations technologies is the development of decision-based support systems that can aid doctors in personalized plan and treatment for ablation procedures [144, 3]. In that direction, there have been already some promising attempts by Zahid et al. [145] that compared model-predicted optimal ablations with clinical lesions that rendered arrhythmia non-inducible.

One of the main drawback of the approaches based on multi-scale biophysical simulations is the requirements imposed, including: necessity of high computational power, time to perform simulations, expertise to build patient-specific models, and interpret results. That is the reason why novel approaches based on machine learning combined with multi-scale simulation are starting to be proposed for different clinical applications [147]. From the modeling perspective, algorithms have been developed, mainly based on decision trees, to help identify the source of FAT from BSPM data [111, 100]. In those studies, the presence of fibrosis was neglected or not considered in the models. Ignoring the effects of fibrosis is a clear limitation since current-resistant fibrotic tissue affects the activation patterns.

In this thesis, I have developed a pipeline that combines the use of multi-scale simulations of the atria and torso with ML techniques with the aim of localizing non-invasively the source of FAT in patients with different levels of LA fibrosis. To achieve that goal, I have studied the coupling of fibroblast and atrial myocytes, developed 25 different 3D fibrotic atrial models, performed more that 450 biophysical electrophysiology simulations and train

computer systems to identify the surface potential patterns produced by different atrial tachycardia ectopic focus. Finally, I have validated the pipeline in an exemplary clinical case acquired for that specific purpose.

7.2   Main Findings

In Chapter 3, I have performed an analysis on a 3D slab of tissue that combined healthy atrial tissue from different regions and fibrotic tissue to assess: (i) changes in action potential duration (APD), (ii) conduction velocities and (iii) depolarization patterns. We analyzed results for both diffuse fibrosis and patchy fibrosis. For the last, different densities of fibrosis were modeled, following the Utah levels were used.

The main findings from the simulation study were the following. There were clear electrophysiological effects on the Courtemanche-Ramirez- Nattel myocytes when coupling to the active formulation of McCannell fibroblast model due to the cell-to-cell electrotonic interaction, which caused a reduction of AP amplitude that could be appreciated with respect to the control trace as soon as the probe was near a more dense patchy fibrosis area. It produced a reduction of AP plateau, and a clear shortening of the myocyte APD90 with respect to the control AP and variable depending the location of the probe and the density of fibrosis. APD50 showed a more constant reduction of the APD as we went deep inside fibrotic areas showing a clear deformation of the AP profile. Also, it produced a prolonged repolarization of the AP compared to the uncoupled myocyte, and more significantly, fibroblasts had a higher resting membrane potential (RMP) and hence affected directly the myocyte RMP, which was constantly elevated. With respect to the effect at tissue level, conduction channels (within fibrotic regions) with a width smaller than 1.2 mm produced a propagation, channels of 1.5mm width propagated the signal (electrotonic currents), but the APs showed very low amplitude, and channels larger than 3mm show normal propagation patterns. In addition, fibrotic barriers located in healthy tissue larger than 1 mm produced conduction blocks.

In Chapter 4, I have developed a 3D atrial model that included different distributions of fibrosis, based on finding collected from a set of LGE MRI sequences acquired at Utah University. In addition, I have simulated FAT from a set of locations reported in the literature and obtained the LAT maps and the BSPiM associated to each simulation, to study the effects of fibrosis

from cellular to whole body scale. In total more than 450 simulations were carried out.

Our results agreed with observations from several studies in the literature, since there were appreciated changes in the maximum values of the BSPiM, which are correlated to signal amplitude. This changes are mainly due to the disorganized activation and the inhomogeneous advance of the depolarization wavefront that has to skip obstacles and it is delayed in some regions. This is also the reason why there is not a clear evolution pattern as fibrosis increases, and it is difficult to predict the outcome of a given simulation. Fibrosis greatly modified the atrial activation pattern, slowing down wave propagation, and producing conduction blocks. Fibrosis patches caused atrial electrical heterogeneity, and large changes in the BSPiM as a function of the fibrosis distribution. However, the increase of fibrosis affected in a different way as a function of the FAT origin, making it more difficult to relate some BSPiM to a FAT origin in certain cases. One of the major repercussions on the BSPiM was observed when fibrosis affected the conduction links between both atria.

In Chapter 5, I developed a pipeline to predict the triggering site of a FAT using only BSPM data to help electrophysiologists pre- and intra-operatively. To achieve this goal, I related a BSPM-derived index to the source of a FAT even in the face of fibrosis patches that could be present in different distributions and densities. In addition, I set out to ascertain the effect of fibrosis on the BSPM-derived indices. The proposed method uses ML techniques to develop a prediction pipeline that should be able to learn the relationship between BSPMs and ectopic foci location. We trained this system with a simulation database, generated by means of a detailed biophysical model of 3D human atria, in which we have control of the input parameters, and can simulate the desired scenarios.

The pipeline presented improves previous results in non-fibrotic patients and obtains an accuracy above 90% for classifying ectopics into 6 different atrial regions (i.e., from K = 2 to K = 6). In addition, it can reduce the dimensionality of the BSPiM patterns, considering noise, to obtain data similar to that acquired in a clinical environment. By means of feature selection analysis, I could find the minimum number of electrodes required to predict, with high accuracy, the location of ectopic foci during FAT. For cases without fibrosis, I could obtain predictions (dividing the atria in K = 4 regions) with an accuracy of 0.90 with only 16 features or electrodes placed on the torso front. When detection considered more and smaller

regions (from K = 6 to K = 10), the accuracy was reduced to a minimum accuracy of 0.81 for K = 10, and a maximum of 256 electrodes.

As soon as LA patchy fibrosis comes into play, (i.e., Stage 1 to Stage 5), together with an increase in the number of regions analyzed, (i.e., K = 2 to K = 10), the measure of overlapped regions ratio increases, confirming that overlapping, and the ratio of well formed clusters, or convexity, decreases, demonstrating the presence of ectopics disconnected or isolated from their group. However, the classification accuracy, remained above the value of 0.90 for numbers electrodes ranging from 128 to 256, even for the most extreme case, which is the model M5. The high accuracy was obtained because I allowed the clusters of patches to be disconnected. From a clinical point of view, the location of the atrial trigger will not be so efficient since the area of search increases, but still the method improves current clinical practice. A positive point is that in cases in which a given atrial patch has more than one label, the main patches associated with the label are in general neighbors. That means that patches in the borders of two regions sometimes are classified as label "a" and sometimes a neighboring region "b."

In Chapter 6, I setup a hardware acquisition system to record a large number of body surface electrograms, and precisely localize them in the patient's torso using a 3D camera. Using the system, a patient candidate to PVI by RFA was chosen and monitored. FAT was triggered in the atria by a pace-mapping protocol that allowed to record the BSPM associated with each ectopic focus, as well as the exact location of the ectopic focus in an RV EAM. The datasets were collected to validate all the pipelines developed in Chapters 4 and 5, and check whether a system trained exclusively with simulations can be used to classify patient's data. We observed that for most ectopic foci location there is a good match between the simulations and the patient data, with a few exceptions in areas that present a large variability in the ECG.

In conclusion, the methods and the ML pipeline developed in this thesis have shown the potential of computational tools to reproduce certain atrial arrhythmias such as FAT in a fibrotic atria, as well as to train ML model to classify the origin of a FAT. This proof-of-concept demonstrates the impact that biophysical modeling can have to clinics in terms in therapy planning and optimization, since it can help finding the origin of a FAT pre-operatively from non-invasive data, or reduce intervention times.

One of the advantages of this methodology is that it can be extended to

other pathologies, such as VT, and it only requires non-invasive data from the patients, which permits the its use as a pre-operative. In addition, thanks to the combination with pre-trained ML models, it is not necessary to carry out expensive computational simulations or perform the patient-specific reconstructions of the 3D models. Therefore, the technology can be easily translated to the clinical environment, where no special hardware or advance computational background would be required. In addition, all the libraries employed to develop the methodology are open-source scientific software packages, which can help its translation.

7.3 Contributions

This thesis presents the following contributions that arise directly from the initial main goals:

- **To study the effect of coupling fibroblast and healthy atrial tissue on the electrical wave propagation.** The effects of coupling the CRN atrial ionic model and the McCannel fibroblast model have been studied and quantified at cellular and tissue level, with the set of parameters defined in our 3D atrial model. The study is reported for two atrial regions, the LA and the PVs. Although there are several studies on this topic, our results are related to the 3D open-source atrial model we have based on all our simulation study, and are relevant for other researcher that make use of the same 3D model.

- **To build a set of 3D atrial models with varying fibrosis distribution and perform FAT multi-scale electrophysiology simulations for each scenario.** We created a database of 25 3D atrial models that include fibrosis, randomly included, but considering distributions observed in real patients by LGE MRI. In addition, for each atrial model, we have the atrial activation sequence triggered from 19 locations and the corresponding BSPM and BSPiM, which could be used to understand the relationship between intracavitary activation and the surface multi-electrode ECG, saving several months of computation.

- **To develop a machine learning system trained with electrophysiology FAT simulations to support clinicians to predict**

the location of ectopic foci prior to the RFA intervention. This is one of the main contributions of the thesis, and consist of a full computational pipeline where BSPiM labeled data can be used to train a ML model that is able to cluster and classify the data with the aim of predicting the location (atrial region) of an ectopic focus in presence of fibrosis. In addition, the methodology is able to determine the optimal electrodes (number and position) to classify patients.

- **To validate the proposed methodology on an exemplary clinical case.** We setup a hardware and software system able to acquire in the EP Lab information from a patient that is undergoing a RFA. That information was semi-automatically processed, and permitted to accurately locate the electrodes of a multi-electrodes system and relate them to nodes of our computational model. In addition, we could perform on those nodes the signal processing necessary to obtain the patient BSPiM, and subsequently classify it to predict the origin of the FAT.

7.4 Limitations

There are several limitations of the work presented that are summarized in the following paragraphs.

- **Modeling fibrosis.** There have been proposed a number of approaches to model fibrotic tissue in the atria, such as, interstitial conduction barriers or probabilistic percolation that we have not considered in this thesis. In addition, in our approach we took several decisions, such as the conductivity values used to connect fibroblast and atrial myocytes, or conductivity of different regions of the atria. Using a different set of parameters might slightly change the results we obtained, for instance, modification in AP in areas close to fibrotic patches, or the effect of a fibrotic barrier in the wavefront propagation. Due to the lack of data to validate our results at tissue level, we took the decision of using approaches from the literature that were able to elicit macroscopic effects, such as atrial fibrillation at organ level.

- **Fibrosis distribution in 3D models.** First of all, we did not use a patient-specific distribution of fibrosis used on LGE MRI in our study. However, we did use values to distribute the fibrosis that corresponded

to observation taken from a set of patients from Utah University that underwent LGE MRI. On the other hand, we included fibrosis only in the LA.

- **Use of a single 3D atrial geometry.** One of the most important limitations is that although the activation patterns were validated against a clinical database, they have been simulated and do not correspond to real patients. In addition, patient atrial shape variability could introduce slight differences in the P wave morphology that in turn will affect the BSPiM patterns in some cases. Finally, the localization of ectopic focus is based on regions, and therefore the electrophysiologist still has to determine where exactly the focal point is within the predicted region.

- **Validation of BSPiM including fibrosis.** In a previous work we were able to compare simulated BSPiM with database available from the literature, obtaining a very good much for all the ectopic foci. However, we do not have similar clinical data to validate simulations including fibrosis. The electrophysiology models we selected have been validated by other researchers with access to LGE MRI patient-specific data, but were never employed with the objective of this thesis. Therefore, it will be important to build different patient-specific models and obtain the related BSPiM to check if the data used to train the ML pipeline is accurate, and the minimum number of fibrotic configurations required to have a sample large enough to obtain good classification results.

- **Use of additional biomarkers for training.** In this thesis we considered a single biomarker to predict the location of an ectopic focus, the BSPiM. This biomarker can have a number of characteristics that depend on the number of electrodes placed on the patient torso. However, there might be other characteristics that provide valuable information to the ML pipeline for classification that could be explorer. The reason for using this particular biomarker was the access to data for validation in healthy conditions, and its robustness among patients, since it is based on the overall P-wave integral pattern across the torso. Using a more sensitive biomarker that depends on P-wave morphology or amplitude might be more difficult to generalize among patients or between simulations and real cases.

- **Extraction of the P-wave from multi-electrode recordings.** In this thesis, in order to cancel out VA in the ECG, we choose to suppress the QRS complex and T wave through the subtraction of a fixed template being called Template Matching Subtraction (TMS) [181, 180]. One of the main limitations of these methods such as high sensitivity to QRS morphological changes and their inability to eliminate artifacts from electrode movement or ectopic beats [185].

- **Data available for a single patient.** One of the major limitations is that the methodology was validated in a single patient. Conclusions obtained with one patient are not relevant, and can be only considered to illustrate the full patient in an exemplary case. On the positive side, the process allowed us to tune different algorithms to be able to process in a more automatic fashion new cases.

7.5   Future Work

Although the initial thesis goals have been fulfilled, after completing them, several additional issues have been identified and will be carried out in the future.

First of all, given the fact that AF-perpetuating re-entrant sources have also been found to localize in the RA [188], and have even been directly targeted for catheter ablation [189], an important short-term goal is to generate new simulations where development of fibrosis is present on both the RA and LA.

A second goal will involve the increase of the simulation database, to take into account more patient anatomies and orientations of the atria, which would enrich the model trained. In parallel, more patient that would have to be collected to have a larger test, making sure that we use the maximum number of electrodes in the torso of the patient.

A third, and more ambitious goal, is to enlarge the amount of patient datasets acquired with our electrode systems together with LGE MRI, which will allow us not only to further validate the methodology, but to define new biomarkers that help in the prediction of arrhythmia origin. Most of the available datasets online are built to study AF, instead of AT, and therefore the data required to train our models is scarce and in most cases have to be acquired locally in our clinical collaborator centers.

This third goal goes inline with the extension of the methods to include other arrhythmias with more complex electrical activation patterns, such as macro-reentrant tachycardias, typical and atypical flutter, which are more problematic to treat in the EP-Lab. That would most surely require to study additional biomarkers and ML models to learn the temporally dynamic patters observed in some og those arrhythmia.

8

Thesis Publications

Journal papers

1. **Godoy E.**, Lozano M., García-Fernández I., Ferrer-Albero A., MacLeod R., Saiz J., Sebastian R. Atrial fibrosis hampers non-invasive localization of atrial ectopic foci from multi-electrode signals: A 3D simulation study. Frontiers in Physiology Vol. 9(404):, pp. 1 - 18, 2018.

Conference papers

1. **Godoy E.**, Ferrer-Albero A., Lozano M., Garcia-Fernandez I., MacLeod R., Saiz J., Sebastian R. Effect of fibrosis on BSPM of patients with focal atrial tachycardia. Virtual Physiological Human Conference (VPH2018). Zaragoza, 5-7 September, 2018

2. **Godoy E.**, Lozano M., Garcia-Fernandez I., Sebastian R. Combining Biophysical Modeling and Machine Learning to predict location of atrial Ectopic Triggers. Computing in Cardiology Conference, Vol 45, Maastricht, 23-26 September, 2018.

3. **Godoy E.**, Lozano M., Ferrer A., Saiz J., Sebastian R. Optimal Surface ECG Electrode Set For Prediction of Atrial Ectopic Foci Region. 5th International Conference on Computational and Mathematical Biomedical Engineering - CMBE2017, 10–12 April 2017, USA. Vol 1. pp. 206-209, 2017.

4. **Godoy E.**, López J., Bermúdez L., Ferrer-albero A., García N., García-Vicent C., Lurbe E.F., Saiz J. Time-Domain, Frequency Do-

main and non-linear measurements in neonates' Heart Rate Variability with clinical sepsis. Computing in Cardiology 2014. pp. 429-432. IEEE. 2014.

5. **Godoy E**, Romero L, Ferrero JM. Comparing Hodgkin-Huxley and Markovian Formulations for the Rapid Potassium Current in Cardiac Myocytes: A Simulation Study. XIII Mediterranean Conference on Medical and Biological Engineering and Computing 2013. pp. 931-934. Springer, Cham. 2014.

6. **Godoy E.**, López J., Bermúdez L., Ferrer-albero A., García N., García-Vicent C., Lurbe E.F., Saiz J. Fractal Changes in the Long-Range Correlation and Loss of Signal Complexity in Infant's Heart Rate Variability with Clinical Sepsis. XIII Mediterranean Conference on Medical and Biological Engineering and Computing 2013. pp. 714-717. Springer, Cham. 2014.

Other related papers

1. **Ferrer-Albero A.**, Godoy E.J., Lozano M., Martinez-Mateu L., Atienza F., Saiz J., Sebastian R. Non-invasive localization of atrial ectopic beats by using simulated body surface P-wave integral maps. PLoS ONE, Vol. 12(7):e0181263, pp. 1 - 23, 2017.

2. **Carbonell-Pascual B.**, Godoy E., Ferrer-Albero A, Romero L., Ferrero J.M.Comparison between Hodgkin–Huxley and Markov formulations of cardiac ion channels. Journal of theoretical biology 399, 92-102, 2016.

3. **Ferrer A.**, Sebastian R., Sanchez-Quintana D., Rodriguez J.F., Godoy E.J., Martinez, L., Saiz J. Detailed anatomical and electrophysiological models of human atria and torso for the simulation of atrial activation. PLOS One, Vol. 10(11):e0141573, pp. 1 - 29, 2015.

A

Catalogue of Simulation Results for fibrotic Case 1

A.1   LAT maps for all FAT
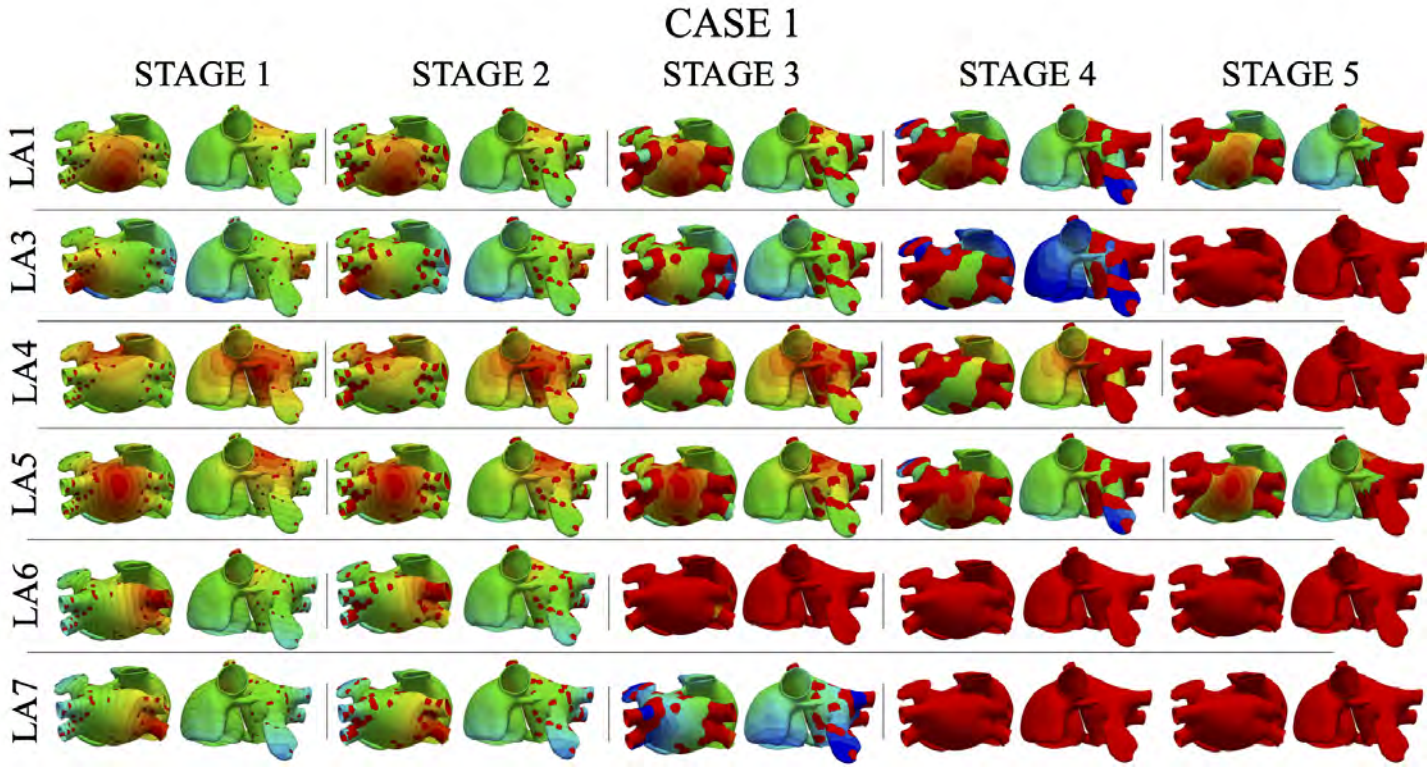
Figure A.1: LAT maps for Case 1 (including a fibrotic substrate) triggered from 6 different ectopic foci in the LA. Labels indicate the origin of the stimulus.
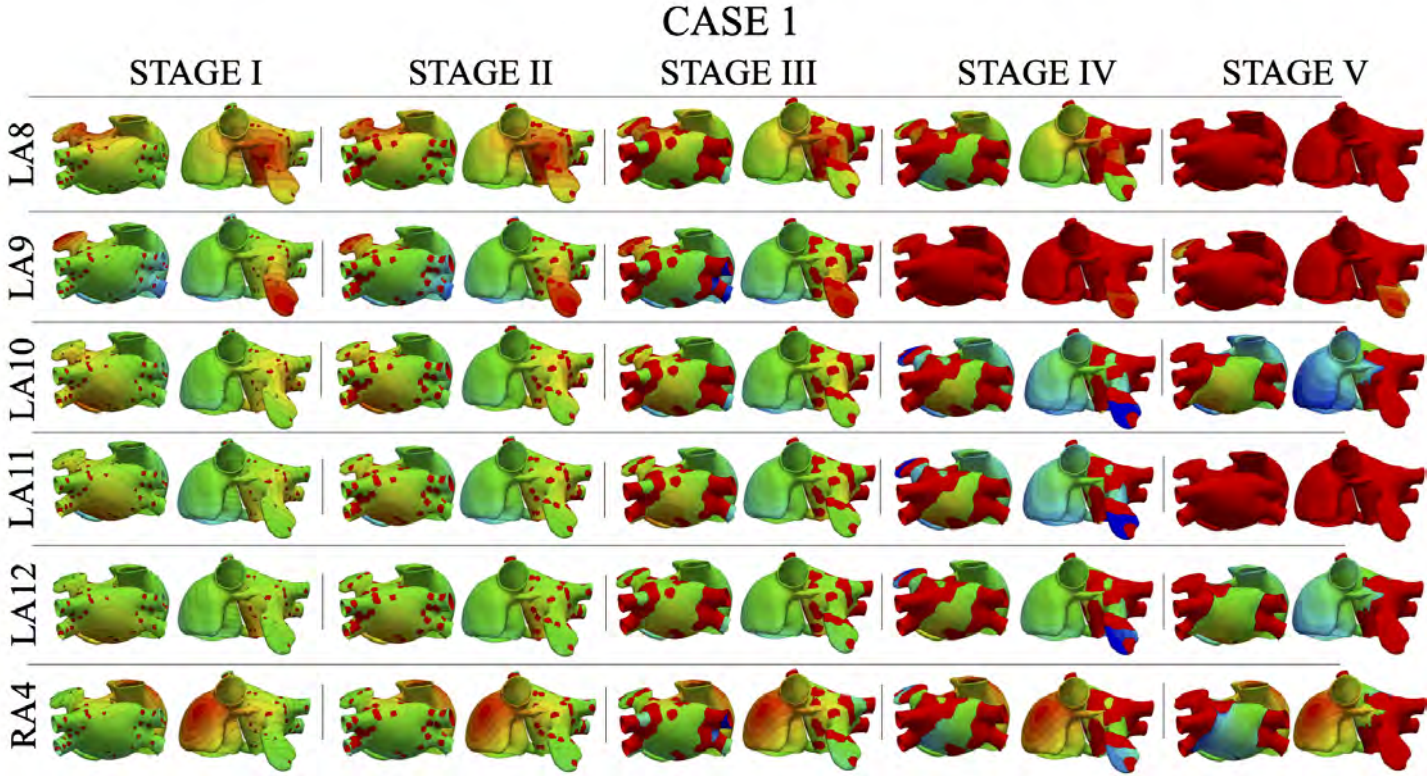
Figure A.2: LAT maps for Case 1 (including a fibrotic substrate) triggered from 5 different ectopic foci in the LA and 1 in the RA. Labels indicate the origin of the stimulus.
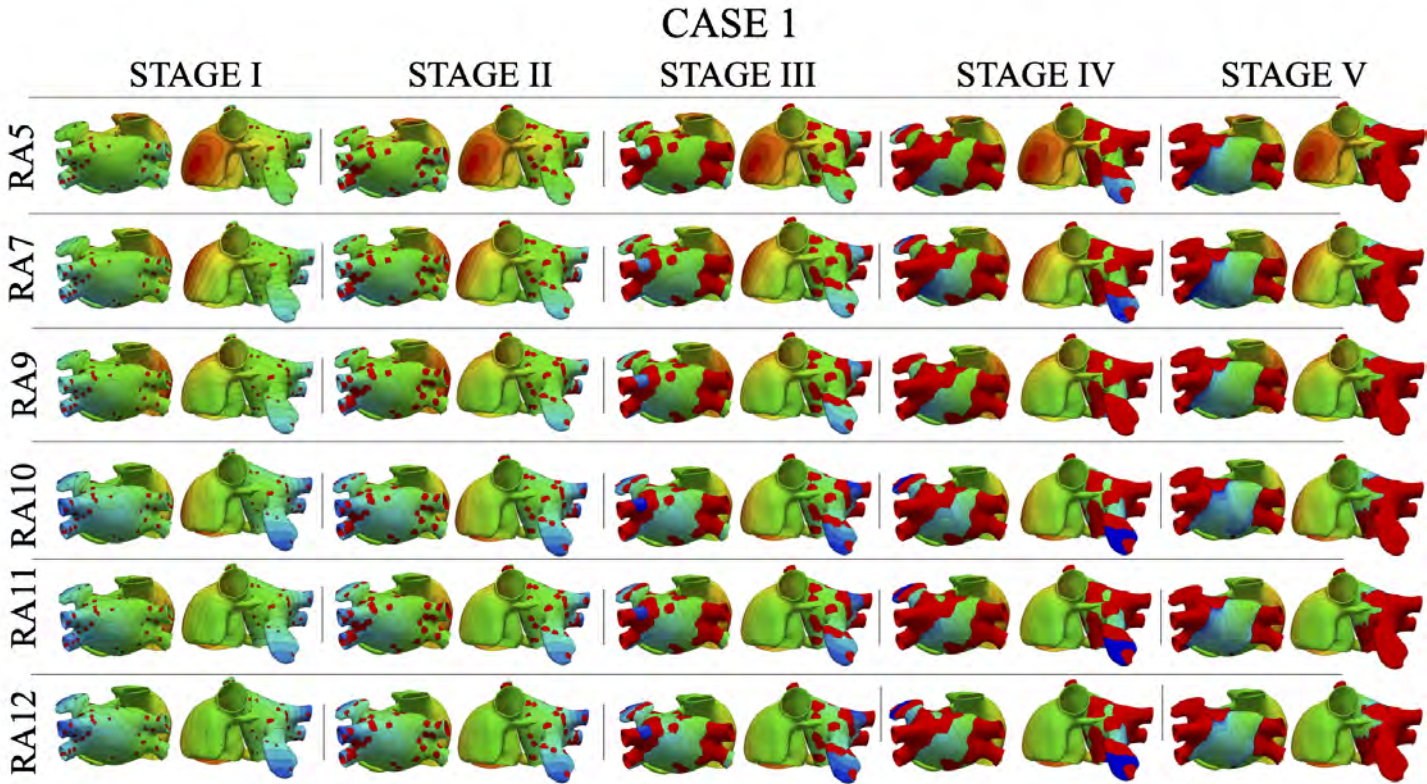
Figure A.3: LAT maps for Case 1 (including a fibrotic substrate) triggered from 6 different ectopic foci in the RA. Labels indicate the origin of the stimulus.
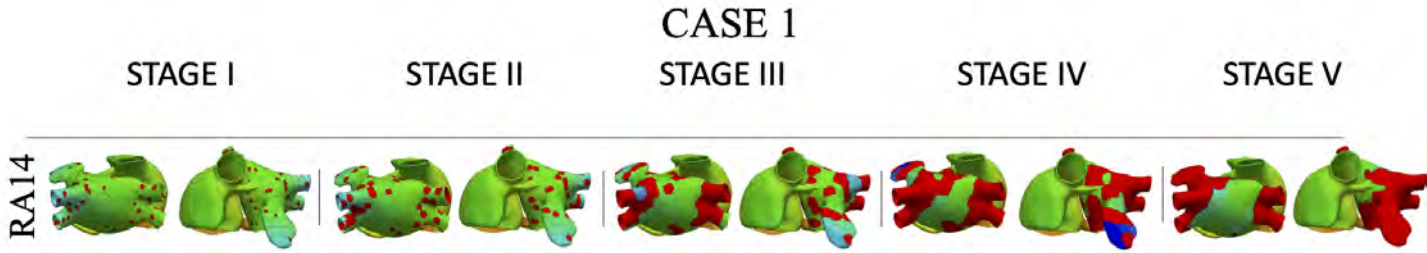
Figure A.4: LAT maps for Case 1 (including a fibrotic substrate) triggered from 1 ectopic focus in the RA. Labels indicate the origin of the stimulus.

A.2 BSPiMs for all FAT
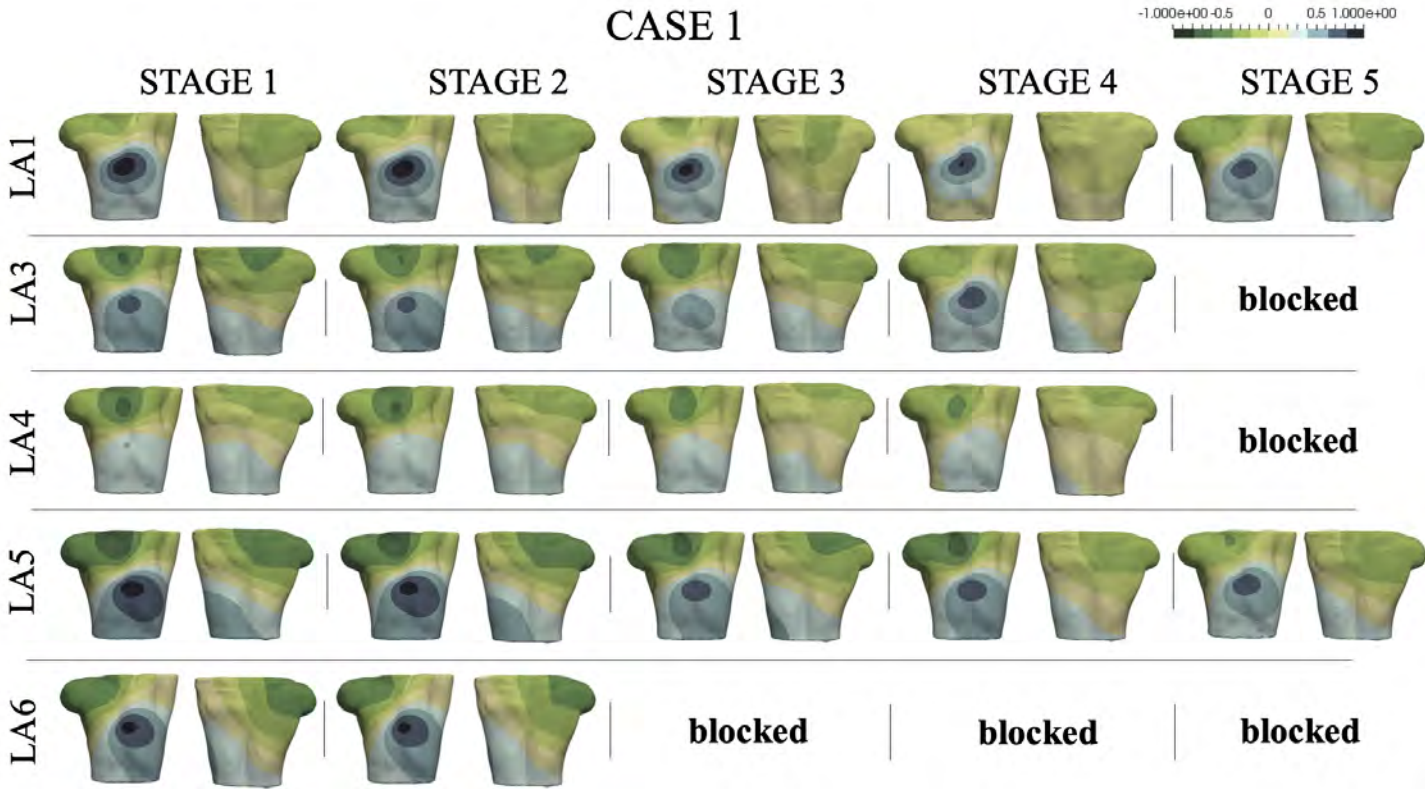
Figure A.5: BSPiMs for fibrotic models triggered from 5 ectopic foci located in the LA.
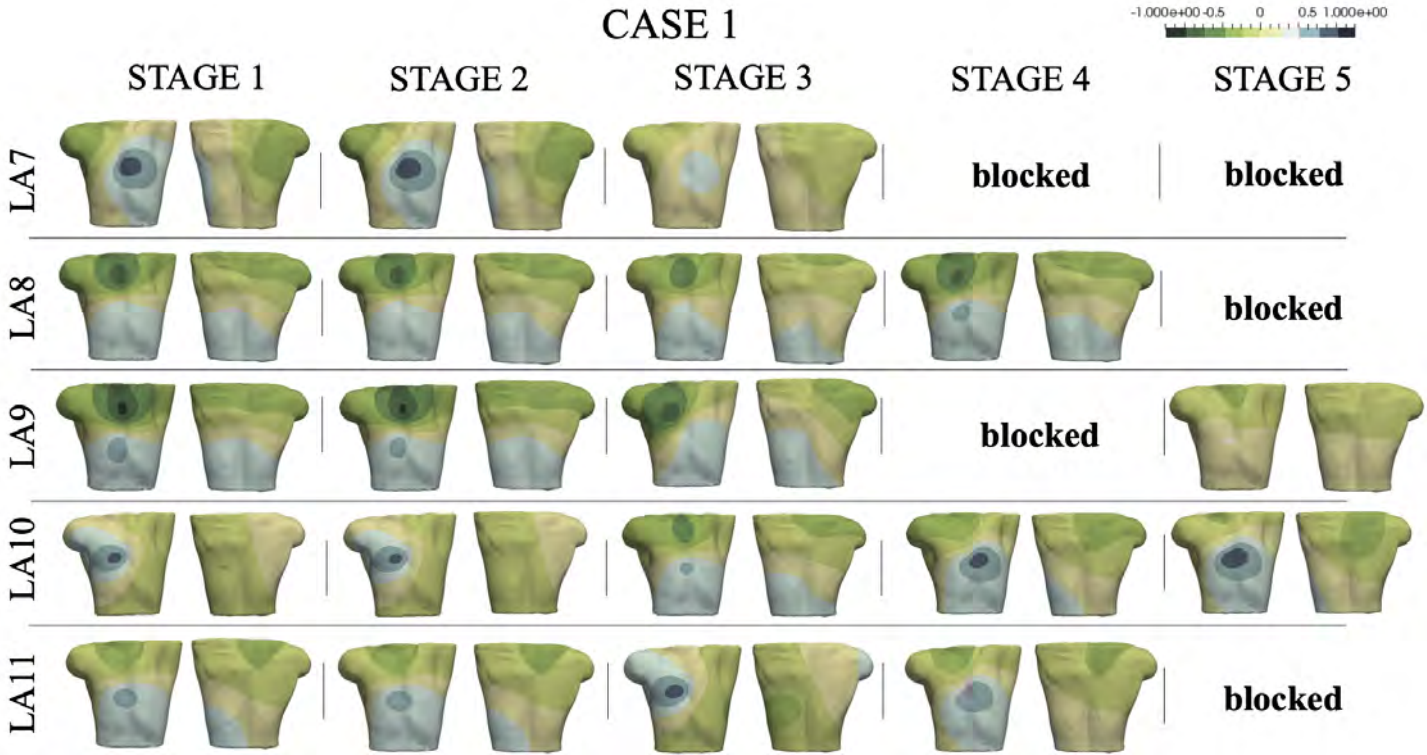
Figure A.6: BSPiMs for fibrotic models triggered from 5 ectopic foci located in the LA.
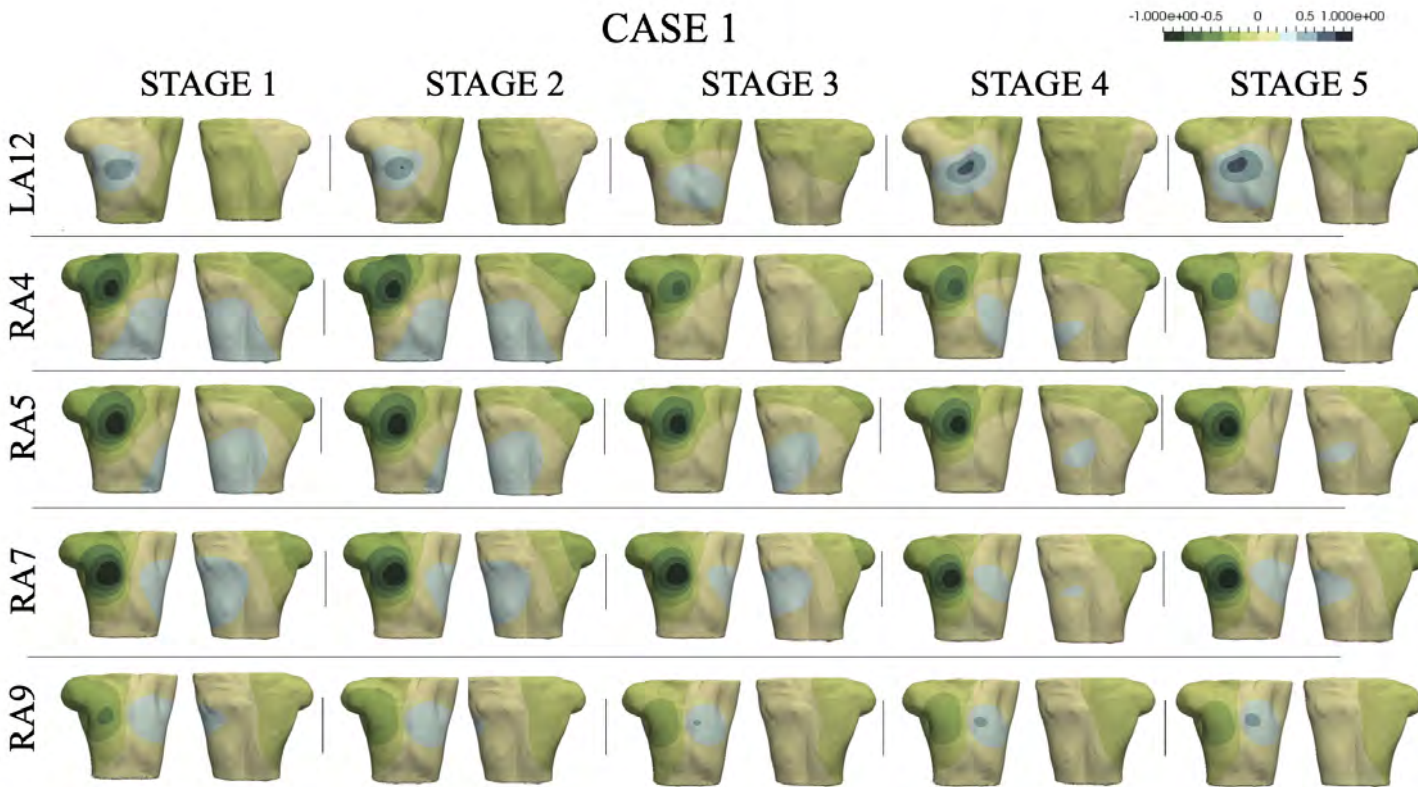
Figure A.7: BSPiMs for fibrotic models triggered from 4 ectopic foci located in the RA and 1 in the LA.
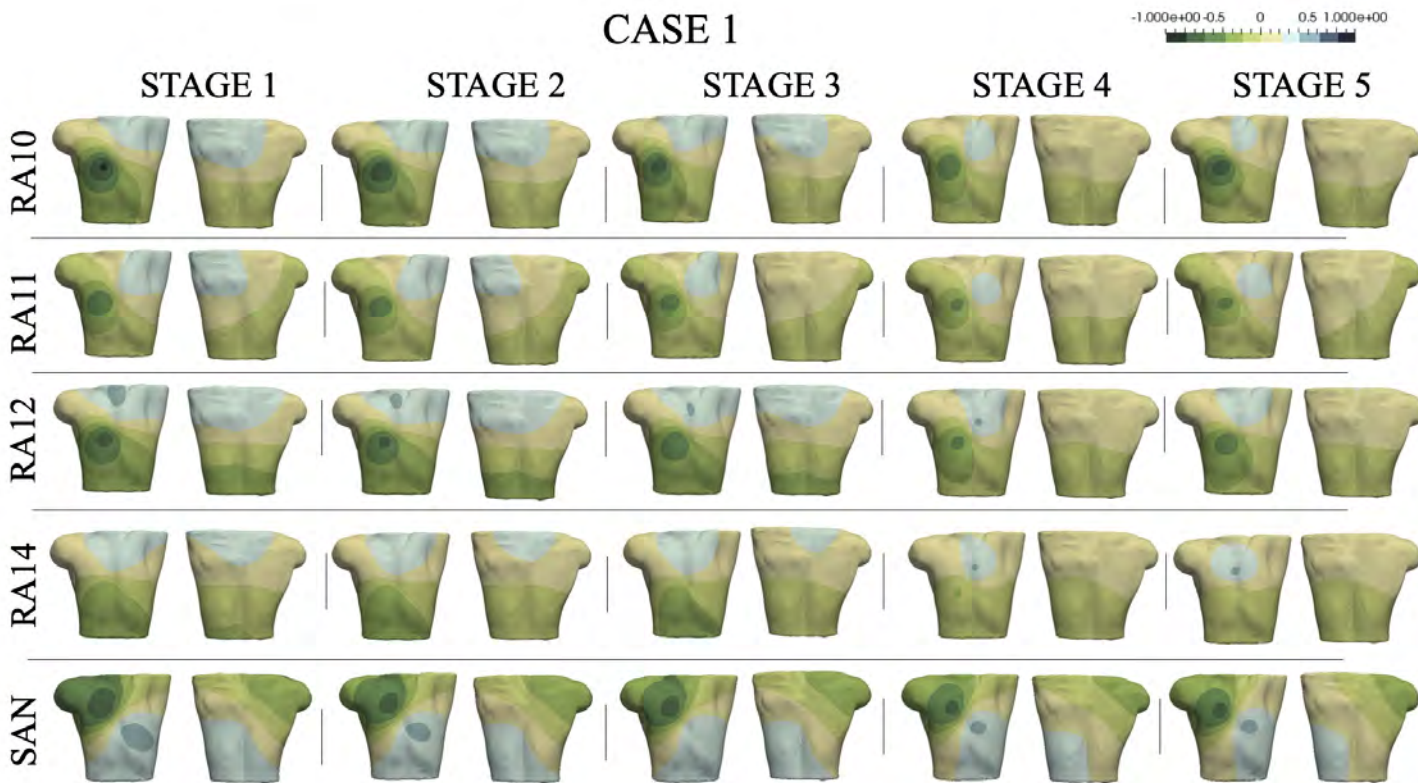
Figure A.8: BSPiMs for fibrotic models triggered from 5 ectopic foci located in the RA.

Bibliography

[1] A John Camm, Paulus Kirchhof, Gregory Y H Lip, Ulrich Schotten, Irene Savelieva, Sabine Ernst, Isabelle C Van Gelder, Nawwar Al-Attar, Gerhard Hindricks, Bernard Prendergast, Hein Heidbuchel, Ottavio Alfieri, Annalisa Angelini, Dan Atar, Paolo Colonna, Raffaele De Caterina, Johan De Sutter, Andreas Goette, Bulent Gorenek, Magnus Heldal, Stefan H Hohloser, Philippe Kolh, Jean-Yves Le Heuzey, Piotr Ponikowski, Frans H Rutten, and ESC Committee for Practice Guidelines. Guidelines for the management of atrial fibrillation: the task force for the management of atrial fibrillation of the european society of cardiology (esc). *Europace*, 12(10):1360–420, 10 2010.

[2] Charulatha Ramanathan, Ping Jia, Raja Ghanem, Daniela Calvetti, and Yoram Rudy. Noninvasive electrocardiographic imaging (ECGI): Application of the generalized minimal residual (GMRes) method. *Annals of Biomedical Engineering*, 2003.

[3] Natalia A Trayanova, Patrick M Boyle, and Plamen P Nikolov. Personalized imaging and modeling strategies for arrhythmia prevention and therapy. *Curr Opin Biomed Eng*, 5:21–28, Mar 2018.

[4] Patrick M Boyle, Joe B Hakim, Sohail Zahid, William H Franceschi, Michael J Murphy, Edward J Vigmond, Rémi Dubois, Michel Haïssaguerre, Mélèze Hocini, Pierre Jaïs, Natalia A Trayanova, and Hubert Cochet. Comparing reentrant drivers predicted by image-based computational modeling and mapped by electrocardiographic imaging in persistent atrial fibrillation. *Front Physiol*, 9:414, 2018.

[5] Richard L Drake, Richard L Drake, and Henry Gray. *Gray's atlas of anatomy*. Churchill Livingstone, Philadelphia, 1st ed edition, 2008.

[6] J Farré, J A Cabrera, D Sánchez-Quintana, S Yen Ho, and R H Anderson. [anatomy of the atria for rhythmologists]. *Arch Mal Coeur Vaiss*, 96 Spec No 7:32–6, Dec 2003.

[7] Damián Sánchez-Quintana, José Ramón López-Mínguez, Yolanda Macías, José Angel Cabrera, and Farhood Saremi. Left atrial anatomy relevant to catheter ablation. *Cardiol Res Pract*, 2014:289720, 2014.

[8] Luigi Di Biase, Pasquale Santangeli, Matteo Anselmino, Prasant Mohanty,

Ilaria Salvetti, Sebastiano Gili, Rodney Horton, Javier E Sanchez, Rong Bai, Sanghamitra Mohanty, Agnes Pump, Mauricio Cereceda Brantes, G Joseph Gallinghouse, J David Burkhardt, Federico Cesarani, Marco Scaglione, Andrea Natale, and Fiorenzo Gaita. Does the left atrial appendage morphology correlate with the risk of stroke in patients with atrial fibrillation? results from a multicenter study. *J Am Coll Cardiol*, 60(6):531–8, Aug 2012.

[9] Luigi Di Biase, J David Burkhardt, Prasant Mohanty, Javier Sanchez, Sanghamitra Mohanty, Rodney Horton, G Joseph Gallinghouse, Shane M Bailey, Jason D Zagrodzky, Pasquale Santangeli, Steven Hao, Richard Hongo, Salwa Beheiry, Sakis Themistoclakis, Aldo Bonso, Antonio Rossillo, Andrea Corrado, Antonio Raviele, Amin Al-Ahmad, Paul Wang, Jennifer E Cummings, Robert A Schweikert, Gemma Pelargonio, Antonio Dello Russo, Michela Casella, Pietro Santarelli, William R Lewis, and Andrea Natale. Left atrial appendage: an underrecognized trigger site of atrial fibrillation. *Circulation*, 122(2):109–18, Jul 2010.

[10] Allison M. Pritchett, Steven J. Jacobsen, Douglas W. Mahoney, Richard J. Rodeheffer, Kent R. Bailey, and Margaret M. Redfield. Left atrial volume as an index of left atrial size: A population-based study. *Journal of the American College of Cardiology*, 41(6):1036–1043, 2003.

[11] Ulrich Schotten, Hans-Ruprecht Neuberger, and Maurits A Allessie. The role of atrial dilatation in the domestication of atrial fibrillation. *Progress in Biophysics and Molecular Biology*, 82(1-3):151–162, may 2003.

[12] S Y Sánchez-Quintana, D and Anderson, R H and Cabrera, J A and Climent, V and Martin, R and Farré, J and Ho. The terminal crest: morphological features relevant to electrophysiology. *Heart*, 49(20):406–412, 2002.

[13] Damián Sánchez-Quintana and Siew Yen Ho. [anatomy of cardiac nodes and atrioventricular specialized conduction system]. *Rev Esp Cardiol*, 56(11):1085–92, Nov 2003.

[14] José Angel Cabrera, Damian Sánchez-Quintana, Jerónimo Farré, José Manuel Rubio, and Yen Ho Siew. The inferior right atrial isthmus: Further architectural insights for current and coming ablation technologies. *Journal of Cardiovascular Electrophysiology*, 16(4):402–408, 2005.

[15] GREGORY K FELD, MICHAEL MOLLERUS, ULRIKA BIRGERSDOTTER-GREEN, OSAMU FUJIMURA, TRISTRAM D BAHNSON, K E R BOYCE, and MARC RAHME. Conduction Velocity in the Tricuspid Valve-Inferior Vena Cava Isthmus is Slower in Patients With Type I Atrial Flutter Compared to Those Without a History of Atrial Flutter. *Journal of Cardiovascular Electrophysiology*, 8(12):1338–1348, 1997.

[16] Farhad Pashakhanloo, Daniel A Herzka, Hiroshi Ashikaga, Susumu Mori, Neville Gai, David A Bluemke, Natalia A Trayanova, and Elliot R McVeigh. Myofiber architecture of the human atria as revealed by submillimeter diffusion tensor imaging. *Circ Arrhythm Electrophysiol*, 9(4):e004133, Apr 2016.

[17] D. Sánchez-Quintana, J. A. Cabrera, J. Farré, V. Climent, R. H. Anderson, and Siew Yen Ho. Sinus node revisited in the era of electroanatomical mapping and catheter ablation. *Heart*, 91(2):189–194, 2005.

[18] Patrizia Camelliti, Colin R. Green, Ian LeGrice, and Peter Kohl. Fibroblast Network in Rabbit Sinoatrial Node: Structural and Functional Identification of Homogeneous and Heterogeneous Cell Coupling. *Circulation Research*, 94(6):828–835, 2004.

[19] Patrizia Camelliti, Thomas K. Borg, and Peter Kohl. Structural and functional characterisation of cardiac fibroblasts. *Cardiovascular Research*, 65(1):40–51, 2005.

[20] Pyotr G Platonov. Atrial fibrosis: an obligatory component of arrhythmia mechanisms in atrial fibrillation? *J Geriatr Cardiol*, 14(3):174–178, Mar 2017.

[21] Antonio P. Beltrami, Konrad Urbanek, Jan Kajstura, Shao-Min Yan, Nicoletta Finato, Rossana Bussani, Bernardo Nadal-Ginard, Furio Silvestri, Annarosa Leri, C Alberto Beltrami, and Piero Anversa. Evidence that human cardiac myocytes divide after myocardial infarction. *The New England Journal of Medicine*, 344(23):1130–1135, 2001.

[22] Deidre MacKenna, Sonya R. Summerour, and Francisco J. Villarreal. Role of mechanical factors in modulating cardiac fibroblast function and extracellular matrix synthesis. *Cardiovascular Research*, 46(2):257–263, 2000.

[23] Brett Burstein and Stanley Nattel. Atrial Fibrosis: Mechanisms and Clinical Relevance in Atrial Fibrillation. *Journal of the American College of Cardiology*, 51(8):802–809, 2008.

[24] Ivan V. Kazbanov, Kirsten H.W.J. Ten Tusscher, and Alexander V. Panfilov. Effects of Heterogeneous Diffuse Fibrosis on Arrhythmia Dynamics and Mechanism. *Scientific Reports*, 6(September 2015):1–14, 2016.

[25] Nassir F. Marrouche, David Wilber, Gerhard Hindricks, Pierre Jais, Nazem Akoum, Francis Marchlinski, Eugene Kholmovski, Nathan Burgon, Nan Hu, Lluis Mont, Thomas Deneke, Mattias Duytschaever, Thomas Neumann, Moussa Mansour, Christian Mahnkopf, Bengt Herweg, Emile Daoud, Erik Wissner, Paul Bansmann, and Johannes Brachmann. Association of atrial tissue fibrosis identified by delayed enhancement MRI and atrial fibrillation catheter ablation: The DECAAF study. *JAMA - Journal of the American Medical Association*, 311(5):498–506, 2014.

[26] Ross Morgan, Michael A. Colman, Henry Chubb, Gunnar Seemann, and Oleg V. Aslanidi. Slow conduction in the border zones of patchy fibrosis stabilizes the drivers for atrial fibrillation: Insights from multi-scale human atrial modeling. *Frontiers in Physiology*, 7(OCT):1–15, 2016.

[27] Franziska Fochler, Takanori Yamaguchi, Mobin Kheirkahan, Eugene G Kholmovski, Alan K Morris, and Nassir F Marrouche. Late gadolinium enhancement magnetic resonance imaging guided treatment of post-atrial fibrillation ablation recurrent arrhythmia. *Circ Arrhythm Electrophysiol*, 12(8):e007174,

Aug 2019.

[28] Robert Lemery, David Birnie, Anthony S L Tang, Martin Green, Michael Gollob, Matt Hendry, and Ernest Lau. Normal atrial activation and voltage during sinus rhythm in the human heart: an endocardial and epicardial mapping study in patients with a history of atrial fibrillation. *J Cardiovasc Electrophysiol*, 18(4):402–8, Apr 2007.

[29] Ana Ferrer, Rafael Sebastián, Damián Sánchez-Quintana, José F. Rodríguez, Eduardo J. Godoy, Laura Martínez, and Javier Saiz. Detailed Anatomical and Electrophysiological Models of Human Atria and Torso for the Simulation of Atrial Activation. *Plos One*, 10(11):e0141573, 2015.

[30] N. Saoudi, F. Cosío, A. Waldo, S. A. Chen, Y. Iesaka, M. Lesh, S. Saksena, J. Salerno, and W. Schoels. A classification of atrial flutter and regular atrial tachycardia according to electrophysiological mechanisms and anatomical bases: A statement from a joint expert group from the working group of arrhythmias of the European society of cardiology and the . *European Heart Journal*, 22(14):1162–1182, 2001.

[31] Jason P. Brown, David E. Krummen, Gregory K. Feld, and Sanjiv M. Narayan. Using Electrocardiographic Activation Time and Diastolic Intervals to Separate Focal From Macro-Re-Entrant Atrial Tachycardias. *Journal of the American College of Cardiology*, 49(19):1965–1973, 2007.

[32] S A Chen, C E Chiang, C J Yang, C C Cheng, T J Wu, S P Wang, B N Chiang, and M S Chang. Sustained atrial tachycardia in adult patients. Electrophysiological characteristics, pharmacological response, possible mechanisms, and effects of radiofrequency ablation. *Circulation*, 90(3):1262–78, 1994.

[33] J M Kalman, J E Olgin, M R Karch, M Hamdan, R J Lee, and M D Lesh. "cristal tachycardias": origin of right atrial tachycardias from the crista terminalis identified by intracardiac echocardiography. *J Am Coll Cardiol*, 31(2):451–9, Feb 1998.

[34] J B Morton, P Sanders, A Das, J K Vohra, P B Sparks, and J M Kalman. Focal atrial tachycardia arising from the tricuspid annulus: electrophysiologic and electrocardiographic characteristics. *J Cardiovasc Electrophysiol*, 12(6):653–9, Jun 2001.

[35] Marius Volkmer, Matthias Antz, Joachim Hebe, and Karl-Heinz Kuck. Focal atrial tachycardia originating from the musculature of the coronary sinus. *J Cardiovasc Electrophysiol*, 13(1):68–71, Jan 2002.

[36] Kurt C Roberts-Thomson, Peter M Kistler, Haris M Haqqani, Andrew D McGavigan, Richard J Hillock, Irene H Stevenson, Joseph B Morton, Jitendra K Vohra, Paul B Sparks, and Jonathan M Kalman. Focal atrial tachycardias arising from the right atrial appendage: electrocardiographic and electrophysiologic characteristics and radiofrequency ablation. *J Cardiovasc Electrophysiol*, 18(4):367–72, Apr 2007.

[37] Denis Noble. From the hodgkin-huxley axon to the virtual heart. *J Physiol*, 580(Pt 1):15–22, Apr 2007.

[38] Natalia A Trayanova. Whole-heart modeling: applications to cardiac electrophysiology and electromechanics. *Circ Res*, 108(1):113–28, Jan 2011.

[39] Edward Vigmond, Fijoy Vadakkumpadan, Viatcheslav Gurev, Hermenegild Arevalo, Makarand Deo, Gernot Plank, and Natalia Trayanova. Towards predictive modelling of the electrophysiology of the heart. *Exp Physiol*, 94(5):563–77, May 2009.

[40] Hermenegild J Arevalo, Patrick M Boyle, and Natalia A Trayanova. Computational rabbit models to investigate the initiation, perpetuation, and termination of ventricular arrhythmia. *Prog Biophys Mol Biol*, 121(2):185–94, 07 2016.

[41] Alejandro Lopez-Perez, Rafael Sebastian, and Jose M Ferrero. Three-dimensional cardiac computational modelling: methods, features and applications. *Biomed Eng Online*, 14:35, Apr 2015.

[42] Alejandro Lopez-Perez, Rafael Sebastian, M Izquierdo, Ricardo Ruiz, Martin Bishop, and Jose M Ferrero. Personalized cardiac computational models: From clinical data to simulation of infarct-related ventricular tachycardia. *Front Physiol*, 10:580, 2019.

[43] Edison F Carpio, Juan F Gomez, Rafael Sebastian, Alejandro Lopez-Perez, Eduardo Castellanos, Jesus Almendral, Jose M Ferrero, and Beatriz Trenor. Optimization of lead placement in the right ventricle during cardiac resynchronization therapy. a simulation study. *Front Physiol*, 10:74, 2019.

[44] Fernando Barber, Miguel Lozano, Ignacio García-Fernández, and Rafael Sebastián. Inverse estimation of terminal connections in the cardiac conduction system. *Mathematical Methods in the Applied Sciences*, 41(6):2340–2349, 2018.

[45] Natalia A Trayanova, Thomas O'Hara, Jason D Bayer, Patrick M Boyle, Kathleen S McDowell, Jason Constantino, Hermenegild J Arevalo, Yuxuan Hu, and Fijoy Vadakkumpadan. Computational cardiology: how computer simulations could be used to develop new therapies and advance existing ones. *Europace*, 14 Suppl 5:v82–v89, Nov 2012.

[46] Alejandro F Frangi, Daniel Rueckert, Julia A Schnabel, and Wiro J Niessen. Automatic construction of multiple-object three-dimensional statistical shape models: application to cardiac modeling. *IEEE Trans Med Imaging*, 21(9):1151–66, Sep 2002.

[47] Maria Lorenzo-Valdés, Gerardo I Sanchez-Ortiz, Andrew G Elkington, Raad H Mohiaddin, and Daniel Rueckert. Segmentation of 4d cardiac mr images using a probabilistic atlas and the em algorithm. *Med Image Anal*, 8(3):255–65, Sep 2004.

[48] Roy C P Kerckhoffs, Andrew D McCulloch, Jeffrey H Omens, and Lawrence J Mulligan. Effects of biventricular pacing and scar size in a computational model of the failing heart with left bundle branch block. *Med Image Anal*, 13(2):362–9, Apr 2009.

[49] Kathleen S McDowell, Hermenegild J Arevalo, Mary M Maleckar, and Na-

talia A Trayanova. Susceptibility to arrhythmia in the infarcted heart depends on myofibroblast density. *Biophys J*, 101(6):1307–15, Sep 2011.

[50] Rashed Karim, R James Housden, Mayuragoban Balasubramaniam, Zhong Chen, Daniel Perry, Ayesha Uddin, Yosra Al-Beyatti, Ebrahim Palkhi, Prince Acheampong, Samantha Obom, Anja Hennemuth, Yingli Lu, Wenjia Bai, Wenzhe Shi, Yi Gao, Heinz-Otto Peitgen, Perry Radau, Reza Razavi, Allen Tannenbaum, Daniel Rueckert, Josh Cates, Tobias Schaeffter, Dana Peters, Rob MacLeod, and Kawal Rhode. Evaluation of current algorithms for segmentation of scar tissue from late gadolinium enhancement cardiovascular magnetic resonance of the left atrium: an open-access grand challenge. *J Cardiovasc Magn Reson*, 15:105, Dec 2013.

[51] D D Streeter, Jr, H M Spotnitz, D P Patel, J Ross, Jr, and E H Sonnenblick. Fiber orientation in the canine left ventricle during diastole and systole. *Circ Res*, 24(3):339–47, Mar 1969.

[52] Darren A Hooks, Karl A Tomlinson, Scott G Marsden, Ian J LeGrice, Bruce H Smaill, Andrew J Pullan, and Peter J Hunter. Cardiac microstructure: implications for electrical propagation and defibrillation in the heart. *Circ Res*, 91(4):331–8, Aug 2002.

[53] Ian LeGrice, Greg Sands, Darren Hooks, Dane Gerneke, and Bruce Smaill. Microscopic imaging of extended tissue volumes. *Clin Exp Pharmacol Physiol*, 31(12):902–5, Dec 2004.

[54] Bruce H Smaill, Ian J LeGrice, Darren A Hooks, Andrew J Pullan, Bryan J Caldwell, and Peter J Hunter. Cardiac structure and electrical activation: models and measurement. *Clin Exp Pharmacol Physiol*, 31(12):913–9, Dec 2004.

[55] Fernando Barber, Ignacio García-Fernández, Miguel Lozano, and Rafael Sebastian. Automatic estimation of purkinje-myocardial junction hot-spots from noisy endocardial samples: A simulation study. *Int J Numer Method Biomed Eng*, 34(7):e2988, 07 2018.

[56] S Y Ho, D Sanchez-Quintana, J A Cabrera, and R H Anderson. Anatomy of the left atrium: implications for radiofrequency ablation of atrial fibrillation. *J Cardiovasc Electrophysiol*, 10(11):1525–33, Nov 1999.

[57] D Gil, R Aris, A Borras, E Ramirez, R Sebastian, and M Vazquez. Influence of fiber connectivity in simulations of cardiac biomechanics. *Int J Comput Assist Radiol Surg*, 14(1):63–72, Jan 2019.

[58] Ruben Doste, David Soto-Iglesias, Gabriel Bernardino, Alejandro Alcaine, Rafael Sebastian, Sophie Giffard-Roisin, Maxime Sermesant, Antonio Berruezo, Damian Sanchez-Quintana, and Oscar Camara. A rule-based method to model myocardial fiber orientation in cardiac biventricular geometries with outflow tracts. *Int J Numer Method Biomed Eng*, 35(4):e3185, 04 2019.

[59] M Courtemanche, R J Ramirez, and S Nattel. Ionic mechanisms underlying human atrial action potential properties: insights from a mathematical

model. *Am J Physiol*, 275(1):H301–21, 07 1998.

[60] Mary M. Maleckar, Joseph L. Greenstein, Wayne R. Giles, and Natalia A. Trayanova. Electrotonic coupling between human atrial myocytes and fibroblasts alters myocyte excitability and repolarization. *Biophysical Journal*, 97(8):2179–2190, 2009.

[61] A Nygren, C Fiset, L Firek, J Clark, D Lindblad, R.B Clark, and W.R Giles. Mathematical model of an adult human atrial cell: the role of K+ currents in repolarization. *Circulation Research*, 82(7):63–81, 1998.

[62] Jussi T Koivumäki, Topi Korhonen, and Pasi Tavi. Impact of sarcoplasmic reticulum calcium release on calcium dynamics and action potential morphology in human atrial myocytes: a computational study. *PLoS Comput Biol*, 7(1):e1001067, Jan 2011.

[63] Eleonora Grandi, Sandeep V Pandit, Niels Voigt, Antony J Workman, Dobromir Dobrev, José Jalife, and Donald M Bers. Human atrial action potential and ca2+ model: sinus rhythm and chronic atrial fibrillation. *Circ Res*, 109(9):1055–66, Oct 2011.

[64] Mathias Wilhelms, Hanne Hettmann, Mary M Maleckar, Jussi T Koivumaki, Olaf Dossel, and Gunnar Seemann. Benchmarking electrophysiological models of human atrial myocytes. *Front Physiol*, 3:487, 2013.

[65] R Plonsey and R C Barr. Mathematical modeling of electrical activity of the heart. *J Electrocardiol*, 20(3):219–26, Jul 1987.

[66] Otto H. Schmitt. Biological information processing using the concept of interpenetrating domains. *Information Processing in The Nervous System*, pages 325–331, 1969.

[67] B J Roth. The electrical potential produced by a strand of cardiac muscle: a bidomain analysis. *Ann Biomed Eng*, 16(6):609–37, 1988.

[68] Chris Bradley, Andy Bowery, Randall Britten, Vincent Budelmann, Oscar Camara, Richard Christie, Andrew Cookson, Alejandro F Frangi, Thiranja Babarenda Gamage, Thomas Heidlauf, Sebastian Krittian, David Ladd, Caton Little, Kumar Mithraratne, Martyn Nash, David Nickerson, Poul Nielsen, Oyvind Nordbø, Stig Omholt, Ali Pashaei, David Paterson, Vijayaraghavan Rajagopal, Adam Reeve, Oliver Röhrle, Soroush Safaei, Rafael Sebastián, Martin Steghöfer, Tim Wu, Ting Yu, Heye Zhang, and Peter Hunter. Opencmiss: a multi-physics & multi-scale computational infrastructure for the vph/physiome project. *Prog Biophys Mol Biol*, 107(1):32–47, Oct 2011.

[69] Elvio A. Heidenreich, José M. Ferrero, Manuel Doblaré, and José F. Rodríguez. Adaptive macro finite elements for the numerical solution of monodomain equations in cardiac electrophysiology. *Annals of Biomedical Engineering*, 38(7):2331–2345, 2010.

[70] Corné Hoogendoorn, Rafael Sebastian, José Félix Rodriguez, Karim Lekadir, and Alejandro F Frangi. An atlas- and data-driven approach to initializing reaction-diffusion systems in computer cardiac electrophysiology. *Int J Nu-*

mer Method Biomed Eng, 33(8):e2846, 08 2017.

[71] Lars Buitinck, Gilles Louppe, Mathieu Blondel, Fabian Pedregosa, Andreas Mueller, Olivier Grisel, Vlad Niculae, Peter Prettenhofer, Alexandre Gramfort, Jaques Grobler, Robert Layton, Jake VanderPlas, Arnaud Joly, Brian Holt, and Gaël Varoquaux. API design for machine learning software: experiences from the scikit-learn project. In *ECML PKDD Workshop: Languages for Data Mining and Machine Learning*, pages 108–122, 2013.

[72] Stuart P. Lloyd. Least squares quantization in pcm. *IEEE Transactions on Information Theory*, 28:129–137, 1982.

[73] Christopher M. Bishop. *Pattern Recognition and Machine Learning*. Springer, 2006.

[74] Geert J. S. Litjens, Thijs Kooi, Babak Ehteshami Bejnordi, Arnaud Arindra Adiyoso Setio, Francesco Ciompi, Mohsen Ghafoorian, Jeroen A. W. M. van der Laak, Bram van Ginneken, and Clara I. Sánchez. A survey on deep learning in medical image analysis. *Medical Image Anal.*, 42:60–88, 2017.

[75] Shweta H Jambukia, Vipul K Dabhi, and Harshadkumar B Prajapati. Classification of ecg signals using machine learning techniques: A survey. In *2015 International Conference on Advances in Computer Engineering and Applications*, pages 714–721. IEEE, 2015.

[76] Gari D Clifford, Chengyu Liu, Benjamin Moody, H Lehman Li-wei, Ikaro Silva, Qiao Li, AE Johnson, and Roger G Mark. Af classification from a short single lead ecg recording: the physionet/computing in cardiology challenge 2017. In *2017 Computing in Cardiology (CinC)*, pages 1–4. IEEE, 2017.

[77] Zhaohan Xiong, Martin K Stiles, and Jichao Zhao. Robust ecg signal classification for detection of atrial fibrillation using a novel neural network. In *2017 Computing in Cardiology (CinC)*, pages 1–4. IEEE, 2017.

[78] Philip Warrick and Masun Nabhan Homsi. Cardiac arrhythmia detection from ecg combining convolutional and long short-term memory networks. In *2017 Computing in Cardiology (CinC)*, pages 1–4. IEEE, 2017.

[79] Shenda Hong, Meng Wu, Yuxi Zhou, Qingyun Wang, Junyuan Shang, Hongyan Li, and Junqing Xie. Encase: An ensemble classifier for ecg classification using expert features and deep neural networks. In *2017 Computing in Cardiology (CinC)*, pages 1–4. IEEE, 2017.

[80] Morteza Zabihi, Ali Bahrami Rad, Aggelos K Katsaggelos, Serkan Kiranyaz, Susanna Narkilahti, and Moncef Gabbouj. Detection of atrial fibrillation in ecg hand-held devices using a random forest classifier. In *2017 Computing in Cardiology (CinC)*, pages 1–4. IEEE, 2017.

[81] Shreyasi Datta, Chetanya Puri, Ayan Mukherjee, Rohan Banerjee, Anirban Dutta Choudhury, Rituraj Singh, Arijit Ukil, Soma Bandyopadhyay, Arpan Pal, and Sundeep Khandelwal. Identifying normal, af and other abnormal ecg rhythms using a cascaded binary classifier. In *2017 Computing in Cardiology (CinC)*, pages 1–4. IEEE, 2017.

[82] Lucia Billeci, Franco Chiarugi, Magda Costi, David Lombardi, and Maurizio Varanini. Detection of af and other rhythms using rr variability and ecg spectral measures. In *2017 Computing in Cardiology (CinC)*, pages 1–4. IEEE, 2017.

[83] Jacob R Sutton, Ruhi Mahajan, Oguz Akbilgic, and Rishikesan Kamaleswaran. Physonline: an open source machine learning pipeline for real-time analysis of streaming physiological waveform. *IEEE journal of biomedical and health informatics*, 23(1):59–65, 2018.

[84] Rocío Cabrera Lozoya, Benjamin Berte, Hubert Cochet, Pierre Jaïs, Nicholas Ayache, and Maxime Sermesant. Model-based feature augmentation for cardiac ablation target learning from images. *IEEE Transactions on Biomedical Engineering*, 66(1):30–40, 2018.

[85] Sally L Rutherford, Mark L Trew, Gregory B Sands, Ian J LeGrice, and Bruce H Smaill. High-resolution 3-dimensional reconstruction of the infarct border zone: impact of structural remodeling on electrical activation. *Circ Res*, 111(3):301–11, Jul 2012.

[86] Michel Haissaguerre, Ashok J Shah, Hubert Cochet, Meleze Hocini, Remi Dubois, Igor Efimov, Edward Vigmond, Olivier Bernus, and Natalia Trayanova. Intermittent drivers anchoring to structural heterogeneities as a major pathophysiological mechanism of human persistent atrial fibrillation. *J Physiol*, 594(9):2387–98, 05 2016.

[87] Amir S Jadidi, Hubert Cochet, Ashok J Shah, Steven J Kim, Edward Duncan, Shinsuke Miyazaki, Maxime Sermesant, Heiko Lehrmann, Matthieu Lederlin, Nick Linton, Andrei Forclaz, Isabelle Nault, Lena Rivard, Matthew Wright, Xingpeng Liu, Daniel Scherr, Stephen B Wilton, Laurent Roten, Patrizio Pascale, Nicolas Derval, Frédéric Sacher, Sebastien Knecht, Cornelius Keyl, Mélèze Hocini, Michel Montaudon, Francois Laurent, Michel Haïssaguerre, and Pierre Jaïs. Inverse relationship between fractionated electrograms and atrial fibrosis in persistent atrial fibrillation: combined magnetic resonance imaging and high-density mapping. *J Am Coll Cardiol*, 62(9):802–12, Aug 2013.

[88] Juan F. Gomez, Karen Cardona, Laura Martinez, Javier Saiz, and Beatriz Trenor. Electrophysiological and structural remodeling in heart failure modulate arrhythmogenesis. 2D simulation study. *PLoS ONE*, 9(7), 2014.

[89] Caroline H. Roney, Jason D. Bayer, Sohail Zahid, Marianna Meo, Patrick M.J. Boyle, Natalia A. Trayanova, Michel Haïssaguerre, Rémi Dubois, Hubert Cochet, and Edward J. Vigmond. Modelling methodology of atrial fibrosis affects rotor dynamics and electrograms. *Europace : European pacing, arrhythmias, and cardiac electrophysiology : journal of the working groups on cardiac pacing, arrhythmias, and cardiac cellular electrophysiology of the European Society of Cardiology*, 18:iv146–iv155, 2016.

[90] Jason D Bayer, Caroline H Roney, Ali Pashaei, Pierre Jaïs, and Edward J Vigmond. Novel radiofrequency ablation strategies for terminating atrial

fibrillation in the left atrium: A simulation study. *Front Physiol*, 7:108, 2016.

[91] Edward Vigmond, Ali Pashaei, Sana Amraoui, Hubert Cochet, and Michel Hassaguerre. Percolation as a mechanism to explain atrial fractionated electrograms and reentry in a fibrosis model based on imaging data. *Heart Rhythm*, 13(7):1536–1543, 2016.

[92] Martin W. Krueger, Kawal S. Rhode, Mark D. O'Neill, C. Aldo Rinaldi, Jaswinder Gill, Reza Razavi, Gunnar Seemann, and Olaf Doessel. Patient-specific modeling of atrial fibrosis increases the accuracy of sinus rhythm simulations and may explain maintenance of atrial fibrillation. *Journal of Electrocardiology*, 47(3):324–328, 2014.

[93] K Andrew MacCannell, Hojjat Bazzazi, Lisa Chilton, Yoshiyuki Shibukawa, R. B. Clark, and W. R. Giles. A mathematical model of electrotonic interactions between ventricular myocytes and fibroblasts. *Biophysical journal*, 92(11):4121–32, 2007.

[94] Peter Kohl, Patrizia Camelliti, Francis L Burton, and Godfrey L Smith. Electrical coupling of fibroblasts and myocytes: relevance for cardiac propagation. *J Electrocardiol*, 38(4 Suppl):45–50, Oct 2005.

[95] V. Jacquemet and C. S. Henriquez. Loading effect of fibroblast-myocyte coupling on resting potential, impulse propagation, and repolarization: insights from a microstructure model. *AJP: Heart and Circulatory Physiology*, 294(5):H2040–H2052, 2008.

[96] Guillermo Avila, Irma M Medina, Esperanza Jiménez, Guillermo Elizondo, and Citlalli I Aguilar. Transforming growth factor-beta1 decreases cardiac muscle l-type ca2+ current and charge movement by acting on the cav1.2 mrna. *Am J Physiol Heart Circ Physiol*, 292(1):H622–31, Jan 2007.

[97] Jorge Sánchez, Juan F Gomez, Laura Martinez-Mateu, Lucia Romero, Javier Saiz, and Beatriz Trenor. Heterogeneous effects of fibroblast-myocyte coupling in different regions of the human atria under conditions of atrial fibrillation. *Front Physiol*, 10:847, 2019.

[98] Robert S. Oakes, Troy J. Badger, Eugene G. Kholmovski, Nazem Akoum, Nathan S. Burgon, Eric N. Fish, Joshua J E Blauer, Swati N. Rao, Edward V R Dibella, Nathan M. Segerson, Marcos Daccarett, Jessiciah Windfelder, Christopher J. McGann, Dennis Parker, Rob S. MacLeod, and Nassir F. Marrouche. Detection and quantification of left atrial structural remodeling with delayed-enhancement magnetic resonance imaging in patients with atrial fibrillation. *Circulation*, 119(13):1758–1767, 2009.

[99] Marcos Daccarett, Troy J. Badger, Nazem Akoum, Nathan S. Burgon, Christian Mahnkopf, Gaston Vergara, Eugene Kholmovski, Christopher J. McGann, Dennis Parker, Johannes Brachmann, Rob S. MacLeod, and Nassir F. Marrouche. Association of left atrial fibrosis detected by delayed-enhancement magnetic resonance imaging and the risk of stroke in patients with atrial fibrillation. *Journal of the American College of Cardiology*,

174

57(7):831–838, 2011.

[100] Ana Ferrer-Albero, Eduardo J. Godoy, Miguel Lozano, Laura Martõnez-Mateu, Felipe Atienza, Javier Saiz, and Rafael Sebastian. Non-invasive localization of atrial ectopic beats by using simulated body surface P-wave integral maps. *PLoS ONE*, 12(7), 2017.

[101] David B Geselowitz and W T Miller. A bidomain model for anisotropic cardiac muscle. *Annals of Biomedical Engineering*, 11(3):191–206, may 1983.

[102] Jason Pellman, Jing Zhang, and Farah Sheikh. Myocyte-fibroblast communication in cardiac fibrosis and arrhythmias: Mechanisms and model systems. *J Mol Cell Cardiol*, 94:22–31, 05 2016.

[103] Giedrius Gaudesius, Michele Miragoli, Stuart P Thomas, and Stephan Rohr. Coupling of cardiac electrical activity over extended distances by fibroblasts of cardiac origin. *Circ Res*, 93(5):421–8, Sep 2003.

[104] Patrizia Camelliti, Colin R Green, and Peter Kohl. Structural and functional coupling of cardiac myocytes and fibroblasts. *Adv Cardiol*, 42:132–149, 2006.

[105] Peter Kohl and Patrizia Camelliti. Fibroblast-myocyte connections in the heart. *Heart Rhythm*, 9(3):461–4, Mar 2012.

[106] Maarten Hulsmans, Sebastian Clauss, Ling Xiao, Aaron D Aguirre, Kevin R King, Alan Hanley, William J Hucker, Eike M Wülfers, Gunnar Seemann, Gabriel Courties, Yoshiko Iwamoto, Yuan Sun, Andrej J Savol, Hendrik B Sager, Kory J Lavine, Gregory A Fishbein, Diane E Capen, Nicolas Da Silva, Lucile Miquerol, Hiroko Wakimoto, Christine E Seidman, Jonathan G Seidman, Ruslan I Sadreyev, Kamila Naxerova, Richard N Mitchell, Dennis Brown, Peter Libby, Ralph Weissleder, Filip K Swirski, Peter Kohl, Claudio Vinegoni, David J Milan, Patrick T Ellinor, and Matthias Nahrendorf. Macrophages facilitate electrical conduction in the heart. *Cell*, 169(3):510–522.e20, 04 2017.

[107] Vincent Jacquemet. An eikonal-diffusion solver and its application to the interpolation and the simulation of reentrant cardiac activations. *Computer Methods and Programs in Biomedicine*, 108(2):548–558, 2012.

[108] Patrick M Boyle, Sohail Zahid, and Natalia A Trayanova. Towards personalized computational modelling of the fibrotic substrate for atrial arrhythmia. *Europace*, 18(suppl 4):iv136–iv145, Dec 2016.

[109] P Kohl, A G Kamkin, I S Kiseleva, and D Noble. Mechanosensitive fibroblasts in the sino-atrial node region of rat heart: interaction with cardiomyocytes and possible role. *Exp Physiol*, 79(6):943–56, Nov 1994.

[110] Pasquale Santangeli and Francis E. Marchlinski. Techniques for the provocation, localization, and ablation of non–pulmonary vein triggers for atrial fibrillation. *Heart Rhythm*, 14(7):1087–1096, 2017.

[111] Peter M. Kistler, Kurt C. Roberts-Thomson, Haris M. Haqqani, Simon P. Fynn, Suresh Singarayar, Jitendra K. Vohra, Joseph B. Morton, Paul B. Sparks, and Jonathan M. Kalman. P-Wave Morphology in Focal Atrial

Tachycardia. Development of an Algorithm to Predict the Anatomic Site of Origin. *Journal of the American College of Cardiology*, 48(5):1010–1017, 2006.

[112] Ellen Hoffmann, Christopher Reithmann, Petra Nimmermann, Florian Elser, Uwe Dorwarth, Thomas Remp, and Gerhard Steinbeck. Clinical experience with electroanatomic mapping of ectopic atrial tachycardia. *Pacing and clinical electrophysiology : PACE*, 25(1):49–56, 2002.

[113] Pasquale Santangeli, Erica S Zado, Mathew D Hutchinson, Michael P Riley, David Lin, David S Frankel, Gregory E Supple, Fermin C Garcia, Sanjay Dixit, David J Callans, and Francis E Marchlinski. Prevalence and distribution of focal triggers in persistent and long-standing persistent atrial fibrillation. *Heart Rhythm*, 13(2):374–382, feb 2016.

[114] Deepak Bhakta and John M. Miller. Principles of electroanatomic mapping. *Indian Pacing and Electrophysiology Journal*, 8(1):32–50, 2008.

[115] Francesco Santoro, Christian H. Heeger, Andreas Metzner, Natale D. Brunetti, Matteo Di Biase, Karl Heinz Kuck, and Feifan Ouyang. Targeting ablation strategies and electro-anatomical systems for different atrial fibrillation patterns. *Minerva Cardioangiologica*, 66(1):63–74, 2018.

[116] Alan S. Go, Elaine M. Hylek, Kathleen A. Phillips, YuChiao Chang, Lori E. Henault, Joe V. Selby, and Daniel E. Singer. Prevalence of Diagnosed Atrial Fibrillation in Adults. *Jama*, 285(18):2370, 2001.

[117] Madison S. Spach and John P. Boineau. Microfibrosis produces electrical load variations due to loss of side- to-side cell connections: A major mechanism of structural heart disease arrhythmias. *PACE - Pacing and Clinical Electrophysiology*, 20(2 II):397–413, 1997.

[118] Natalia A. Trayanova and Patrick M. Boyle. Advances in modeling ventricular arrhythmias: From mechanisms to the clinic. *Wiley Interdisciplinary Reviews: Systems Biology and Medicine*, 6(2):209–224, 2014.

[119] Oleg V. Aslanidi, Michael A. Colman, Jonathan Stott, Halina Dobrzynski, Mark R. Boyett, Arun V. Holden, and Henggui Zhang. 3D virtual human atria: A computational platform for studying clinical atrial fibrillation. *Progress in Biophysics and Molecular Biology*, 107(1):156–168, 2011.

[120] Jichao Zhao, Sanjay R. Kharche, Brian J. Hansen, Thomas A. Csepe, Yufeng Wang, Martin K. Stiles, and Vadim V. Fedorov. Optimization of catheter ablation of atrial fibrillation: Insights gained from clinically-derived computer models. *International Journal of Molecular Sciences*, 16(5):10834–10854, 2015.

[121] Maria S. Guillem, Andreu M. Climent, Miguel Rodrigo, Francisco Fernandez-Aviles, Felipe Atienza, and Omer Berenfeld. Presence and stability of rotors in atrial fibrillation: Evidence and therapeutic implications. *Cardiovascular Research*, 109(4):480–492, 2016.

[122] José Jalife. Déjà vu in the theories of atrial fibrillation dynamics. *Cardiovascular Research*, 89(4):766–775, 2011.

[123] Ashok J Shah, Meleze Hocini, Patrizio Pascale, Laurent Roten, Yuki Komatsu, Matthew Daly, Khaled Ramoul, Arnaud Denis, Nicolas Derval, Frederic Sacher, Remi Dubois, Ryan Bokan, Sandra Eliatou, Maria Strom, Charu Ramanathan, Pierre Jais, Philippe Ritter, and Michel Haissaguerre. Body Surface Electrocardiographic Mapping for Non-invasive Identification of Arrhythmic Sources. *Arrhythmia & electrophysiology review*, 2(1):16–22, 2013.

[124] Sophie Giffard-Roisin, Thomas Jackson, Lauren Fovargue, Jack Lee, Herve Delingette, Reza Razavi, Nicholas Ayache, and Maxime Sermesant. Non-Invasive Personalisation of a Cardiac Electrophysiology Model from Body Surface Potential Mapping. *IEEE Transactions on Biomedical Engineering*, 64(9):1–1, 2016.

[125] Maria S Guillem, Andreu M Climent, Jose Millet, Ángel Arenal, Francisco Fernández-Avilés, José Jalife, Felipe Atienza, and Omer Berenfeld. Noninvasive localization of maximal frequency sites of atrial fibrillation by body surface potential mapping. *Circ Arrhythm Electrophysiol*, 6(2):294–301, Apr 2013.

[126] Miguel Rodrigo, Maria S Guillem, Andreu M Climent, Jorge Pedrón-Torrecilla, Alejandro Liberos, José Millet, Francisco Fernández-Avilés, Felipe Atienza, and Omer Berenfeld. Body surface localization of left and right atrial high-frequency rotors in atrial fibrillation patients: a clinical-computational study. *Heart Rhythm*, 11(9):1584–91, Sep 2014.

[127] J Feng, L Yue, Z Wang, and S Nattel. Ionic mechanisms of regional action potential heterogeneity in the canine right atrium. *Circ Res*, 83(5):541–51, Sep 1998.

[128] D Li, L Zhang, J Kneller, and S Nattel. Potential ionic mechanism for repolarization differences between canine right and left atrium. *Circ Res*, 88(11):1168–75, Jun 2001.

[129] D Dobrev, E Graf, E Wettwer, H M Himmel, O Hála, C Doerfel, T Christ, S Schüler, and U Ravens. Molecular basis of downregulation of g-protein-coupled inward rectifying k(+) current (i(k,ach)) in chronic human atrial fibrillation: decrease in girk4 mrna correlates with reduced i(k,ach) and muscarinic receptor-mediated shortening of action potentials. *Circulation*, 104(21):2551–7, Nov 2001.

[130] Tae-Joon Cha, Joachim R Ehrlich, Liming Zhang, Denis Chartier, Tack Ki Leung, and Stanley Nattel. Atrial tachycardia remodeling of pulmonary vein cardiomyocytes: comparison with left atrium and potential relation to arrhythmogenesis. *Circulation*, 111(6):728–35, Feb 2005.

[131] Jichao Zhao, Robert S. Stephenson, Greg B. Sands, Ian J. LeGrice, Henggui Zhang, Jonathan C. Jarvis, and Bruce H. Smaill. Atrial fibrosis and atrial fibrillation: A computer simulation in the posterior left atrium. *Lecture Notes in Computer Science (including subseries Lecture Notes in Artificial Intelligence and Lecture Notes in Bioinformatics)*, 7945 LNCS:400–408, 2013.

[132] Peter Kohl and Robert G Gourdie. Fibroblast-myocyte electrotonic coupling:

does it occur in native cardiac tissue? *J Mol Cell Cardiol*, 70:37–46, May 2014.

[133] Arne SippensGroenewegen, Heidi A.P. Peeters, Emile R. Jessurun, Andre C. Linnenbank, Etienne O. Robles de Medina, Michael D. Lesh, and Norbert M. Van Hemel. Body surface mapping during pacing at multiple sites in the human atrium: P-wave morphology of ectopic right atrial activation. *Circulation*, 97(4):369–380, 1998.

[134] David U J Keller, Frank M. Weber, Gunnar Seemann, and Olaf Dossel. Ranking the influence of tissue conductivities on forward-calculated ecgs. *IEEE Transactions on Biomedical Engineering*, 57(7):1568–1576, 2010.

[135] Frank M. Weber, David U J Keller, Stefan Bauer, Gunnar Seemann, Cristian Lorenz, and Olaf Dossel. Predicting tissue conductivity influences on body surface potentials-An efficient approach based on principal component analysis. *IEEE Transactions on Biomedical Engineering*, 58(2):265–273, 2011.

[136] S. A. Niederer, E. Kerfoot, A. P. Benson, M. O. Bernabeu, O. Bernus, C. Bradley, E. M. Cherry, R. Clayton, F. H. Fenton, A. Garny, E. Heidenreich, S. Land, M. Maleckar, P. Pathmanathan, G. Plank, J. F. Rodriguez, I. Roy, F. B. Sachse, G. Seemann, O. Skavhaug, and N. P. Smith. Verification of cardiac tissue electrophysiology simulators using an N-version benchmark. *Philosophical Transactions of the Royal Society A: Mathematical, Physical and Engineering Sciences*, 369(1954):4331–4351, 2011.

[137] Yuan Gao, Yinglan Gong, and Ling Xia. Simulation of atrial fibrosis using coupled myocyte-fibroblast cellular and human atrial models. *Comput Math Methods Med*, 2017:9463010, 2017.

[138] Trine Krogh-Madsen, Geoffrey W Abbott, and David J Christini. Effects of electrical and structural remodeling on atrial fibrillation maintenance: a simulation study. *PLoS Comput Biol*, 8(2):e1002390, 2012.

[139] Kazuhiko Tanaka, Sharon Zlochiver, Karen L. Vikstrom, Masatoshi Yamazaki, Javier Moreno, Matthew Klos, Alexey V. Zaitsev, Ravi Vaidyanathan, David S. Auerbach, Steve Landas, Gérard Guiraudon, José Jalife, Omer Berenfeld, and Jérôme Kalifa. Spatial distribution of fibrosis governs fibrillation wave dynamics in the posterior left atrium during heart failure. *Circulation Research*, 101(8):839–847, 2007.

[140] Brett Burstein, Philippe Comtois, Georghia Michael, Kunihiro Nishida, Louis Villeneuve, Yung-Hsin Yeh, and Stanley Nattel. Changes in connexin expression and the atrial fibrillation substrate in congestive heart failure. *Circ Res*, 105(12):1213–22, Dec 2009.

[141] Kathleen S. McDowell, Fijoy Vadakkumpadan, Robert Blake, Joshua Blauer, Gernot Plank, Rob S. MacLeod, and Natalia A. Trayanova. Methodology for patient-specific modeling of atrial fibrosis as a substrate for atrial fibrillation. *Journal of Electrocardiology*, 45(6):640–645, 2012.

[142] Kathleen S. McDowell, Fijoy Vadakkumpadan, Robert Blake, Joshua Blauer, Gernot Plank, Rob S. Macleod, and Natalia A. Trayanova. Mechanistic

inquiry into the role of tissue remodeling in fibrotic lesions in human atrial fibrillation. *Biophysical Journal*, 104(12):2764–2773, 2013.

[143] David E Krummen, Jason D Bayer, Jeffrey Ho, Gordon Ho, Miriam R Smetak, Paul Clopton, Natalia A Trayanova, and Sanjiv M Narayan. Mechanisms of human atrial fibrillation initiation: clinical and computational studies of repolarization restitution and activation latency. *Circ Arrhythm Electrophysiol*, 5(6):1149–59, Dec 2012.

[144] Natalia A. Trayanova. Mathematical approaches to understanding and imaging atrial fibrillation: Significance for mechanisms and management. *Circulation Research*, 114(9):1516–1531, 2014.

[145] Sohail Zahid, Hubert Cochet, Patrick M. Boyle, Erica L. Schwarz, Kaitlyn N. Whyte, Edward J. Vigmond, Rémi Dubois, Mélèze Hocini, Michel Haïssaguerre, Pierre Jaïs, and Natalia A. Trayanova. Patient-derived models link re-entrant driver localization in atrial fibrillation to fibrosis spatial pattern. *Cardiovascular Research*, 110(3):443–454, 2016.

[146] Kathleen S. McDowell, Sohail Zahid, Fijoy Vadakkumpadan, Joshua Blauer, Rob S. MacLeod, and Natalia A. Trayanova. Virtual electrophysiological study of atrial fibrillation in fibrotic remodeling. *PLoS ONE*, 10(2):1–16, 2015.

[147] Edward J Ciaccio, Elaine Y Wan, Deepak S Saluja, U Rajendra Acharya, Nicholas S Peters, and Hasan Garan. Addressing challenges of quantitative methodologies and event interpretation in the study of atrial fibrillation. *Comput Methods Programs Biomed*, 178:113–122, Sep 2019.

[148] Prashnna Kumar Gyawali, B Milan Horacek, John L Sapp, and Linwei Wang. Sequential factorized autoencoder for localizing the origin of ventricular activation from 12-lead electrocardiograms. *IEEE Trans Biomed Eng*, 67(5):1505–1516, May 2020.

[149] John M Miller, FRANCIS E Marchlinski, Alfred E Buxton, and Mark E Josephson. Relationship between the 12-lead electrocardiogram during ventricular tachycardia and endocardial site of origin in patients with coronary artery disease. *Circulation*, 77(4):759–766, 1988.

[150] John L Sapp, Meir Bar-Tal, Adam J Howes, Jonathan E Toma, Ahmed El-Damaty, James W Warren, Paul J MacInnis, Shijie Zhou, and B Milan Horáček. Real-time localization of ventricular tachycardia origin from the 12-lead electrocardiogram. *JACC: Clinical Electrophysiology*, 3(7):687–699, 2017.

[151] Shijie Zhou, B Milan Horáček, James W Warren, Amir AbdelWahab, and John L Sapp. Rapid 12-lead automated localization method: Comparison to electrocardiographic imaging (ecgi) in patient-specific geometry. *J Electrocardiol*, 51(6S):S92–S97, 2018.

[152] Miki Yokokawa, Tzu-Yu Liu, Kentaro Yoshida, Clayton Scott, Alfred Hero, Eric Good, Fred Morady, and Frank Bogun. Automated analysis of the 12-lead electrocardiogram to identify the exit site of postinfarction ventricular

tachycardia. *Heart Rhythm*, 9(3):330–334, 2012.

[153] John L Sapp, Ahmed El-Damaty, Paul J MacInnis, James W Warren, and B Milan Horácek. Automated localization of pacing sites in postinfarction patients from the 12-lead electrocardiogram and body-surface potential maps. *Computing in Cardiology*, 2012.

[154] Andres Orozco-Duque, John Bustamante, and German Castellanos-Dominguez. Semi-supervised clustering of fractionated electrograms for electroanatomical atrial mapping. *Biomedical engineering online*, 15(1):44, 2016.

[155] Max Falkenberg McGillivray, William Cheng, Nicholas S Peters, and Kim Christensen. Machine learning methods for locating re-entrant drivers from electrograms in a model of atrial fibrillation. *Royal Society open science*, 5(4):172434, 2018.

[156] Seiko Kawano, Masayasu Hiraoka, Machiko Yamamoto, Tohru Sawanobori, and Yasuki Sakamoto. Body surface maps of ectopic p waves originating in the left atrium in the dog. *Journal of electrocardiology*, 22(1):27–43, 1989.

[157] Seiko Kawano, Tohru Sawanobori, and Masayasu Hiraoka. Human body surface mapping during atrial depolarization in normal and diseased subjects. *Journal of electrocardiology*, 16(2):151–159, 1983.

[158] Daniele Giacopelli, John P Bourke, Alan Murray, and Philip Langley. Spatial pattern of p waves in paroxysmal atrial fibrillation patients in sinus rhythm and controls. *Pacing and clinical electrophysiology*, 35(7):819–826, 2012.

[159] Arne SippensGroenewegen, Andrea Natale, Nassir F. Marrouche, Diana Bash, and Jie Cheng. Potential role of body surface ECG mapping for localization of atrial fibrillation trigger sites. In *Journal of Electrocardiology*, volume 37, pages 47–52, 2004.

[160] Michael A. Colman, Oleg V. Aslanidi, Jonathan Stott, Arun V. Holden, and Henggui Zhang. Correlation between P-wave morphology and origin of atrial focal tachycardia-insights from realistic models of the human atria and torso. *IEEE Transactions on Biomedical Engineering*, 58(10 PART 2):2952–2955, 2011.

[161] Erick A Perez Alday, Michael A Colman, Philip Langley, Timothy D Butters, Jonathan Higham, Antony J Workman, Jules C Hancox, and Henggui Zhang. A new algorithm to diagnose atrial ectopic origin from multi lead ecg systems–insights from 3d virtual human atria and torso. *PLoS Comput Biol*, 11(1):e1004026, Jan 2015.

[162] Christian Reich, Tobias Oesterlein, Markus Rottmann, Gunnar Seemann, and Olaf Dossel. Classification of cardiac excitation patterns during atrial fibrillation. *Current Directions in Biomedical Engineering*, 2(1):161–166, 2016.

[163] Sophocles J Orfanidis. *Introduction to signal processing*. Prentice-Hall, Inc., 1995.

[164] Joe H. Ward Jr. Hierarchical grouping to optimize an objective function. *Journal of the American Statistical Association*, 58(301):236–244, 1963.

[165] F. Pedregosa, G. Varoquaux, A. Gramfort, V. Michel, B. Thirion, O. Grisel, M. Blondel, P. Prettenhofer, R. Weiss, V. Dubourg, J. Vanderplas, A. Passos, D. Cournapeau, M. Brucher, M. Perrot, and E. Duchesnay. Scikit-learn: Machine learning in Python. *Journal of Machine Learning Research*, 12:2825–2830, 2011.

[166] Lars Buitinck, Gilles Louppe, Mathieu Blondel, Fabian Pedregosa, Andreas Mueller, Olivier Grisel, Vlad Niculae, Peter Prettenhofer, Alexandre Gramfort, Jaques Grobler, Robert Layton, Jake VanderPlas, Arnaud Joly, Brian Holt, and Gaël Varoquaux. API design for machine learning software: experiences from the scikit-learn project. In *ECML PKDD Workshop: Languages for Data Mining and Machine Learning*, pages 108–122, 2013.

[167] Olaf Dossel, Martin W Krueger, Frank M Weber, Mathias Wilhelms, and Gunnar Seemann. Computational modeling of the human atrial anatomy and electrophysiology. *Med Biol Eng Comput*, 50(8):773–99, Aug 2012.

[168] R.S. MacLeod, E. Kholmovski, E.V.R. DiBella, R.S. Oakes, J.E. Blauer, E. Fish, S. Vijayakumar, M. Daccarett, N.M. Segerson, and N.F. Marrouche. Integration of MRI in evaluation and ablation of atrial fibrillation. *Computers in Cardiology*, pages 77–80, 2008.

[169] J B Morton, P Sanders, a Das, J K Vohra, P B Sparks, and J M Kalman. Focal atrial tachycardia arising from the tricuspid annulus: electrophysiologic and electrocardiographic characteristics. *Journal of cardiovascular electrophysiology*, 12(6):653–659, 2001.

[170] Peter M. Kistler, Prashanthan Sanders, Simon P. Fynn, Irene H. Stevenson, Azlan Hussin, Jitendra K. Vohra, Paul B. Sparks, and Jonathan M. Kalman. Electrophysiological and Electrocardiographic Characteristics of Focal Atrial Tachycardia Originating From the Pulmonary Veins: Acute and Long-Term Outcomes of Radiofrequency Ablation. *Circulation*, 108(16):1968–1975, 2003.

[171] Peter M. Kistler, Simon P. Fynn, Haris Haqqani, Irene H. Stevenson, Jitendra K. Vohra, Joseph B. Morton, Paul B. Sparks, and Jonathan M. Kalman. Focal atrial tachycardia from the ostium of the coronary sinus: Electrocardiographic and electrophysiological characterization and radiofrequency ablation. *Journal of the American College of Cardiology*, 45(9):1488–1493, 2005.

[172] Adriaan Van Oosterom. The inverse problem of bioelectricity: An evaluation, 2012.

[173] Vincent Jacquemet. Lessons from computer simulations of ablation of atrial fibrillation. *The Journal of physiology*, 594(9):2417–2430, 2016.

[174] Shih-Huang Lee, Ching-Tai Tai, Ming-Hsiung Hsieh, Hsuan-Ming Tsao, Yenn-Jiang Lin, Shih-Lin Chang, Jin-Long Huang, Kun-Tai Lee, Yi-Jen Chen, Jun-Jack Cheng, et al. Predictors of non-pulmonary vein ectopic beats initiating paroxysmal atrial fibrillation: implication for catheter ablation. *Journal of the American College of Cardiology*, 46(6):1054–1059, 2005.

[175] Shinsuke Miyazaki, Masateru Takigawa, Shigeki Kusa, Taishi Kuwahara, Hi-

roshi Taniguchi, Kenji Okubo, Hiroaki Nakamura, Hitoshi Hachiya, Kenzo Hirao, Atsushi Takahashi, et al. Role of arrhythmogenic superior vena cava on atrial fibrillation. *Journal of cardiovascular electrophysiology*, 25(4):380–386, 2014.

[176] Wei-Shiang Lin, Ching-Tai Tai, Ming-Hsiung Hsieh, Chin-Feng Tsai, Yung-Kuo Lin, Hsuan-Ming Tsao, Jin-Long Huang, Wen-Chung Yu, Shih-Ping Yang, Yu-An Ding, et al. Catheter ablation of paroxysmal atrial fibrillation initiated by non–pulmonary vein ectopy. *Circulation*, 107(25):3176–3183, 2003.

[177] Raúl Alcaraz Martínez, José J. Rieta, and Fernando Hornero. Caracterización no invasiva de la actividad auricular durante los instantes previos a la terminación de la fibrilación auricular paroxística. *Revista Espanola de Cardiologia*, 61(2):154–160, 2008.

[178] Jorge Mateo and José Joaquín Rieta. Radial basis function neural networks applied to efficient QRST cancellation in atrial fibrillation. *Computers in Biology and Medicine*, 43(2):154–163, 2013.

[179] Fredrik Gustafsson. Determining the initial states in forward-backward filtering. *IEEE Transactions on signal processing*, 44(4):988–992, 1996.

[180] Sergio Shkurovich, Alan V Sahakian, and Steven Swiryn. Detection of atrial activity from high-voltage leads of implantable ventricular defibrillators using a cancellation technique. *IEEE Transactions on Biomedical Engineering*, 45(2):229–234, 1998.

[181] Andreas Bollmann, NarendraK Kanuru, KevinK McTeague, PaulF Walter, DavidB DeLurgio, and JonathanJ Langberg. Frequency analysis of human atrial fibrillation using the surface electrocardiogram and its response to ibutilide. *The American journal of cardiology*, 81(12):1439–1445, 1998.

[182] Jiapu Pan and Willis J Tompkins. A real-time qrs detection algorithm. *IEEE transactions on biomedical engineering*, 32(3):230–236, 1985.

[183] Patrick S Hamilton and Willis J Tompkins. Quantitative investigation of qrs detection rules using the mit/bih arrhythmia database. *IEEE transactions on biomedical engineering*, 33(12):1157–1165, 1986.

[184] A. Ferrer-Albero, E. J. Godoy, R. Sebastian, L. MartÃ-nez, and J. Saiz. Analysis of in-silico body surface p-wave integral maps show important differences depending on the connections between coronary sinus and left atrium. In *2016 Computing in Cardiology Conference (CinC)*, pages 745–748, Sep. 2016.

[185] Martin Stridh and L Sornmo. Spatiotemporal qrst cancellation techniques for analysis of atrial fibrillation. *IEEE Transactions on Biomedical Engineering*, 48(1):105–111, 2001.

[186] Carolina Vásquez, Alfredo Hernández, Fernando Mora, Guy Carrault, and Gianfranco Passariello. Atrial activity enhancement by wiener filtering using an artificial neural network. *IEEE Transactions on Biomedical Engineering*, 48(8):940–944, 2001.

[187] C Sanchez, J Millet, JJ Rieta, F Castells, J Rodenas, R Ruiz-Granell, and V Ruiz. Packet wavelet decomposition: An approach for atrial activity extraction. In *Computers in Cardiology*, pages 33–36. IEEE, 2002.

[188] Michel Haissaguerre, Meleze Hocini, Arnaud Denis, Ashok J Shah, Yuki Komatsu, Seigo Yamashita, Matthew Daly, Sana Amraoui, Stephan Zellerhoff, Marie-Quitterie Picat, Adam Quotb, Laurence Jesel, Han Lim, Sylvain Ploux, Pierre Bordachar, Guillaume Attuel, Valentin Meillet, Philippe Ritter, Nicolas Derval, Frederic Sacher, Olivier Bernus, Hubert Cochet, Pierre Jais, and Remi Dubois. Driver domains in persistent atrial fibrillation. *Circulation*, 130(7):530–8, Aug 2014.

[189] Sanjiv M Narayan, David E Krummen, Kalyanam Shivkumar, Paul Clopton, Wouter-Jan Rappel, and John M Miller. Treatment of atrial fibrillation by the ablation of localized sources: Confirm (conventional ablation for atrial fibrillation with or without focal impulse and rotor modulation) trial. *J Am Coll Cardiol*, 60(7):628–36, Aug 2012.